The Application of MEMS Microphone Arrays to Aeroacoustic Measurements

by

Adam E. Bale

A thesis
presented to the University of Waterloo
in fulfillment of the
thesis requirement for the degree of
Master of Applied Science
in
Mechanical Engineering

Waterloo, Ontario, Canada, 2011

I hereby declare that I am the sole author of this thesis. This is a true copy of the thesis, including any required final revisions, as accepted by my examiners.

I understand that my thesis may be made electronically available to the public.

Abstract

Aeroacoustic emissions were identified as a primary concern in the public acceptance of wind turbines. A review of literature involving sound localization was undertaken and led to the design of two microphone arrays to identify acoustic sources. A small-scale array composed of 27 sensors was produced with the intention of improving the quality of sound measurements over those made by a single microphone in a small, closed-loop wind tunnel. A large-scale array containing 30 microphones was also implemented to allow for measurements of aeroacoustic emissions from airfoils and rotating wind turbines. To minimize cost and pursue alternative sensor technologies, microelectromechanical microphones were selected for the array sensors and assembled into the arrays on printed circuit boards. Characterization of the microphones was completed using a combination of calibration techniques, primarily in a plane wave tube.

Array response to known sources was quantified by analyzing source maps with respect to source location accuracy, beamwidth, and root mean square error. Multiple sources and rotating sources were tested to assess array performance. Following validation with known sources, wind tunnel testing of a 600 watt wind turbine was performed at freestream speeds of 2.5 m/s, 3.5 m/s, 4.5 m/s, and to 5.5 m/s. Significant aeroacoustic emissions were noted from the turbine in the 4.5 m/s and 5.5 m/s cases, with an increase of up to 12 dB over background levels. Source maps from the 5.5 m/s tests revealed that the primary location of aeroacoustic emissions was near the outer radii of the rotor, but not at the tip, and generally moved radially outward with increasing frequency. The azimuthal location of the greatest sound pressure levels was typically found to be between 120° and 130° measured counterclockwise from the upward vertical, coinciding with the predicted location of greatest emissions provided by an analytical model based on dipole directivity and convective amplification. Analysis of the acoustic spectra, turbine operating characteristics, and previous literature suggested that the sound emissions emanated from the trailing edge of the blades.

Acknowledgements

I would like to thank the many people who assisted me and provided valuable insight into my research. To my supervisor Dr. David Johnson, I would like to extend my thanks for allowing me to pursue research in acoustics. Your constant support, insight, and encouragement helped me through the inevitable difficulties of experimental research. To my fellow Wind Energy Group members, Drew Gertz, Vivian Lam, Kobra Gharali, Erik Skensved, Adam McPhee, Brian Gaunt, and Mike McWilliam, many thanks for their contributions of knowledge, assistance, and conversation. Special thanks to Stephen Orlando for his valuable input in the design, fabrication, experimentation, and processing of my results.

Thanks to my family for their unending support in all I do. To my brothers Bryan and Logan for their wisdom and laughter. To my sister Kristen for her continual encouragement and for providing us with my two favourite distractions: Amelia and Charlotte. To my parents Bob and Sue, your support throughout my life has been the foundation in everything I do. Thank you for your love and reassurance. I am forever grateful to Stephanie Collins. I am humbled by your endless love and encouragement and it is with great honour that I dedicate this to you.

Table of Contents

List of Tables

List of Figures

Nomenclature

Roman Symbols

$\bar{a}$	Reconstructed source amplitude
BW	Beamwidth [m]
c	Speed of sound [m s^{-1}]
C	Chord length [m]
d	Diameter [m]
D	Directivity function
e	Steering vector component
$\vec{e}$	Steering vector
E	Source map error
f	Frequency [Hz]
f_d	Perceived frequency due to Doppler effect
$\triangle f$	Frequency bandwidth resolution [Hz]
$\vec{F}$	Force vector [N]
$\mathcal{F}$	Generalized pressure source
G	Array gain
$\vec{G}$	Cross spectral matrix
$G_{mm'}$	Cross spectrum between P_m and $P_{m'}$
K	Number of FFT blocks

l	Length [m]
L_p	Sound pressure level [dB]
M	Number of microphones
$\vec{M}$	Mach number
N	Number of grid points
p	Pressure [Pa]
P	Fourier transform of microphone signal
r	Radius [m]
R	Gas constant [J kg^{-1} K^{-1}]
$s(t)$	Source field
t	Time [s]
$\triangle t$	Microphone time delay [s]
T	Temperature [K]
T_b	FFT block length
$\vec{v}$	Velocity [m s^{-1}]
w	Microphone weighting factor
w_s	Windowing constant
$\vec{x}$	Position
$\vec{x}_p$	Co-array
$y(t)$	Microphone signal
$Y(\vec{e})$	Array output at focus location
$z(t)$	Reconstructed microphone signal

Greek Symbols

α	Angle of attack [^{o}]

γ Specific heat ratio

θ Angle between blade plane and plane containing observer and chord [^{o}]

λ Wavelength [m]

ν Kinematic viscosity [m^2 s^{-}1]

ξ Angle between relative blade velocity and source-observer line [^{o}]

ρ Density [kg m^{-1}]

σ Stress [Pa]

ϕ Angle between relative blade velocity and plane containing observer and chord [^{o}]

φ Angle of incidence or refraction [^{o}]

Subscripts

a Measured signal

$diag$ Diagonal matrix

H High-frequency cutoff

i, j, k Vector and tensor indices

k FFT block index

L Low-frequency cutoff

m Microphone index

m' Cross correlation microphone index

n Grid point index

ref Reference

rms Root mean square

t Theoretical signal

Chapter 1

Introduction

1.1 Project Motivation

Sound emissions are one of the primary concerns in the public's acceptance of the widespread use of wind turbines. With the increasing installation of wind farms as an alternative energy source, public awareness of wind turbines is also increasing. In an effort to reduce the impact of wind farms in developed locations, stricter standards are being put into place for turbine siting, requiring that the emissions from turbines are sufficiently quiet at ground level receptors, such as homes, businesses, or other public areas [1]. These standards typically impose limits on the allowable sound pressure level or force mandatory setbacks on the minimum distance from a turbine to any receptor. The design of wind farms is already considerably challenging since they must be located in areas with high wind speeds, suitable topography, available land, and close proximity to existing electricity transmission infrastructure. Incorporating strict requirements on allowable sound emissions adds further challenge to the implementation of an operating wind farm. Meeting the requirements of the regulations can involve reducing the number of turbines in the wind farm or decreasing the noise levels by decreasing the rotational rate of turbines to lower tip speeds at the expense of power production and profitability. In order to meet the increase in demand for wind energy while meeting the requirements of the regulations, efforts must be concentrated on improving turbine design to reduce sound emissions.

While wind turbines exist in a number of forms, this thesis deals explicitly with three-bladed horizontal-axis wind turbines. Wind turbines have a wide range of sizes consistent with their application. Turbines for residential or remote charging applications can have rotor diameters as small as 1 metre while wind turbines involved in commercial power production can have rotor diameters on the order of 100 metres. Regardless of the size, the same principles of power generation are employed. The turbine blades are composed of airfoils of varying shapes and sizes along their length and are responsible for producing lift from the flow of air. The lift force creates a torque which is used to drive a generator for

power production. As a rotating machine with many moving parts, wind turbines produce sound emissions as a by-product of their power production.

There are two main emission sources: mechanical components and aeroacoustic sources due to flow interacting with the blades. Mechanical contributions originate from the various moving components in the nacelle, such as gearboxes, cooling systems, and generators, but emissions from these sources can be reduced by soundproofing the nacelle and by ensuring proper maintenance of moving parts [2]. Importantly, aerodynamically generated sources are the dominant source of emissions [3]. A number of aeroacoustic mechanisms have been identified, including flow interactions between the blade and tower, stall noise, tip noise, in-flow turbulence noise at the leading edge, and trailing edge noise [2].

In order to study the various sound generation mechanisms from a wind turbine, it is often advantageous to eliminate uncontrollable parameters encountered in field testing such as variations in wind direction, wind speed, turbulence, and background noise. Wind tunnel testing offers a suitable alternative to field tests as it enables highly repeatable test conditions, enabling acoustic testing with microphones in a controlled environment. However, it is unfeasible to perform wind tunnel testing on a commercial size wind turbine. Wind tunnel tests are therefore primarily conducted using scale models.

Even when controlled conditions are employed, measurements of a sound field performed with a single microphone can be limited in their ability to suppress background noise or distinguish contributions from multiple sources. This is particularly true in wind tunnel experiments where flow-induced noise, fan noise, and sound reflections can raise the background noise significantly and make source identification difficult [4]. Contributions from multiple sources at the same frequency, such as mechanical and aeroacoustic sources on a wind turbine, cannot be easily distinguished from each other, and therefore cannot be adequately isolated for study. Only with a technique that can distinguish sound sources can sound emissions be localized and identified. The requirement for effective sound localization has led to the development of advanced measurement tools, such as the microphone array. A microphone array, composed of many microphones in a predetermined arrangement, allows for visual representation of a sound field using a processing technique known as beamforming. A microphone array offers two considerable advantages over conventional microphone measurements: improved signal-to-noise ratio and source localization capabilities.

The objective of this research was to develop two microphone arrays for use in experimental testing of wind turbine emissions. The intention was to develop a user-friendly research technique for assessing the aeroacoustic emissions of two-dimensional wind turbine airfoils and three-dimensional rotating wind turbines. Both arrays are intended to improve the quality of measurements in difficult acoustic environments. The first array is a small-scale array intended to improve the signal-to-noise ratio of measurements made in the small closed-loop wind tunnel at the University of Waterloo [5], ideally for measuring and locating noise sources emitted by two-dimensional wind turbine specific airfoils. The

wind tunnel has a 152.4 mm square test section with hard wall surfaces throughout. The second array, with an aperture of approximately one metre, is designed for measurements and localization of sound emissions from small-scale wind turbines in an open-jet wind tunnel facility. The work presented here demonstrates measured performance in comparison to theoretical performance of both arrays using known sound sources followed by application of the measurement technique on a small wind turbine in a controlled environment.

1.2 Thesis Organization

A review of previous literature is provided in Chapter 2, including detail on aeroacoustic theory, beamforming, array considerations and application, wind turbine noise generation, and wind tunnel testing considerations. Details of array design and fabrication are included in Chapter 3. Rationale for component selection and array design are provided as are details of assembly methods for both microphone arrays. Calibration techniques used to characterize the microphones in each array are outlined in Chapter 4. Preliminary calibration methods and their shortcomings are described. An overview of the calibration methods used in sensor characterization are provided, as are results of the calibrations. Chapter 5 presents details of the equipment and experimental methods used to validate the array's performance in response to known sound sources and acoustic emissions from a 600 watt wind turbine with a rotor diameter of 1.3 metres operating in an open-jet wind tunnel facility. Experimental results and discussion are provided in Chapter 6. Experimental and theoretical source maps produced in the validation of array performance in response to known sources are included and a discussion of array resolution and error is presented where possible. Additional experimental results assessing array response to various known sources are including multiple sound sources and a rotating source are presented. Test results from a rotating wind turbine in an open-jet wind tunnel at a range of wind speeds and rotational rates are included. Finally, Chapter 7 presents the conclusions obtained from the experimental research. Recommendations and potential areas of future exploration in this field of research are provided.

Chapter 2

Literature Review

2.1 Sound

The following section discusses some basic concepts which are necessary to understanding further discussions of sound and beamforming. An introduction to sound propagation and sound wave motion is provided.

2.1.1 Introduction to Sound

Sound is created by pressure fluctuations travelling as a wave through a medium. The cause of pressure fluctuations is vibration resulting from a number of sources, such as the interaction of solid bodies and flows. At a given point in space the pressure disturbances cause changes in the velocity and density of the surrounding medium. The wave motion is created by successive compression and rarefaction of the medium in the direction of propagation. Sound therefore travels as a longitudinal wave. The distance between successive cycles is known as the wavelength. Packets of molecules in the medium do not appreciably change their average positions, but rather vibrate back and forth with the rate of change of position known as the particle velocity. Since the study of sound typically deals with relatively short distances, the inertial effects are much greater than viscous effects, so the flow can be considered inviscid. The speed of propagation can then be calculated from

$$c = \sqrt{\gamma RT}$$

where γ is the gas specific heat ratio, R is the thermodynamic constant of the gas, and T is the absolute temperature of the gas [6]. At 20 °C, the speed of sound is therefore found to be 343 m/s. When pressure fluctuations occur at a constant frequency, the wavelength can be related to the frequency and speed of sound by,

$$\lambda = \frac{c}{f} \tag{2.1}$$

where f is the frequency of the sound source.

The pressure disturbances are weak in relation to atmospheric pressure, but can have a large range of fluctuation, leading to the need for a logarithmic scale in defining their amplitude. The pressure amplitude of sound is commonly expressed as,

$$L_p = 20log\frac{p_{rms}}{p_{ref}} \tag{2.2}$$

where L_p is the sound pressure level measured in decibels (dB), p_{rms} is the root mean square pressure level of the incoming sound, and p_{ref} is 20 μPa, the threshold of human hearing in air [6].

2.1.2 Equations of Motion

Fluid motion can be described generally by equations of conservation of mass and conservation of momentum performed on infinitesimally small fluid volumes. Considering a fluid with density ρ, velocity $\vec{v}$, and pressure p. Conservation of mass yields,

$$\frac{1}{\rho}\frac{\partial \rho}{\partial t} + \nabla \cdot \vec{v} + = 0 \tag{2.3}$$

and the conservation of momentum reduces to the Navier-Stokes equations given by,

$$\rho\frac{D\vec{v}}{Dt} = -\nabla p + \nabla \cdot \sigma_{ij} + \vec{F}$$

where $\vec{F}$ is an external force such as gravity [7]. These equations of fluid motion also govern the propagation of sound. Common simplifications to the Navier-Stokes equations assume incompressible flow to allow for solutions to be easily determined. Such a simplification cannot be applied in the case of sound, since the propagation of the wave depends on the change of density of the medium. For an ideal gas, the fluid can be considered isentropic and inviscid, and in circumstances with zero mean flow, the motion of a sound wave travelling through the medium can be described by the homogeneous wave equation,

$$\nabla^2 p - \frac{1}{c^2}\frac{\partial^2 \rho}{\partial t^2} = 0 \tag{2.4}$$

which is a one-dimensional equation, revealing that pressure fluctuation occurs in the direction of wave propagation [6]. This equation describes the propagation of sound but does not include generation by sound sources. Sound sources cause deviation from the homogeneous wave equation, resulting in the inhomogeneous wave equation,

$$\left(\frac{\partial^2}{c^2 \partial t^2} - \nabla^2\right) p = \mathcal{F}(x,t) \tag{2.5}$$

where $\mathcal{F}(x,t)$ represents a general pressure source [8]. The sound field is therefore distinct from the source field. When the source is known, and appropriate initial and boundary conditions are applied, the sound field can be uniquely solved. However, knowledge of the sound field does not uniquely determine the sound source. This is an important consideration for application of the beamforming technique. The physical nature of potential sound sources in beamforming must therefore be assumed. There are multiple source types to consider, with monopole, dipole, and quadrupole sources commonly encountered in aeroacoustics [8].

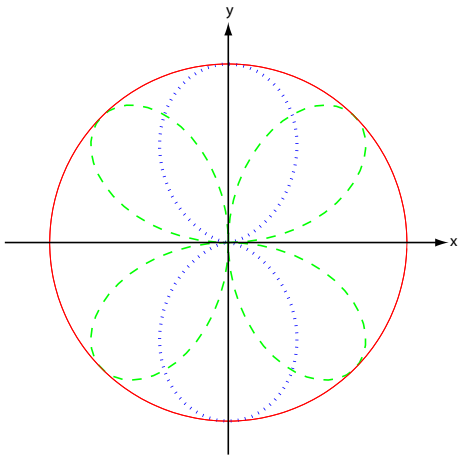

Figure 2.1: Multipole source directivity — Monopole ··· Dipole – – Quadrupole

Referring to the directivity patterns shown in Figure 2.1, a monopole can be thought of as a pulsating, compact sphere radiating equally in all directions. In beamforming, potential sources are considered to be monopoles. A dipole can be considered two oppositely phased monopoles located adjacent to one another or a monopole translating back and forth between two positions. Dipoles are a common source type in aeroacoustics, often present as vortical structures resulting from the interaction of a fluid and a solid body. Dipoles differ from monopoles in that they: have non-uniform directivity with a figure eight radiation pattern; are less efficient radiators due to destructive interference between signals emitted at each pole; and behave differently in the near and far fields. In the near field, dipoles have a strong $1/r^2$ dependence and in the far field exhibit primarily a $1/r$ reduction in amplitude. Quadrupoles can be thought of as adjacent dipoles or perpendicular dipoles, which would create a cloverleaf shaped radiation pattern. Quadrupoles are com-

monly produced by turbulent flow structures, and like dipoles, have a strong distinction between near field and far field radiation and are very inefficient radiators.

2.2 Beamforming

Beamforming is a processing technique used for processing acoustic measurements made simultaneously with all microphones in a microphone array. The following sections provide an introduction to the common algorithms employed in both time and frequency domains. A comparison of the two methods is now presented, followed by refinements to the algorithms to improve the value of processed results. A discussion of the effect of moving sources on beamforming results in included.

2.2.1 Time Domain Beamforming

The analysis presented here should serve as an introduction to the algorithm in its simplest form: delay-and-sum beamforming in the time domain. The use of a beamforming algorithm provides the array with directionality, allowing it to "steer" to various points in space using only post-processing algorithms [9]. The principle of delay-and-sum relies on the fact that sound travels predictably in the free-field according to solutions to the wave equation. Microphone signals collected in such a field can be manipulated through time delays and amplitude adjustments to reconstruct the original signal at the source.

Consider a microphone array of M elements at locations

$$\vec{x}_m,\ m = 1, 2, \ldots, M \tag{2.6}$$

where $\vec{x}_m = (x, y, z)$ is a spatial vector with respect to the array's geometric centre or origin. In any array, the array origin is located at the geometric centre, such that

$$\sum_{m=1}^{M} \vec{x}_m = \vec{0} \tag{2.7}$$

and there is no requirement for a microphone to be located at the origin. Now consider that this microphone array has collected signals from a sound field $s(t)$ containing a single monopole point source at x_s, an unknown location. The signal received at any point in space x, as provided by the spherically symmetric solution to the wave equation is given by

$$y(t) = \frac{s(t - r'/c)}{r'} \tag{2.8}$$

where $r' = |\vec{x} - \vec{x}_s|$ is the distance from the arbitrary point to the source. Now since the source location is unknown it is not possible to determine the value of r' and therefore

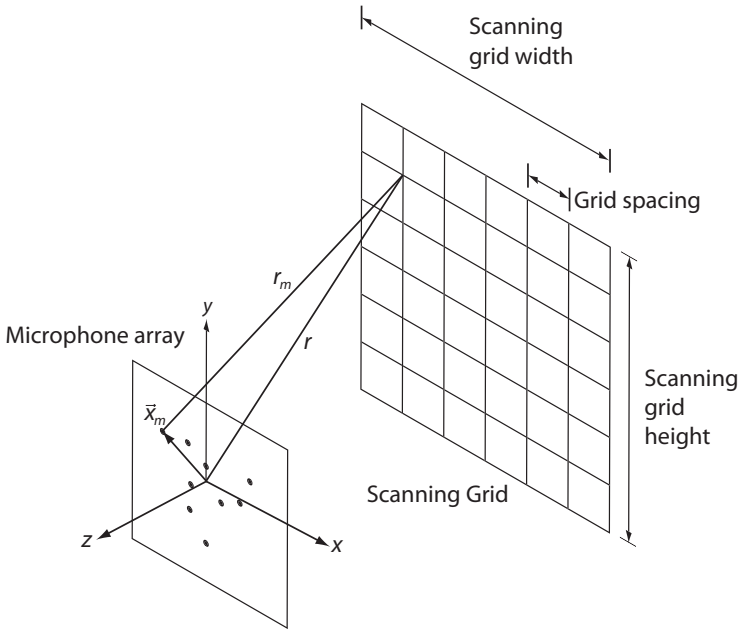

Figure 2.2: Beamforming algorithm coordinate definition

determine the pressure signal at an arbitrary position. Therein lies the value of the beamforming technique. By identifying a grid of scanning points on a plane in space where the source is known to be located but within which its exact position is unknown, the algorithm can be run iteratively for each point in the grid, assuming it to be the source location. For any scanning position, under the assumption that the source is located at that same position, the microphone signals $y_m(t)$ can be appropriately scaled and time-shifted according to the respective distances to the scan location, microphone locations, and array centre, which would allow the equivalent signal at the array centre to be reconstructed. This is the fundamental principle of delay-and-sum beamforming, which provides the equivalent microphone signal at the array as described mathematically by,

$$z(t) = \frac{1}{M} \sum_{m=1}^{M} w_m y_m (t - \triangle t_m) \tag{2.9}$$

where w_m is the microphone weighting factor and $\triangle t_m$ is the microphone time delay [10]. The magnitude of $z(t)$ is normalized by dividing by the number of microphones, M, to provide the representative amplitude of a signal received by a single microphone at the array centre.

Referring to Figure 2.2, the necessary time delay for a given microphone signal is referenced to the distance travelled to the array centre and is found by,

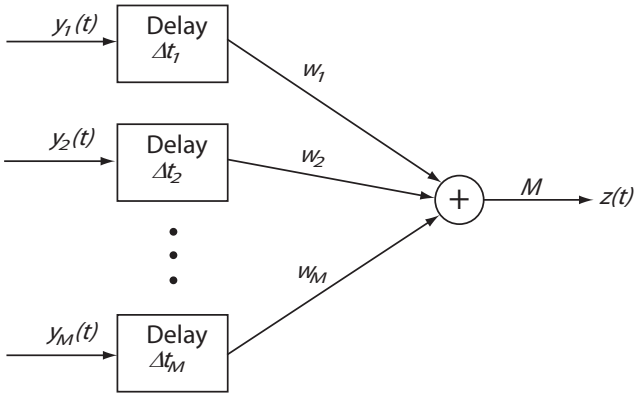

Figure 2.3: Delay-and-sum algorithm block diagram (adapted from Johnson and Dudgeon [10])

$$\triangle t_m = \frac{r - r_m}{c} \tag{2.10}$$

where r is the distance from the array centre to the scanning position and r_m is the distance from the m^{th} microphone to the scanning position. The weighting factor for a given microphone can be calculated by

$$w_m = \frac{r_m}{r} \tag{2.11}$$

which can then be used to scale the pressure amplitudes of each microphone signal.

In practice, the delay-and-sum algorithm is performed by first identifying a scanning grid on a plane where a source is thought to be located. The algorithm is then run for each scan position as shown in Figure 2.3.

Following the delay-and-sum procedure, each scan position the sum of all corresponding manipulated microphone signals normalized by the total number of microphones. For a single source, provided the scanning grid is adequately defined in terms of location and spatial resolution, there should exist one scan point which will coincide with the source location. At this location, the weighted signals will be equal in amplitude and the time delays applied to each signal will align all microphone signals. When summed, the signals will add constructively and created a time-aligned signal with amplitude equal to

$$z\left(t\right) = s_0\left(t\right) \tag{2.12}$$

where $s_0\left(t\right)$ is the magnitude of a signal received at the array centre. For scan locations not coinciding with the source location, the summed signals will have random time-alignment

and unequal amplitudes. When summed, these signals will create a signal with low amplitude and random time-alignment. At grid points near the source location, the signals are nearly time-aligned and therefore add constructively to a greater degree. Scan points farther from the source location have a higher prevalence of destructive interference and produce a signal of much lower amplitude when summed. The output of beamforming is a source map of the squared sound pressure levels as a function of scan position, which provides visual representation of sources in the sound field. The difference in sound pressure level from the highest value in the source map to the lowest value is often exceedingly large, and can lead to difficulty in interpretation of the source map. Therefore, source maps are typically presented over a limited sound pressure level range, known as the dynamic range, measured downward from the maximum sound pressure level. An example source map with 9 dB dynamic range produced in response to a single sound source is shown in Figure 2.4.

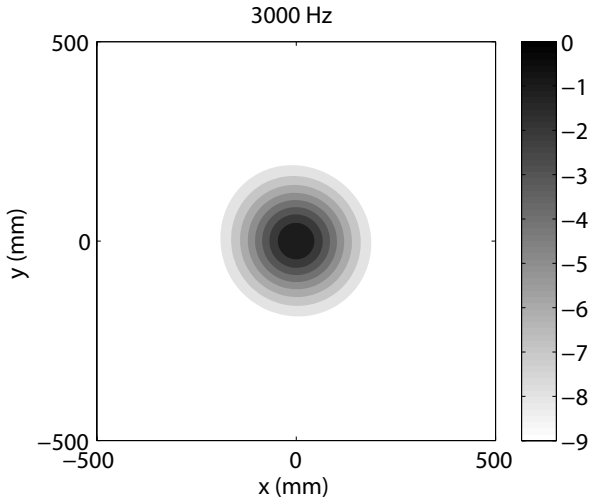

Figure 2.4: Example 3 kHz source map – 9 dB dynamic range

Although the technique above considered a single monopole source, this technique can be applied to any number of sources provided they radiate coherently toward the array. It can also be used for dipoles, quadrupoles, or higher order multipoles, provided their pressure is inversely proportional to propagation distance in the far-field [11]. In defining a grid, the array does however sample only a portion of space and is therefore unable to account for all of the energy in the field. Therefore the technique can not accurately reconstruct the true amplitude of the source [12]. Additional techniques can be applied to provide a more accurate representation of the true sound pressure level [13, 14]; however, such methods are not addressed in this thesis. Furthermore, the technique requires the assumption that the array is capable of sampling the sound field without interfering with

it. Reflections and diffraction due to the array structure are unavoidable and these can influence the measured sound field.

2.2.2 Frequency Domain Beamforming

While the algorithm has been presented in the time domain, beamforming can be readily adapted to the frequency domain by recognizing that a time delay in the time domain can be expressed as a phase delay in the frequency domain. Again, a scanning grid is defined and the algorithm demonstrated here is applied at each grid point [15]. The coordinate and distance definitions are the same as those defined in Figure 2.2. The time series, composed of data discretely sampled at intervals of $\triangle t$, is divided into K blocks of length T_b. A Fast Fourier Transform (FFT) is performed on each data set. The algorithm in the frequency domain begins by obtaining the cross spectral matrix (CSM) for each data set. Each element in the cross spectral matrix is a complex spectrum with bandwidth $\triangle f = 1/T_b$ obtained by,

$$G_{mm'}(f) = \frac{1}{w_s K T_b} \sum_{k=1}^{K} \left[P^*_{mk}(f, T)\, P_{m'k}(f, T_b) \right] \tag{2.13}$$

where $P^*_{mk}(f, T_b)$ and $P_{m'k}(f, T_b)$ are the complex pairs (noting the complex conjugate) obtained from the FFT of the signals of microphones m and m' in block k [15]. The summation provides an average over all blocks for a total signal length of KT_b, and includes a weighting constant w_s to account for a windowing function. Typically, a Hamming window is used to minimize spectral leakage in each block [16]. The cross spectral matrix is therefore composed of

$$\hat{G} = \begin{bmatrix} G_{11} & G_{12} & \cdots & G_{1m_0} \\ G_{21} & G_{22} & & \vdots \\ \vdots & & \ddots & \vdots \\ G_{m_0 1} & \cdots & \cdots & G_{MM_0} \end{bmatrix} \tag{2.14}$$

where each element is the cross-correlation of each possible microphone combination from Equation 2.13. The cross spectral matrix is steered to each grid point similar to the time domain method, using matrix multiplication with steering vectors,

$$Y(\hat{e}) = \frac{\hat{e}^T \hat{G} \hat{e}}{M^2} \tag{2.15}$$

where T denotes the complex conjugate transpose, $Y(\hat{e})$ is the mean pressure squared per frequency bin normalized by the number of microphones squared to obtain the response of a single microphone at the array centre, and $\hat{e}$ is the steering vector. The steering vector

is a column vector $\hat{e} = \text{col}\left[\begin{array}{cccc} e_1 & e_2 & \cdots & e_{m_0} \end{array}\right]$ where

$$e_m = \frac{r_m}{r} e^{j2\pi f \frac{r_m}{c}} \tag{2.16}$$

is the value of each element in the column vector [15].

Obtaining a power spectrum from the resulting signals for each scan point yields the sound pressure level across the scanning grid at any frequency of interest. Typically, one-third octave bands are used for frequency ranges plotted in source maps. These bands are calculated by summing the spectral values in each frequency bin in the band. Since these spectral values are measured in decibels, they must be added logarithmically; that is, the root mean square addition of the pressure in each band.

2.2.3 Comparison of Time and Frequency Domain Methods

A comparison of the two beamforming methods reveals advantages and disadvantages of each. Provided the data acquisition and processing hardware are capable, beamforming in the time domain could be performed on a continuous time signal. However due to cost and simplicity, the technique is more commonly performed on data sampled digitally at a high frequency. Even with a high sampling rate, the available delay times are now discretized. For a given scan position, the physical time delay will likely not correspond to the integer values provided in the digital reconstruction of the microphone signal. Since phase accuracy is vital to the success of the delay-and-sum technique, small errors in time alignment can limit the array's performance. Increasing the sampling frequency by interpolation is an option but adds considerably to the computation time. Delay-and-sum does offer the advantage that the reconstructed time signals for each scan position are available for use, and that once the process is performed, source maps can be generated quickly for any frequency range of interest.

Beamforming in the frequency domain first transforms the time signals recorded by each microphone into bins in the frequency domain, typically through the use of an FFT. Beamforming is then applied to the narrowband spectral results. One immediate advantage is that beamforming can be applied to bins within a frequency range of interest rather than the whole signal, which can result in significantly lower computation times. Additionally, the computational requirements are generally much lower in the frequency domain, since a small number of simple matrix manipulations are used to generate the source map, whereas in the time domain each entry in the time-series must be individually manipulated for each scan point. Furthermore, refinements to conventional beamforming and higher-order algorithms to improve the effectiveness of the source maps can be implemented without significant additional computational requirements. One disadvantage of the frequency domain approach is that the immediate conversion of the time signals into blocks in the frequency domain eliminates the ability to investigate the reconstructed time

signals, should that be desired. Furthermore, accounting for the movement of sources must be performed in the time domain as detailed in Section 2.2.5.

Ultimately, processing used in this thesis uses conventional beamforming in the frequency domain with a number of refinements, the details of which can be found in Orlando [17]. The time domain beamforming algorithm was also completed to allow for the source signal of a moving source to be reconstructed, although the implementation was unsuccessful due to hardware limitations described in Section 6.4.

2.2.4 Refinements to Beamforming

Diagonal Removal

It is evident that each term along the diagonal in the cross spectral matrix in Equation 2.14 is the autocorrelation. Noise is present in any microphone signal due to electrical or self-induced noise. This noise is uncorrelated between any two microphones. However, along the diagonal of the CSM each microphone is correlated with itself and the noise is therefore also correlated. The diagonal is commonly removed from the CSM and replaced with an empty diagonal to improve the signal-to-noise ratio. The output of beamforming with diagonal removal becomes,

$$Y\left(\hat{e}\right) = \frac{\hat{e}^T \hat{G}_{diag=0} \hat{e}}{M^2 - M} \tag{2.17}$$

to account for the accompanying decrease in the overall magnitude of the CSM [18]. It should be noted that while this method improves the array's ability to distinguish physical sources, it can lead to negative pressure squared values in areas of source maps with lower sound pressure levels since it eliminates some of the signal at each scan point.

While diagonal removal can obviously only be performed in the frequency domain since it requires the use of a cross spectral matrix, a similar approach can be utilized on the time domain signals obtained from delay-and-sum beamforming to improve the signal-to-noise ratio. Since an FFT is required to produce the source maps from the reconstructed signals in delay-and-sum beamforming, this spectral information can be manipulated to remove the incoherent noise which is amplified by autocorrelation [19]. The reconstructed source amplitude obtained from the FFT can be written as,

$$\bar{a}\left(\bar{z}\right) = \sum_{m=1}^{M} \bar{a}_m\left(\bar{z}_m\right) \tag{2.18}$$

and the auto-powers can be obtained from the cross power matrix,

$$\bar{A} = \frac{1}{2M^2} \sum_{m=1}^{M} \sum_{m'=1}^{M} \bar{a}_m\left(\bar{z}_m\right) \bar{a}^*_{m'}\left(\bar{z}_{m'}\right) \tag{2.19}$$

allowing for the equivalent of diagonal removal by removing terms where $m = m'$ and normalizing by $M^2 - M$ rather than M^2.

Shading

Measurements made with a microphone array can suffer from coherence issues particularly at higher frequencies as microphones at the inner and outer extremes may have little or no correlation with each other. The source amplitude in the source map will therefore be underrepresented. One method of improving the validity of the source maps is to use an array aperture, the diameter of the array measured between the outermost sensors, which decreases with source frequency [18]. In effect, when performing beamforming at a high frequency, signals from microphones located at distances greater than a determined aperture are not included. This approach can be effective with arrays having large physical dimensions or high sensor counts.

Flow

Acoustic measurements made in the presence of air flow, such as in a wind tunnel, can lead to inaccurate localization of sources. In a closed-loop wind tunnel, the microphone must be placed in the test section, and therefore in the flow. This has implications on the path taken from source to array as the pressure signal is convected along with the flow. The effect of fluid motion can be corrected to a set of retarded coordinates provided the flow speed is known [11].

Using an open-jet tunnel, the microphone is placed out of the flow, so in addition to convection due to flow within the jet, there exists a shear layer between the source and array which causes refraction in the propagation of sound waves. The effect of the shear layer is commonly quantified using Snell's law in Amiet's method [20]. Considering a shear layer to be a thin boundary between quiescent air and freestream flow as shown in Figure 2.5, the direction of sound propagation is altered by refraction such that,

$$\frac{c_1}{\cos\varphi_1} = \frac{c_2}{\cos\varphi_2} \tag{2.20}$$

where c_1 and c_2 are the speeds of sound in the respective propagation medium calculated as the addition of the speed of sound in the medium and the component of flow in the direction of propagation. The phase of the microphone signals can then be corrected by accounting for the additional distance travelled due to the change in propagation direction from each grid point to each microphone [18].

Higher Order Algorithms

Additional refinements to the beamforming process have been introduced recently that aim to improve source identification and location. Examples of these include methods to improve source resolution and distinguish reflected sources from physical sources [18,21–25]. These algorithms are beyond the scope of this thesis and were not implemented in the processing experimental results.

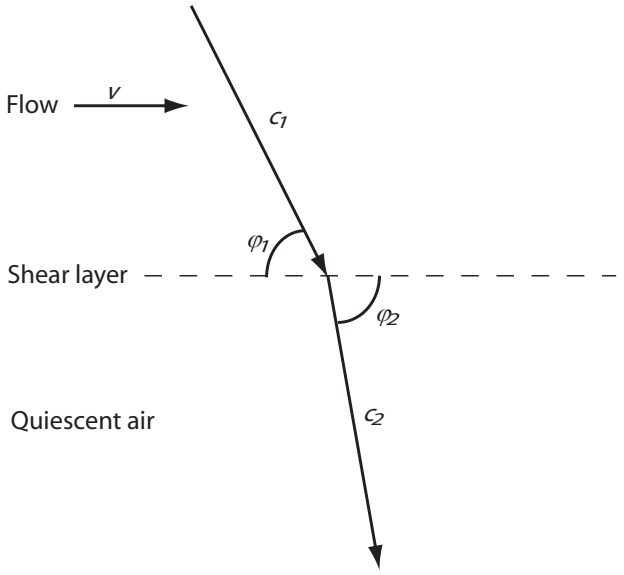

Figure 2.5: Refraction of sound due to shear layer

2.2.5 Moving Sources

A number of issues arise when a sound source is moving. Source maps of a moving source reveal a source which appears to spread out since it is averaged over the length of the signal or block. Furthermore, when a sound source is moving, the radiated pressure field changes with respect to a stationary observer due to the Doppler effect. A source with frequency f approaching an observer at velocity v emits a signal which at the beginning of the period $t = 1/f$ travels from source to observer a distance of ct. However by the end of the period, the source has travelled a distance of vt. The distance between the crests in the signal is therefore reduced by vt yielding,

$$\lambda = \frac{c - v}{f} \tag{2.21}$$

the perceived wavelength due to motion. The frequency of the signal received by the observer is not the frequency of the signal but rather,

$$f_d = \frac{c}{\lambda} = \frac{fc}{c - \lambda} = \frac{f}{1 - \frac{v}{c}} \tag{2.22}$$

the frequency corresponding to the adjusted wavelength. For a source moving toward an observer, the perceived frequency is higher than the source frequency. The converse is true for a source moving away from an observer. This has considerable implications for beamforming, since a moving source at a fixed frequency is perceived as having a variable

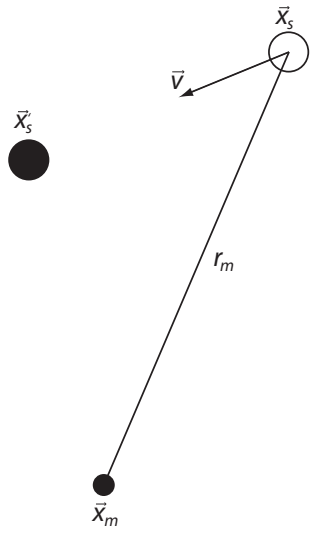

Figure 2.6: Demonstration of moving source

frequency depending on its velocity, location, and microphone position. In the time domain, this frequency shift has the effect of reducing time alignment between microphone signals. In the frequency domain, the frequency shift can move the source frequency across various narrowband frequency bins.

To overcome these issues the microphone signals can be reconstructed, or dedopplerized, accounting for the movement of the source, by using scanning grids which move along with the source, provided the source motion vector is known. Dedopplerization can only be performed in the time domain since it requires that the the time signals of each microphone be reconstructed for each grid point. Beamforming becomes significantly more complicated and computationally expensive when taking a moving source into account. The following analysis presents the approach for dedopplerizing a source moving with known trajectory [11, 26].

Consider a source at position $\vec{x}_s$, moving with velocity $\vec{v}$, as shown in Figure 2.6. Without movement the signal would arrive at microphone position $\vec{x}_m$ in $\triangle t$ seconds. Due to the movement, the source has moved to position $\vec{x}_s'$ during this time.

The transfer function relating the source signal and microphone pressure signal can be expressed as,

$$\frac{y\left(\vec{x}, t+\triangle t\right)}{s\left(t\right)} = \frac{1}{4\pi\left[c\triangle t - \frac{1}{c}\vec{v}\cdot\left(\vec{x}_m - \vec{x}_s\right)\right]} \tag{2.23}$$

with the factor 4π included to reconstruct the amplitude of the monopole source, and where $\triangle t$ is given by,

$$\triangle t = \frac{1}{c\left(1-|\vec{M}|^2\right)^2}\left(-\vec{M}\cdot(\vec{x}_m-\vec{x}_s)+\sqrt{\left(\vec{M}\cdot(\vec{x}_m-\vec{x}_s)\right)^2+\left(1-|\vec{M}|^2\right)^2|\vec{x}_m-\vec{x}_s|^2}\right) \tag{2.24}$$

where $\vec{M}$, given by,

$$\vec{M} = \frac{\vec{v}}{c} \tag{2.25}$$

is the Mach number vector corresponding to the source motion. The reconstructed source amplitude can then be calculated using the transfer function in Equation 2.23 as the steering function in delay-and-sum beamforming,

$$s(t) = \frac{1}{M}\sum_{m=1}^{M} 4\pi\left[c\triangle t - \frac{1}{c}\vec{v}\cdot(\vec{x}_m-\vec{x}_s)\right] y_m(t+\triangle t_m) \tag{2.26}$$

selecting t, a series of equally spaced times to obtain the dedopplerized signal. The times $t+\triangle t_m$ will not coincide with measurement sampling times and will not be equally spaced since the source is moving, so the signals must be interpolated to obtain the microphone signals at the required times. Due to the additional processing required on each discretized sample of each microphone's time signal, the technique requires considerable computational resources.

2.3 Microphone Arrays

Phased arrays have long been used in astronomy, seismology, and sonar applications. More recently phased arrays containing microphones as transducers have become a vital tool in aeroacoustic testing. The implementation of a microphone array takes advantage of the properties of sound propagation in the acoustic far-field, using the variations in amplitude and phase measured by the various microphones in the array. Utilizing beamforming as a post-processing technique, the array can be focused to chosen spatial locations by manipulating the phase and amplitude of measured signals in either the time or frequency domains. In measuring a sound field, there should exist correlation in the signals recorded by all microphones in the array. The correlated signal will be amplified above any uncorrelated portions of the signal, such as self-noise due to flow passing over the microphone. A microphone array offers directivity to measurements and allows significant improvement in the signal-to-noise ratio of measurements of a source at a given spatial location, allowing for improved efficacy of acoustic measurements in otherwise troublesome measuring environments. The beamforming technique is the basis of spatially locating individual acoustic emissions from a source, since it offers directivity not possible with a single microphone.

Microphone arrays for aeroacoustic measurements have become popular due to their ability to spatially identify acoustic sources. This has led to their use in controlled aeroacoustic testing in numerous applications, including measurements of scale model aircraft [19, 27, 28], aircraft landing gear [29], jet engines [25, 30], two-dimensional airfoils [31–35], flaps [36] and slats [37], trains [38], helicopter rotors [39], scale-model wind turbines [40, 41], among numerous other aeroacoustic tests. However, the use of microphone arrays extends beyond anechoic environments and wind tunnel tests; large arrays on the order of tens of metres incorporating up to hundreds of microphones have been used to capture sound emissions from aircraft flyovers [42, 43] and full-scale wind turbines in operation [3, 44]. Such tests are able to visually demonstrate the location of acoustic sources, enabling the mechanisms of sound production to be understood and reduced in future designs.

2.3.1 Array Considerations

The primary factors affecting the response of the array are the array layout, source frequency, distance from the source, and the algorithm used for processing. These factors contribute to the usefulness of the source map. The source map contains the main beam, or mainlobe, and secondary beams called sidelobes. The mainlobe comprises the physical acoustic signal captured by the microphones, while the sidelobes are present as artifacts of the finite number of microphones used in the array layout and the beamforming algorithm used, and do not contribute meaningfully to the desired output. An example three-dimensional source map demonstrating the terminology and array output is shown in Figure 2.7.

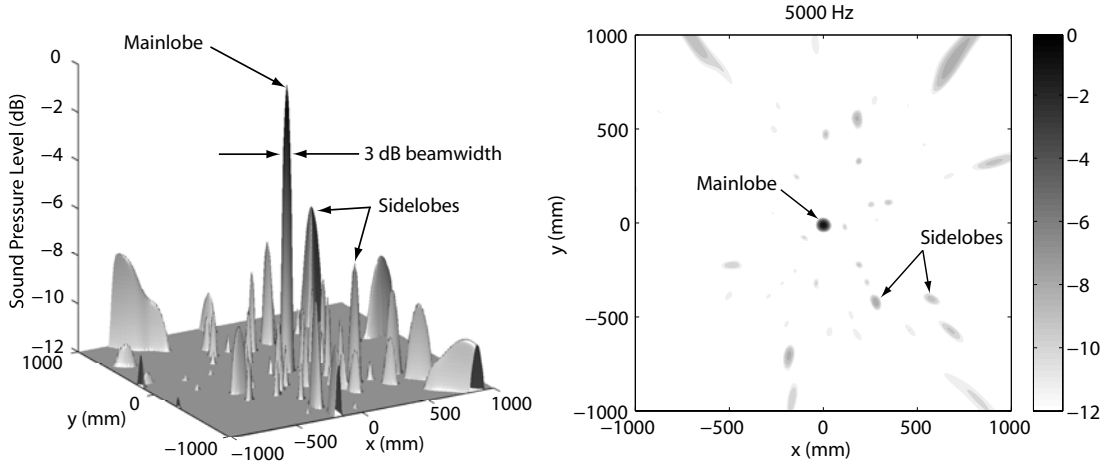

Figure 2.7: Example 5 kHz source shown as three-dimensional source map (left) and two-dimensional source map (right)

Source maps can be presented in two or three dimensions depending on the required interpretation. Source maps in this thesis will be primarily demonstrated as contour maps in two dimensions. The location of the mainlobe peak corresponds with the source location, while its width gives an indication of the array's spatial resolution. Sources can only be uniquely distinguished if they are positioned at a distance greater than the beamwidth from each other. The beamwidth therefore governs the spatial resolution of the array, with a smaller beamwidth being desired from the output of any array layout. A metric for the performance of the array is described by the mainlobe beamwidth at the -3 dB contour. Since the mainlobe is ideally circular but is commonly found to be elongated or non-uniform in source maps, the beamwidth is commonly calculated by determining the diameter of a circle which would enclose the same area as the area enclosed by the -3 dB contour.

At a given source distance, beamwidth is inversely proportional to frequency,

$$BW \propto \frac{1}{f} \tag{2.27}$$

and at a given frequency, beamwidth is proportional to source distance,

$$BW \propto z \tag{2.28}$$

such that array resolution improves with increasing frequency and decreasing distance to the source. Although resolution improves at higher frequencies, the number of sidelobes present in a source map also increases. This is demonstrated in Figure 2.8 for a 4 kHz and 10 kHz theoretical sound source located at the same position.

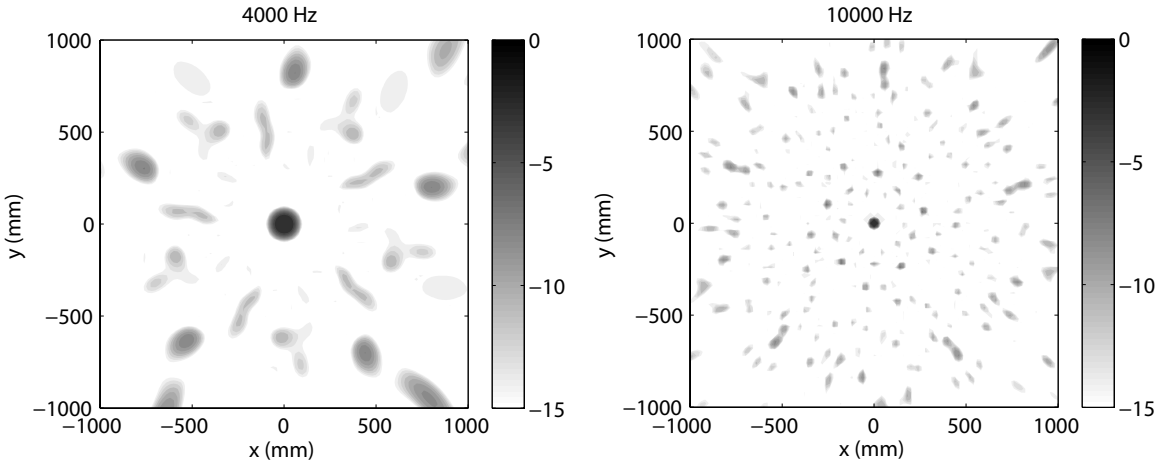

Figure 2.8: Source maps for modelled 4 kHz and 10 kHz sound source at 1 m along z-axis

The mainlobe has a certain width due to partial time-alignment of summed signals near the peak. Ideally at the peak, the signals are perfectly in phase with each other. Moving away from the peak, the signals maintain some alignment which diminishes at scan locations farther away from the peak. The beamwidth decreases with increasing frequency which improves array resolution with increasing frequency. It is intuitive that the beamwidth should decrease with increasing frequency since summed signals maintain less phase coherence with each other due to the decreased wavelength and therefore do not add constructively as readily, causing the resultant amplitude to decrease more rapidly across the grid. Lower frequency signals maintain higher levels of coherence among microphones due to their long wavelengths and therefore maintain much greater summed signal amplitudes farther from the peak location.

It is also important to note that the spatial resolution of the beamforming technique is not as effective in resolving sources at different positions in the depth direction. This provides advantages or disadvantages depending on the measurement scenario. In choosing a scanning plane at a known distance, sources at slightly different positions in the depth direction will be detected almost equally well. This can be beneficial if the source position is not precisely known or if the source is moving in and out of the scanning plane, for instance with a yawed wind turbine. The downside of such poor resolution is that sources travelling out of the scan plane are not easily distinguished as moving sources in the plane. Consequently performance of a two-dimensional planar array is best when the array, scan plane, and relevant source plane are parallel.

Aside from the obvious attraction of locating sources in a field through beamforming, a microphone array offers the ability to improve the signal-to-noise ratio (SNR) over a single microphone, and can provide amplification of signals radiating from a specific direction. The gain of the array is the improvement in the SNR of the array compared to the SNR of the sensor and can be expressed as,

$$G = \frac{SNR_{array}}{SNR_{sensor}} = \frac{\left(\sum_{m=1}^{M} w_m\right)^2}{\left(\sum_{m=1}^{M} w_m^2\right)} \tag{2.29}$$

where w_m is calculated as in Equation 2.11 [10]. As the source moves away from the array the weighting factor approaches unity and the gain can be simplified to its maximum, M. The maximum gain is

$$G = 10log\,(M) \tag{2.30}$$

where G is measured in decibels.

Sidelobes can be difficult to distinguish from mainlobes, particularly when the sound field is completely unknown. That is, sources that are different in amplitude by more than the difference in amplitude between the mainlobe and highest sidelobe cannot be resolved as

physical sources. The sidelobes therefore represent the array's capability in filtering signals arriving at the array from directions other than the steering vector [9]. It is desirable to suppress sidelobes to improve the array's signal-to-noise ratio. Sidelobes can be suppressed to an extent through array layout and refinements to the beamforming algorithm. The goal of the array design is to minimize the beamwidth and maximize the dynamic range over a broad range of frequencies while operating under the constraints of sensor count, sensor size, array size, and microphone frequency range. Sidelobes also arise from spatial aliasing, which is a consequence of spatially undersampling; that is, using an insufficient number or inadequately arranged sensors in the aperture of the array. Much like temporal aliasing in which the sampling rate is insufficient to distinguish between multiple frequency components, spatial aliasing results in an inability to distinguish multiple propagation directions. Spatial aliasing reveals itself as sidelobes on a source map and becomes more prevalent at higher frequencies. The classical Nyquist criterion [45] used in the time domain is also valid in the spatial domain, such that spatial sampling is performed at intervals less than a half-wavelength of the frequency under test. Therefore, in order to resolve high frequencies, without spatial aliasing, microphones must be located in close proximity to one another. However, the array must be capable of resolving a wide range of frequencies and lower frequencies can only be adequately resolved by having a large array aperture. Trying to accommodate both of these requirements leads to large arrays with numerous sensors, which can be cost prohibitive.

A further consideration of spatial aliasing has to do with arrays employing equal intersensor spacings. Sidelobes result from the summation of coherent signals at angles other than the intended steering angle. The accumulation of these signals can be prevented by eliminating equivalent vectors between sensors. It is therefore desirable to have array geometries where there are no redundant intersensor vectors. For any given array with coordinates defined in Equation 2.6, there exists a coarray consisting of all possible vectors between microphones expressed by,

$$\vec{x}_p = \vec{x}_m - \vec{x}_n, \tag{2.31}$$

where $m = 1, 2, \ldots, M$ and $n = 1, 2, \ldots, M$. There are a possible $M^2 - M$ non-zero vectors. Sidelobe suppression is greatest when none of the non-zero vectors are redundant [9].

2.3.2 Array Geometries

Various planar array geometries are available to balance the requirements of spatial resolution and signal-to-noise ratio while adhering to physical size and sensor count limitations. Arrays can also be constructed in three-dimensions to aid in characterizing highly complex three-dimensional source fields. However, these are beyond the scope of the work undertaken in this thesis. An introduction to common planar geometries follows.

Linear Arrays

Arrays consisting of microphones arranged on one axis only are referred to as linear arrays. Such arrays can be a useful tool in improving the signal-to-noise ratio over a single microphone. Linear arrays are not particularly effective at locating sound sources off axis, so their use is typically limited to identifying the location of a sound source along a fixed axis. The applications of a linear array are limited in aeroacoustic testing but could have suitable effectiveness in two-dimensional closed-loop wind tunnel testing, for identifying the location of emissions from a two-dimensional aeroacoustic source, such as an airfoil with a constant chord. Linear arrays can be constructed in a regularly spaced pattern, or with variable spacing to create an aperiodic array, in which there are no redundant intersensor vectors within the array aperture.

Rectangular Arrays

Expanding the linear array to two dimensions provides the foundation for the rectangular array. In such an array, sensors are typically positioned at regular intervals in a grid. Equally spaced microphones create issues with sidelobes as the redundant vectors between microphones can lead to the accumulation of signals at angles other than the intended steering angle. Furthermore, equally spacing microphones does not lead to a wide range of intersensor spacings resulting in compromised array performance over a wide frequency range. For these reasons, this type of array can be easily outperformed by other geometries.

Random Arrays

Random arrays are a type of aperiodic array created with a random process to position the sensors. Random arrays are not common in aeroacoustic testing as their performance can theoretically be exceeded using a well-designed aperiodic array, where the sensor locations are geometrically positioned and known. Accurately determining, marking, and aligning the centre of a random array can be cumbersome. Random arrays have been researched extensively and reveal that the sidelobe level is primarily affected by the number of elements in the array [46]. A random array is shown in Figure 2.9.

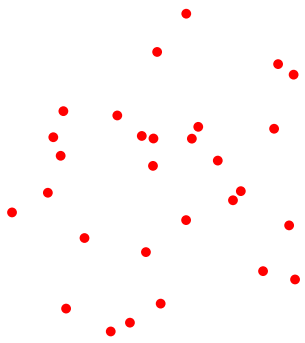

Figure 2.9: Example random array

Circular Arrays

A circular microphone array places microphones in one or more rings which are concentric with the array origin. Circular arrays can be constructed with regular intervals between sensors and be guaranteed to have zero redundancy in intersensor vectors provided the number of elements in each circle is an odd number. Circular arrays offer the ability to have closely spaced sensors to provide high frequency resolution and wide apertures to adequately capture low frequency sources. However, due to the even spacing between sensors in any given ring, these arrays do not offer a wide range of intersensor spacings and therefore may not be suited to resolving sources at all frequencies adequately. A circular array is shown in Figure 2.10.

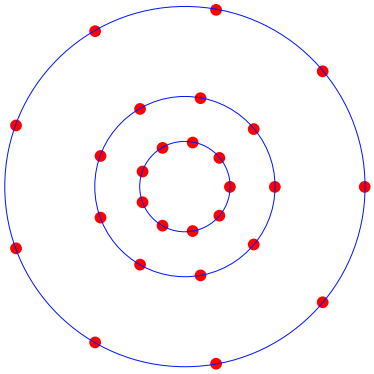

Figure 2.10: Example circular array

Spiral Arrays

Spiral arrays have been introduced to improve sidelobe suppression over a wide range of frequencies [9]. A Dougherty spiral array places sensors along a logarithmic spiral such that the arc length between sensors is equal, which reduces sidelobes resulting from periodicity by guaranteeing that there are no redundant intersensor vectors [47]. This array geometry also accommodates a large aperture with a relatively low sensor count and provides a wide range of intersensor spacings to improve resolution and sidelobe suppression across a wide range of frequencies. An array based on a single logarithmic spiral starting from an initial radius and expanding around the origin to a known final radius can be defined by the desired inner and outer radii, the number of sensors, and the spiral angle which determines the number of revolutions around the origin [9]. Therefore, by establishing the dimensions and sensor count of the array, the spiral angle can be adjusted to provide a wide range of geometries and resulting intersensor spacings. Due to the spreading nature of the spiral, the arrays tend not to be symmetric and have a geometric centre that must be calculated using Equation 2.7, similar to a random array. A spiral array is shown in Figure 2.11.

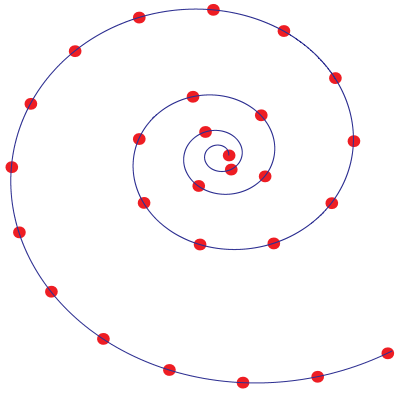

Figure 2.11: Example Dougherty spiral array [47]

Arrays can also be laid out with multiple spiral arms. An Underbrink equal aperture array combines the symmetry of a circular array with the sidelobe suppression of a spiral array [48]. Such an array uses an odd number of arms to guarantee zero redundancy in the co-array of Equation 2.31. Multiple arm spiral arrays can be geometrically defined by the number of microphones per spiral, the number of spiral arms, the inner and outer radii of the array, and the spiral angle [9]. Spiral arrays can also take advantage of unequal spacings between sensors along the spiral to provide spatial weighting, an effect similar to shading as discussed in Section 2.2.4. Equal-arc length spacing leads to greater sensor density near the array origin. By redistributing the microphones along a spiral arm, sensor density can be made more uniform which can help to narrow the beamwidth and maintain sidelobe suppression. The Underbrink equal aperture array takes advantage of this design principle. In this multiple spiral array geometry, a circular aperture is divided into concentric annuli. Each annulus has equal area and the sensors in each spiral are located at the centre of the concentric annuli. An additional inner ring is added to the array to improve high-frequency resolution. A multi-arm spiral array is shown in Figure 2.12.

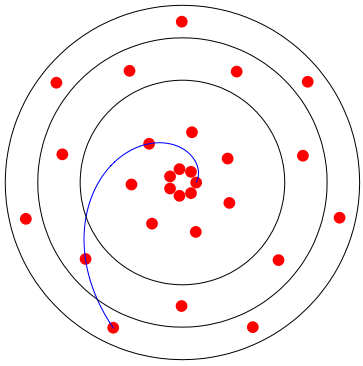

Figure 2.12: Example Underbrink spiral array [48]

2.3.3 Characterizing Array Performance

Assessing Potential Layouts

A convenient method of evaluating an array's performance is to analyze the source map for a modelled source of known frequency located at the origin of the map. A source can be modelled as having an amplitude inversely proportional to distance and a time delay based on the propagation distance. Parameters such as beamwidth and signal-to-noise ratio can be measured and compared for any number of array layouts, altering parameters such as source frequency, grid size and resolution, and distance from the array to reflect actual conditions in which the array will be employed. The source need not be located at the centre of the map, if this does not represent realistic conditions such as in a situation where the facility determines the array mounting location, but resolution is greatest for sources on axis with the array centre as demonstrated in Figure 2.13 for the same sound source at two locations along the same plane.

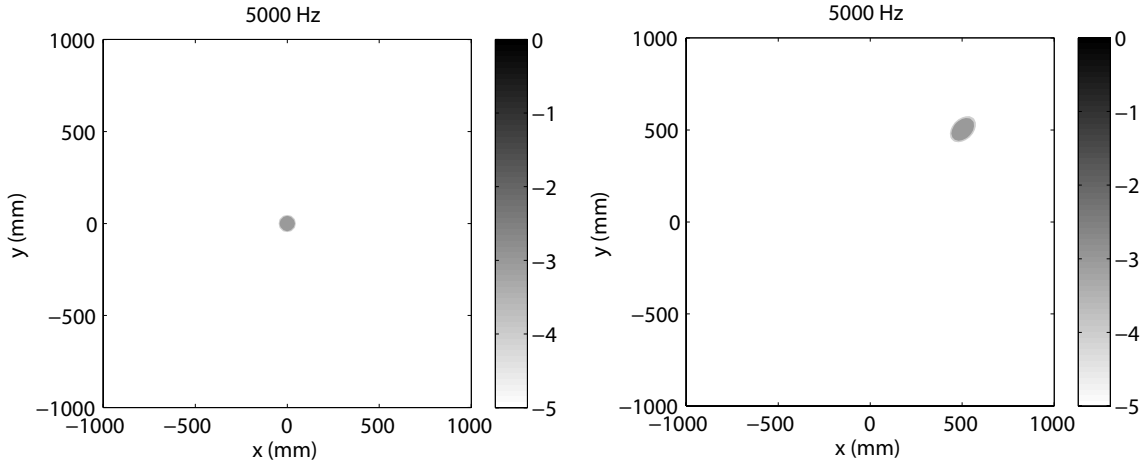

Figure 2.13: Demonstration of decreased off-axis resolution for 5 kHz source at 1 m

Validating Physical Layouts

In assessing the array's performance, the response to a physical source can be measured with respect to the same parameters as above. Since the theoretical model assumes an ideal acoustic environment, the array's measured and theoretical performance can be directly compared with measurements made in an anechoic chamber. A number of methods can be used to quantify the error in the experimental source maps. The following methods are used to validate the array's performance and provide an analysis of error on suitable test configurations.

By comparing the measured maps with the theoretical maps, one measure of error can be ascertained by comparing beamwidths at the -3 dB contour. The contour maps are nor-

malized by their peak value such that their pressure amplitudes can be compared directly. Another method of comparison provides greater detail through a visual representation of the error contained in the measured source maps. By determining the relative error of the pressure found at all scan locations and plotting it as a function of space, the location and magnitude of the relative error between the measured and theoretical maps can be visualized. However, this method provides an additional spatial map and is not easily quantified. To allow for the relative error between theoretical and measured data over the entire source map to be tabulated, the root mean square averaged over the entire source map can be calculated as,

$$E_{rms} = \sqrt{\sum_{n=1}^{N} \frac{(Y_{an} - Y_{tn})^2}{N}} \tag{2.32}$$

where Y_{an} and Y_{tn} are the resultant pressures at each scan location from the measured and theoretical maps respectively.

A final measure of error is to compare the array's ability to spatially locate a known source within the expected margin of error. In situations where the source is precisely placed at a known location in space, the array's measured response should be able to display the mainlobe at this position.

2.4 Wind Turbine Sound Emissions

2.4.1 Noise Generation Mechanisms

While literature involving acoustic testing of rotating wind turbines is limited, testing of a full-scale wind turbine in operation with a 148 element microphone array, with dimensions 15 m by 18 m, has demonstrated that although mechanical noise is audible, aeroacoustic sound emissions dominate across the audible frequency range by an average of 10 dBA as shown in Figure 2.14, which overlays a source map produced from microphone array measurements onto a still image taken from a distance [3].

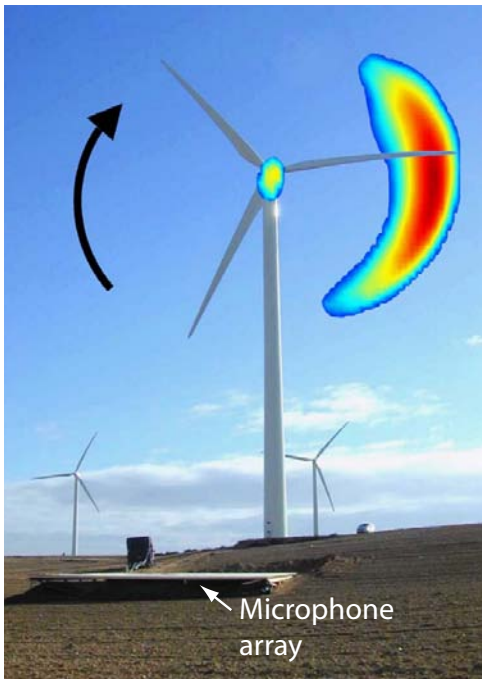

Figure 2.14: Source map from microphone array acoustic testing of Gamesa G58 turbine – 12 dB dynamic range (from Oerlemans et al. [3])

Aeroacoustic emissions have been shown to be proportional to the fifth power of relative speed, such that a rotating turbine produces greater sound output at higher rotational rates and at the outer portions of the rotor where the relative flow velocities are higher [49]. The aeroacoustic emissions produced by the blades result from a number of interactions between the flow and blades. There exist six aeroacoustic mechanisms, demonstrated in Figure 2.15, for a typical airfoil: turbulent boundary layer trailing edge noise, laminar boundary layer vortex shedding noise, separation stall at low angles of attack, large-scale separation or deep stall at high angles of attack, blunt trailing edge vortex shedding, and tip vortex formation noise. In a low-turbulence environment these methods of sound generation are referred to as self-noise, as they result from instabilities in the flow resulting from interactions with the airfoil. Self-noise can be broadband or tonal depending on the production mechanism. Another mechanism of sound production is due to in-flow turbulence interacting with the leading edge of an airfoil. A combination of these mechanisms constitute the overall sound production from an airfoil.

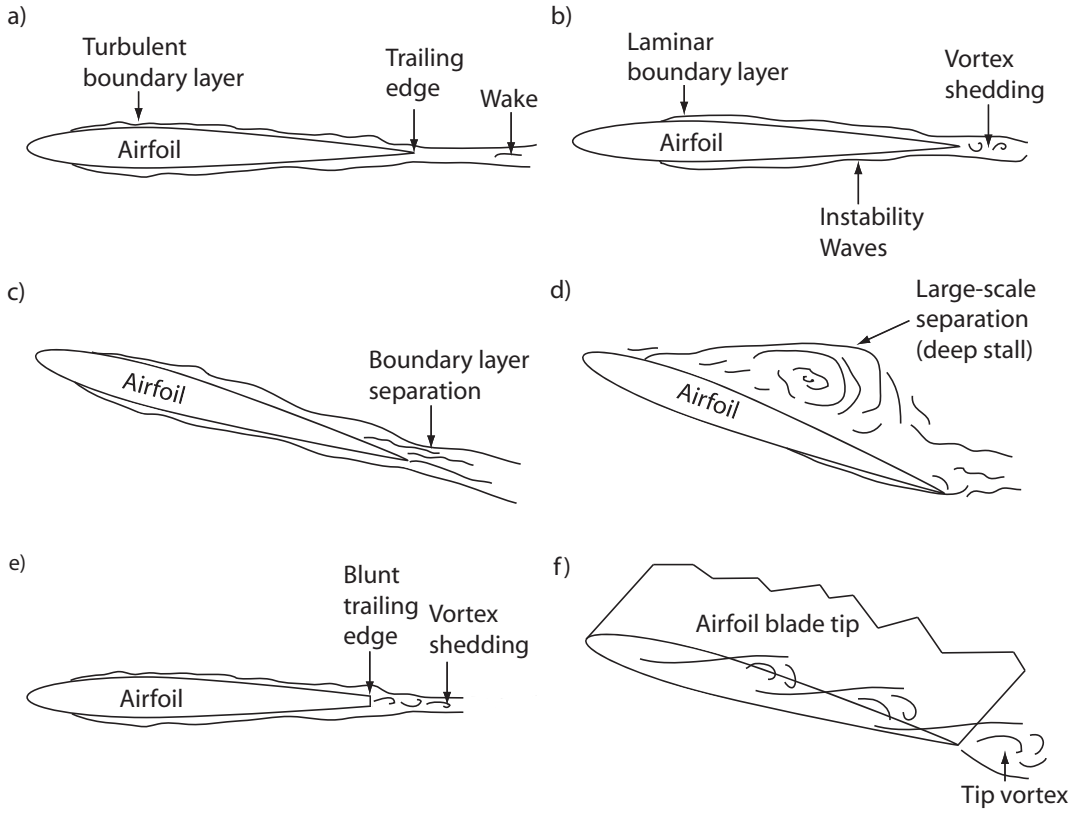

Figure 2.15: Airfoil noise generation mechanisms (adapted from Brooks et al. [49]): a) Turbulent boundary layer – trailing edge; b) Laminar boundary layer – vortex shedding; c) Separation-stall; d) Large-scale separation (deep stall); e) Trailing edge bluntness – vortex-shedding; f) Tip vortex formation

While a rotating wind turbine blade has varying chord, twist, and airfoil shape along its length, small spanwise segments can be modelled as two-dimensional airfoils. For this reason, wind tunnel tests of two-dimensional airfoils can be readily applied to testing wind turbine noise emissions. An example two-dimensional airfoil is shown in Figure 2.16.

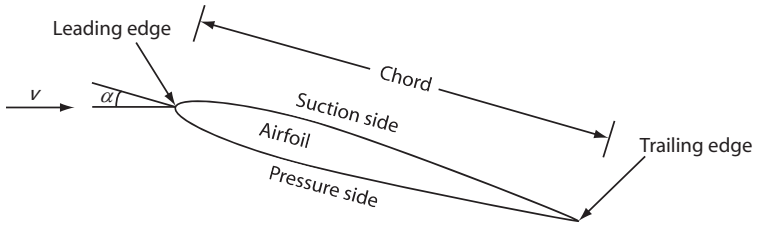

Figure 2.16: Airfoil velocity and angle definitions

Extensive wind tunnel testing of two-dimensional airfoils and field testing of commercial wind turbines has shown that the dominant aeroacoustic emissions originate at the trailing edge [3, 49, 50]. Consequently, for an operating wind turbine, noise emissions are expected to be greatest at the trailing edge and near the tips of the blades where the relative flow velocities are greatest. For small-scale and commercial size wind turbines, the relevant trailing edge noise mechanisms consist of turbulent boundary layer trailing edge noise, laminar boundary layer vortex shedding, boundary layer separation, and blunt trailing edge vortex shedding.

Considering a commercial wind turbine with Reynolds number defined by,

$$Re = \frac{vC}{\nu} \tag{2.33}$$

where v is the relative flow velocity, C is the airfoil chord, and ν is the kinematic viscosity of air, the magnitude of the Reynolds number in the turbine's outer radii is generally greater than 10^6, so a laminar flow has typically transitioned to turbulence at some point along the chord prior to the trailing edge of the blade. The majority of sound emissions on a commercial turbine are therefore produced by broadband turbulent boundary layer trailing edge noise. The amplitude of this mechanism scales with boundary layer thickness [49]. The leading edge of a turbine blade often becomes pitted due to impact with precipitation, dirt, or insects, and this blade erosion can increase the boundary layer thickness, leading to additional sound emissions. The frequency of emissions due to turbulent boundary layer trailing edge noise is proportional to the boundary layer thickness [3].

At Reynolds numbers around or less than 10^5, the flow on either side of the airfoil may be laminar up to the trailing edge. Acoustic emissions originate as a Kármán vortex street, a pattern of alternating vortices as shown in Figure 2.15b), emitted at the trailing edge. Sound emissions radiated upstream from the trailing edge can then contribute to the transition to turbulence or create boundary layer instabilities known as Tollmien-Schlichting waves which can then themselves radiate trailing edge noise resulting in a positive feedback loop [51]. Laminar boundary layer vortex shedding is tonal in nature, with the frequency of the sound source coinciding with the shedding frequency of the vortex street. Based on dimensional analysis the shedding frequency is proportional to velocity and inversely proportional to chord length. The laminar boundary layer vortex shedding mechanism is negligible for commercial turbines since they commonly operate at Reynolds numbers greater than 10^6, but can be significant for turbines on the order of a few kilowatts or less, with corresponding smaller chord lengths and relative velocities. The emissions produced by laminar boundary layer vortex shedding can be mitigated by tripping the boundary layer [49, 50].

At higher angles of attack, α, as shown for a two-dimensional airfoil in Figure 2.16, stall may occur resulting in flow separation on the suction side of the airfoil. For an operating turbine, the angle of attack for a two-dimensional segment of a three-dimensional turbine

blade is affected by the relative flow velocity resulting from freestream wind speed and rotational velocity component. By increasing the twist of the blade, or by increasing the freestream speed at a constant rotational rate, or by decreasing the rotational speed at a constant freestream speed, the angle of attack increases and the flow around the suction side of the airfoil separates near the trailing edge. Acoustic emissions are produced near the trailing edge due to the vorticity of the flow shed from the separation of the boundary layer. At stall, this noise mechanism can be increased by 10 dB [49].

An airfoil with a blunt trailing edge, such that the trailing edge thickness is 20% greater than the boundary layer displacement thickness, also creates a Kármán vortex street due to flow separation at the trailing edge [49]. Blunt trailing edge noise is a minor concern for a properly designed and fabricated turbine blade.

Other sources may arise in operation of a wind turbine, such as the aforementioned tip noise, deep stall, leading edge noise due to in-flow turbulence, or interactions with the flow passing between the blade and tower. However, experimental testing has shown that these sources are typically minor contributors to overall sound emissions in normal operating conditions [3, 40, 41]. Source maps produced from measurements of rotating turbines show common characteristics, which reveal the primary locations and probable mechanisms of sound productions. The greatest emissions are typically found at the outer portions of the blades, but not at the tip, and are noted to move outward with increasing acoustic frequency. The increase in radial position with increasing source frequency can be attributed to the decrease in airfoil chord length and increase in relative flow velocities with increasing radial position. For turbulent boundary layer trailing noise, the decrease in airfoil chord length and increase in flow velocity with an increase in radial position would result in thinner boundary layers and increase the frequency of turbulent boundary layer trailing edge noise. For laminar boundary layer vortex shedding the decrease in chord length and increase in flow velocity would increase the laminar boundary layer vortex shedding frequency at greater radial positions. In field testing of a Gamesa G58 wind turbine, Oerlemans et al. [3] discovered that the location of the greatest emissions ranged from a radial position located approximately 74% of the rotor diameter at 315 Hz to roughly 92% of the rotor diameter at 5 kHz. Wind tunnel tests of a 4.48 m two-bladed turbine performed by Oerlemans et al. [41] revealed a radially outward progression of the primary sound source from approximately 77% of rotor diameter at 1250 Hz to roughly 95% of the rotor diameter at 6.3 kHz. In testing a 1.2 m diameter, two-bladed, scale-model turbine, Cho et al. [40] presented similar findings, with the radial location of the measured sound source ranging from 77% at 2 kHz to 93% at 6.3 kHz.

2.4.2 Dipole Directivity and Convective Amplification

Distinguishing between trailing edge and leading edge noise is difficult based only on source maps due to the movement of the source and limitations encountered in spatial resolution.

A determination of the probable sound production mechanisms from an operating turbine requires an assessment of many contributing parameters. Knowledge of the propagation of a moving dipole source can aid in the assessment of wind turbine sound emissions.

Over a single revolution of a rotating wind turbine, the amplitudes of emissions emanating from a blade to an observer are not equal. At any given azimuth, the angular position of the blade, there can exist variations in the sound pressure level received at a stationary observer. Commonly for an observer located on the ground, the sound pressure level increases during a blade's downward approach. The variation in sound pressure level as a function of blade azimuth can be explained by the radiation pattern of trailing edge noise which is a dipole source, and by convective (Doppler) amplification due to the motion of the source. Referring to Figure 2.1 the magnitude of dipole source radiation is seen to vary with angle. Consequently, for an observer located on the ground a dipole source located at the trailing edge of a rotating turbine blade will be received across a wide range of emission angles as the dipole source moves along with the blade. Additionally, the motion of the blade contributes to a perceived increase in sound pressure level due to convective amplification as the motion vector of the source aligns with the vector from the dipole source to the observer. Based on an investigation of acoustic emissions from a commercial wind turbine, Oerlemans et al. [3] reported that the directivity function governing high frequency radiation from a trailing edge dipole source and convection of sound due to motion can be modelled by the following expression,

$$D = \frac{2sin^2\left(\theta/2\right) sin^2\phi}{\left(1 - Mcos\xi\right)^4} \tag{2.34}$$

where θ is the angle between the plane of the blade and the plane containing the chord line and observer, ϕ is the angle between the relative flow velocity at the blade and the plane containing the chord line and observer, ξ is the angle between the relative velocity vector and the line between source and observer, and M is the blade Mach number. This model was analytically developed for infinite flat plates [49] but has been shown to be valid for finite airfoils provided θ does not approach 180° and the airfoil chord is greater than the acoustic wavelengths [33]. Factors affecting the directivity of the dipole include the ratio of acoustic wavelength to the airfoil chord and convection of sound due to flow. For low frequency radiation where the acoustic wavelength is approximately the same wavelength as the chord length, the $sin^2\left(\theta/2\right)$ term should be replaced by $sin^2\theta$ [3]. For leading edge noise due to in-flow turbulence, θ should be replaced by $\pi - \theta$ as the θ dependence is inverted. In their study of the Gamesa G58 turbine, Oerlemans et al. included time-averaged measurements made using a 148-element microphone array which revealed sound emissions consistent with the analytical model described by Equation 2.34 [3]. The location of the greatest sound predicted by the directivity function was 110°, measured clockwise from the upward vertical position with an expected difference of 14.9 dB between maximum and minimum sound pressures over one revolution. Experimental source maps from these

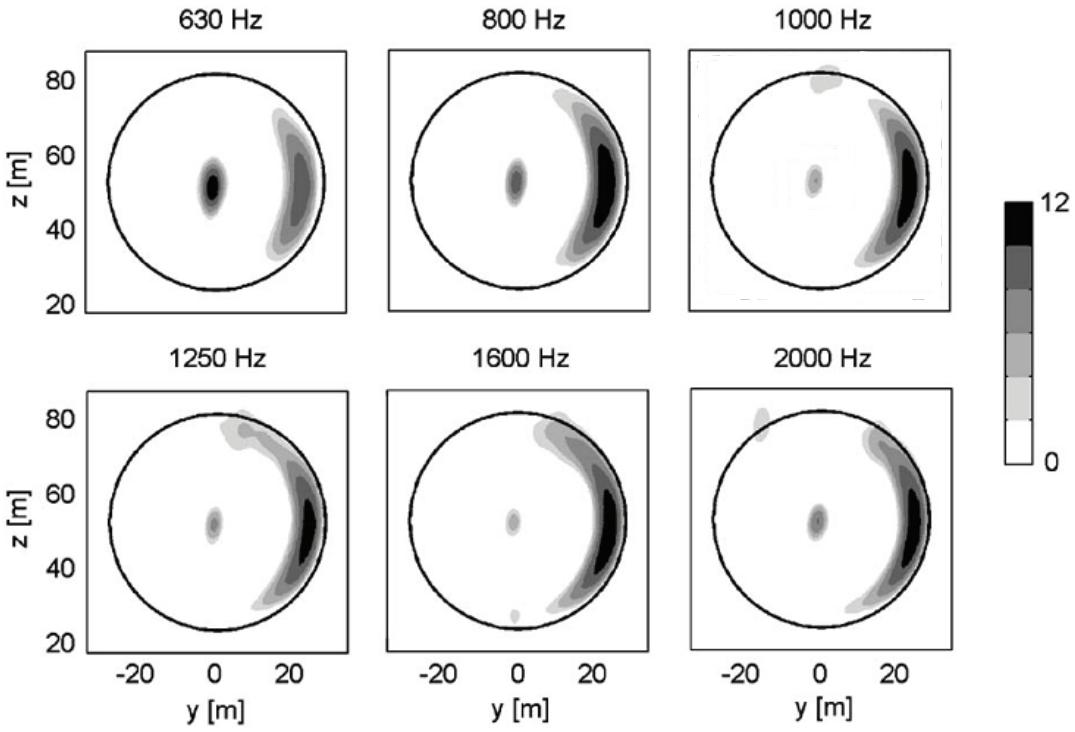

Figure 2.17: Experimental time-averaged source maps from field measurements of Gamesa G58 turbine (adapted from Oerlemans et al. [3])

tests are shown in Figure 2.17, where the circles represent the trajectory of the blade tips. The source maps reveal an average azimuth of 102° and a difference of approximately 15 dB between the right and left sides of the rotor plane, which was deemed consistent with the predicted locations of greatest sound emissions from the turbine rotor.

2.5 Wind Tunnel Testing

There are a number of configurations in which microphone arrays can be employed in wind tunnel installations. Microphone arrays have been used successfully in anechoic facilities, designed with aeroacoustic testing in mind. Due to their ability to increase the signal-to-noise ratio of sound measurements, they also have value in facilities designed explicitly for aerodynamic testing, where little regard has been given to the aeroacoustic measuring environment. Microphone arrays are becoming a common tool in aeroacoustics in both closed-loop and open-jet wind tunnels. However, careful consideration of the mounting configuration and facility are required for successful implementation of a microphone array.

2.5.1 Closed-Loop Wind Tunnels

Typically, installation of a microphone array in a closed-loop wind tunnel requires that the microphones be flush-mounted on a hard plane surface as shown in Figure 2.18, either along the test section wall or on a separate plate. Microphones located inside the tunnel test section are subjected to noise from various sources, including fans and flow. Having microphones located on a wall or plate inside a wind tunnel raises the noise floor of the microphones considerably as they are located in the boundary layer of the tunnel wall [4]. The beamforming process amplifies correlated sound signal over uncorrelated noise so it can be effective in reducing the boundary layer noise to some extent. However, this noise can be significant, and in many cases can overwhelm the target sound source. To overcome this noise, the boundary layer noise must be mitigated or the microphones must be taken out of the flow. Recessing the microphones by positioning them in holes behind the hard wall surface is not effective since the flow will still interact with the cylindrical holes, creating resonance and interfering with the natural decay of waves entering the holes. Trying to recess the entire microphone plate structure does not overcome the problem as the test section geometry must be modified, which would alter the flow and increase noise. A practical solution to removing the microphones from the flow requires that one of the tunnel walls remain ideally impermeable to flow and permeable to acoustic emissions, such that the microphones are able to receive sound from the test section, which constrains flow as though it is enclosed completely by hard walls. One such solution has been demonstrated using a taut Kevlar® sheet in place of a test section wall [29]. Microphones are placed behind the Kevlar® sheet, keeping them out of the flow and allowing sound emissions to pass through largely unaffected. However, boundary layer noise can still be an issue even when microphones are located outside the flow since this noise source is produced by all walls of the test section, notably between the target noise source and the microphones. This noise source will be correlated in the microphones and will be amplified by array processing, so measures must be taken to improve flow quality if this noise source presents a problem in measuring the target noise source. Reflections are also encountered in closed test sections, and these reflections will be detected as possible sources so they must be accounted for in processing or mitigated by acoustically treating the test section walls.

2.5.2 Open-Jet Wind Tunnels

Microphone measurements in open-jet facilities present the advantage of using the microphone array outside the flow without the need for modifications to the test section. Microphones can be placed in the flow if desired, but are most commonly located outside the flow to reduce boundary layer induced noise. An open-jet wind tunnel can be more readily converted to an anechoic facility, which can create an ideal measurement scenario for a microphone array. The improvements in open-jet tunnels are largely realized by removal of noise due to flow over microphones and walls, greater absorption by the environment,

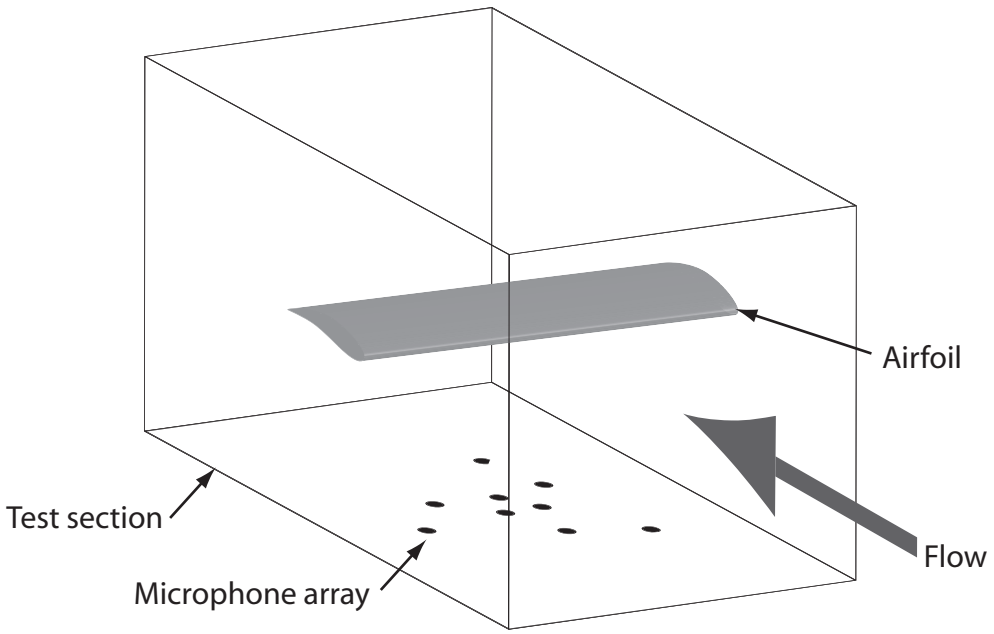

Figure 2.18: Diagram of microphone array testing in closed-loop wind tunnel

and lower fan-generated noise [4]. While the target sound source may demonstrate a lower recorded amplitude in the open-jet tunnel due to increased distance from the source, the decreased noise floor will still provide a greater signal-to-noise ratio over the closed-loop tunnel. However an open-jet tunnel does present an unbounded flow which may be difficult to utilize in controlled experiments. Furthermore, the presence of a shear layer between the microphone array and flow emitted from the open-jet tunnel can lead to erroneous source localization results due to refraction, as discussed in Section 2.2.4.

Chapter 3

Microphone Array Design and Fabrication

This chapter describes the work undertaken in the design and fabrication of two microphone arrays. A small-scale array (SSA) was first constructed for use in a closed-loop wind tunnel, followed by the large-scale array (LSA) which was designed and fabricated such that it could be used with a number of facilities. Implementing a microphone array for aeroacoustic measurements in wind tunnels presents numerous challenges such as cost, mounting considerations, spatial limitations, frequency range limitations, calibration, data acquisition, signal processing, data handling and storage. Efforts were undertaken to address these concerns. Details related to the microphone selection, array layout, printed circuit board design, and construction are included for each array. As implemented, beamforming is applied as a post-processing technique to previously recorded microphone data and is not performed in real-time. Both arrays are therefore standalone measurement devices which can be interfaced with any number of software algorithms.

3.1 Microphone Selection

Two types of microphones have primarily been used in microphone arrays: condenser and electret. Microphone arrays constructed with commercial condenser microphones can be prohibitively expensive for use in arrays with large numbers of sensors, and require the use of additional hardware to provide polarization voltages, signal conditioning, and preamplification. Furthermore, they can be difficult to install, particularly in wind tunnel applications where the microphones are commonly mounted onto a planar surface from the rear. A condenser microphone detects changes in capacitance due to pressure fluctuations imposed on a capacitor formed by a thin flexible diaphragm located in close proximity to a parallel, polarized backplate. These microphones have excellent performance and are provided with detailed calibration information. An option for an inexpensive microphone is

an electret capsule which operates similarly to a condenser microphone but does not require polarization as the backplate is prepolarized. These microphones are widely available, have minimal amplification, are fairly compact, and can offer similar acoustic performance to condenser microphones. Unavoidably, these microphone capsules require additional signal conditioning and preamplification which can lead to mounting costs or considerable effort in amplifier design, layout, and assembly.

More recently, microelectromechanical (MEMS) microphones have shown promise as an alternative in microphone arrays for aeroacoustic testing [52–54]. A MEMS microphone is a silicon device consisting of a small diaphragm combined with built-in circuitry including CMOS preamplification and filtering. Sound is transmitted to the diaphragm through a narrow acoustic port in the microphone casing. These microphone packages are surface mount devices, and as such are extremely compact. Surface mount devices can lead to difficulties in assembly but offer excellent positional accuracy which is of utmost importance for successful beamforming processing. Furthermore, the built-in circuitry allows for the microphones to be implemented in a system with few additional components. The prospect of using a miniature, inexpensive, and relatively easy to implement package was tempting for use in research. There are a wide range of MEMS microphones available through common electronics distributors. Knowles Acoustics SiSonic MEMS microphones were chosen due to the large number of products offered by the company, the ease of obtaining the units through electronics distributors, and their previous successful implementation in a microphone array [53].

Small-Scale Array:

Presented with a wide range of microphone options in the Knowles SiSonic product line, the SPM0408LE5H microphone was selected for the small-scale array [55]. This silicon microphone is shown in detail in Figure 3.1. It was deemed the most suitable offering for small-scale array as it is a bottom-ported microphone with analog preamplification circuitry allowing up to 20 dB gain. Furthermore the microphone includes enhanced radio frequency (RF) protection and is housed in a "Mini" package with dimensions 4.72 mm by 3.76 mm by 1.25 mm, allowing for a compact layout. The microphone uses a perforated backplate, and has an acoustic port 0.254 mm in diameter. This microphone has the flattest published frequency response among the SiSonic packages, as shown in Figure 3.2.

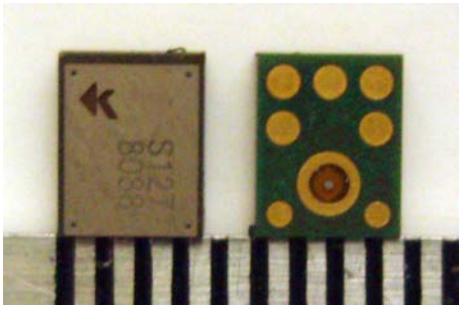

Figure 3.1: Detail view of SPM0408LE5H microphone top and bottom (ruler scale in mm)

The microphone's flatter frequency response compared to other similarly packaged microphones is largely due to the internal geometry of the casing. A common trait of all Knowles MEMS microphones is the use of a ported design with an acoustic cavity transmitting pressure fluctuations to the diaphragm. Bottom-ported microphones produced by Knowles have a small, direct acoustic cavity within the microphone package itself with a relatively large back volume compared to the diaphragm. This geometry can be seen in Figure 3.3.

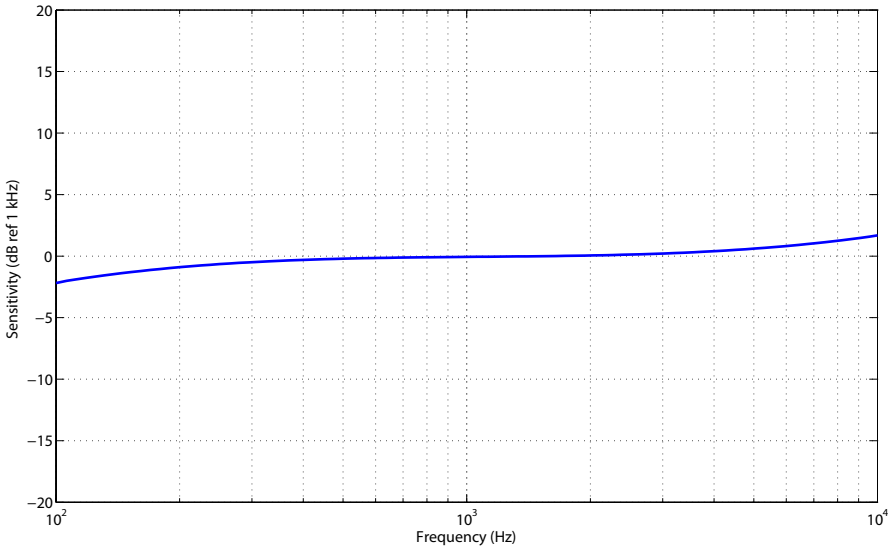

Figure 3.2: Published SPM0408LE5H frequency response (data from Knowles Acoustics [56])

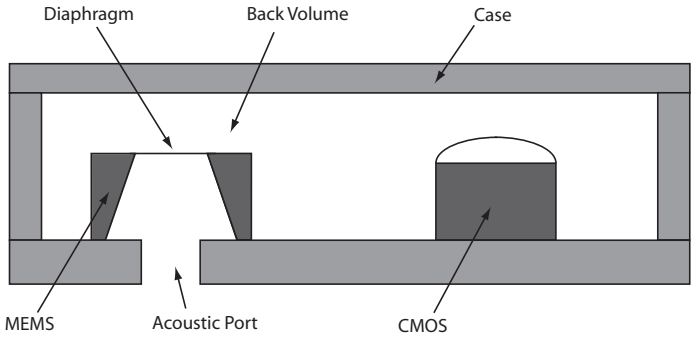

Figure 3.3: Simplified bottom-ported microphone (adapted from Knowles Acoustics [57])

The bottom-ported package requires that the microphone be soldered to a printed circuit board (PCB) and that the PCB have a port hole to serve as an acoustic path. The microphone has 8 surface mount pads, including an annular ring surrounding the microphone port which acts as an acoustic seal when soldered. The built-in amplification and filtering significantly reduce the number of additional components required in the circuit design, and reduce the risk of component failure during fabrication. The preamplifier has adjustable gain yielding sensitivities of -38 dB to -18 dB, and provides the ability to set the high pass cutoff frequency through the selection of a single capacitor. The MEMS packages require power to provide the required voltage for the amplifier. The microphones are rated for 1.5 to 3.6V and have no change in sensitivity in this range. The total harmonic distortion (THD) of the microphone output is rated as less than 1% at 100 dB and less than 10% at 115 dB.

Large-Scale Array:

For the large-scale array, a similar microphone was selected: a Knowles Acoustics SPM0408HE5H microphone. This microphone has the same electronic circuitry as the SPM0408LE5H microphone but is contained in a top-ported package with 4 surface mount pads, as shown in Figure 3.4.

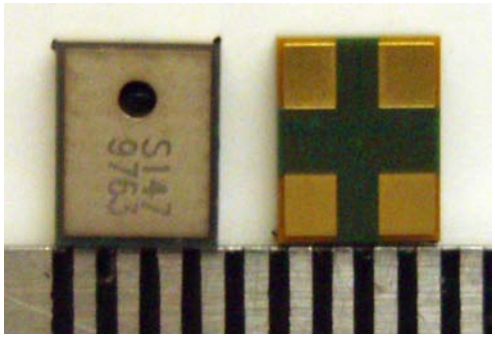

Figure 3.4: Detail view of SPM0408HE5H microphone top and bottom (ruler scale in mm)

The acoustic port, measuring 0.838 mm in diameter, is located in the microphone casing on the top surface of the microphone, so the microphone does not require an acoustic pathway through the PCB. Therefore the microphone presents fewer concerns related to soldering and sealing of the acoustic pathway. The published frequency response is similar to the SPM0408LE5H used in the small-scale array, albeit slightly less flat as shown in Figure 3.5. The top-ported microphones available from Knowles utilize an acoustic port hole in the top of the package casing. The acoustic pathway within the casing is relatively lengthy since the port hole and diaphragm are at opposite ends of the package. Furthermore, the back volume behind the diaphragm is considerably smaller than in the bottom-ported configuration. A simplified diagram of the internal geometry of the top-ported microphone is shown in Figure 3.6.

Since both microphone types use a narrow acoustic port, a strong resonant peak is expected in the upper range of the frequency response of the microphone. This strong frequency amplification is due to Helmholtz resonance, wherein a narrow opening with a much larger volume of air connected to it creates a resonant peak, as the volume of air in the microphone oscillates in and out of the port hole, like a mass-spring system [6]. Helmholtz resonance is known to occur in these MEMS microphones around or above 10 kHz [57]. This resonance can be mitigated in a number of ways, primarily by altering the geometry of the acoustic port. In most cases improvements are made to simply force the resonance to a higher frequency. In the case of the SPM0408LE5H bottom-ported microphone, the frequency response can be flattened by using a wider, shorter pathway in the PCB. The acoustic path within the microphone is as short and direct as possible. Another method of improving frequency response is to use a thin permeable material, known as an acoustic vent, over the port hole to create an acoustic resistance. For the SPM0408HE5H top-ported microphone, the port hole cannot be readily changed without altering the microphone's plastic casing. An acoustic vent could also be used over the SPM0408HE5H port hole to introduce some acoustic resistance to dampen the spring effect of the air volume in the cavity. The acoustic pathway within the microphone casing could be minimized by rotating the case 180 degrees or by removing it entirely.

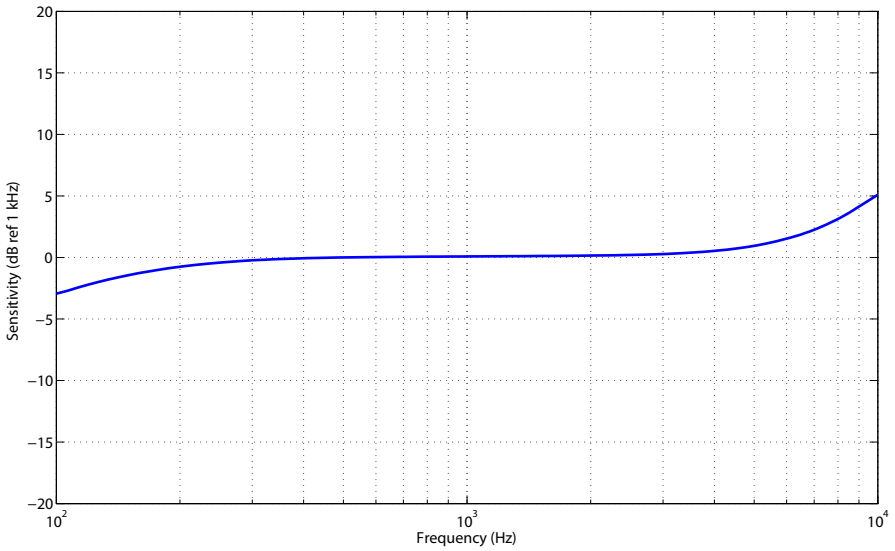

Figure 3.5: Published SPM0408HE5H frequency response (data from Knowles Acoustics [58])

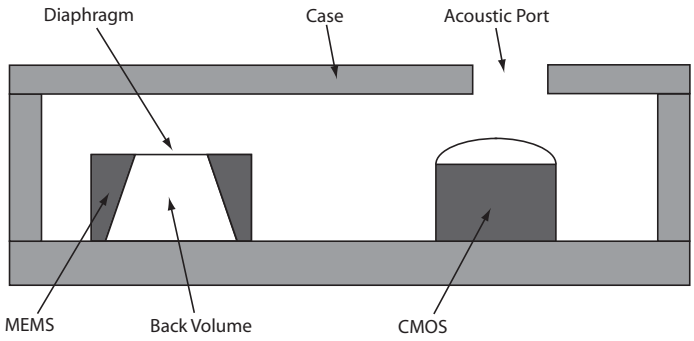

Figure 3.6: Simplified top-ported microphone (adapted from Knowles Acoustics [57])

3.2 Array Layout

Small-Scale Array:

The main constraints for the small-scale array were the sensor count, as the data acquisition hardware has a maximum channel count of 32, and the physical size of the PCB, since the small-scale array was designed to be used in a wind tunnel with a 152.4 mm square test section. Potential array layouts were tested using a simulated source, having a modelled microphone signal amplitude and time delay based on propagation distance, located along the z-axis and evaluated with numerous combinations of parameters and layout types including a random array, circular array, and numerous spiral geometries. Efforts were made to employ an odd number of elements in each arm to eliminate redundancy in intersensor vectors and provide a variety of intersensor spacings [9]. The small-scale array was found to give the best performance in terms of beamwidth and sidelobe suppression, while also maintaining a concise, organized layout when an array of 27 sensors arranged in an Underbrink equal-aperture configuration was used [9].

The layout has nine logarithmic spiral arms arranged in three concentric rings. The inner radius of the array is 13 mm and the outer radius is 70.5 mm. The spiral angle is 70°. The array aperture is 141 mm and the minimum intersensor spacing is 8.9 mm. A representation of the array layout is shown in Figure 3.7 and a list of microphone coordinates can be found in Appendix A.

Large-Scale Array:

The large-scale array is also an Underbrink equal-aperture design, made up of 30 microphones. The array contains five spiral arms with six concentric rings. Again, it was essential to use an odd number of sensors in each arm to reduce sidelobes due to intersensor spacing redundancy. The inner radius is 35 mm and the outer radius is 470 mm. The spiral angle is 68°. The minimum intersensor spacing is 41.1 mm and the array aperture is 940 mm. The array geometry was also selected primarily using simulated data of a single source located along the z-axis to evaluate the effect of various parameters on the array performance. The chosen geometry provided the best performance of any configuration tested. The array geometry is shown in Figure 3.8 and the microphone coordinates referenced to the array centre can be found in Appendix A.

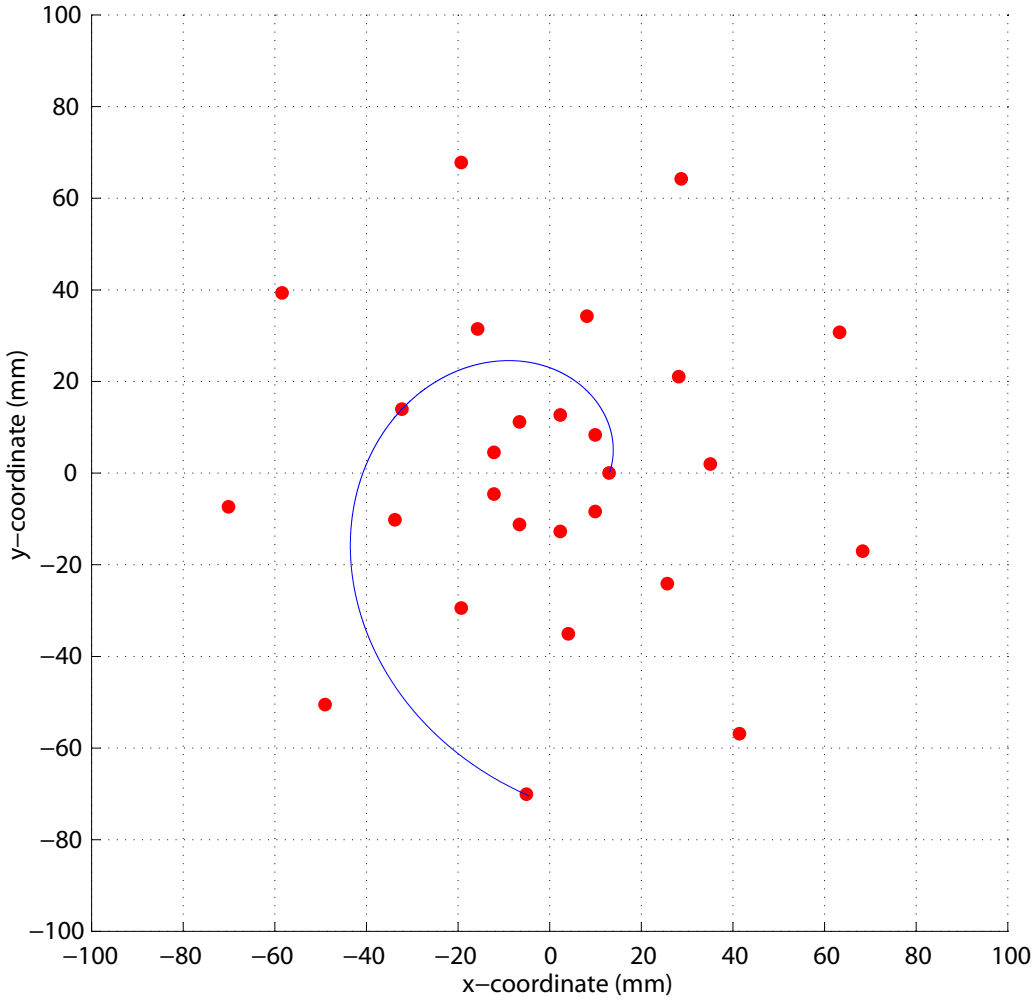

Figure 3.7: Small-scale array layout (viewed from rear)

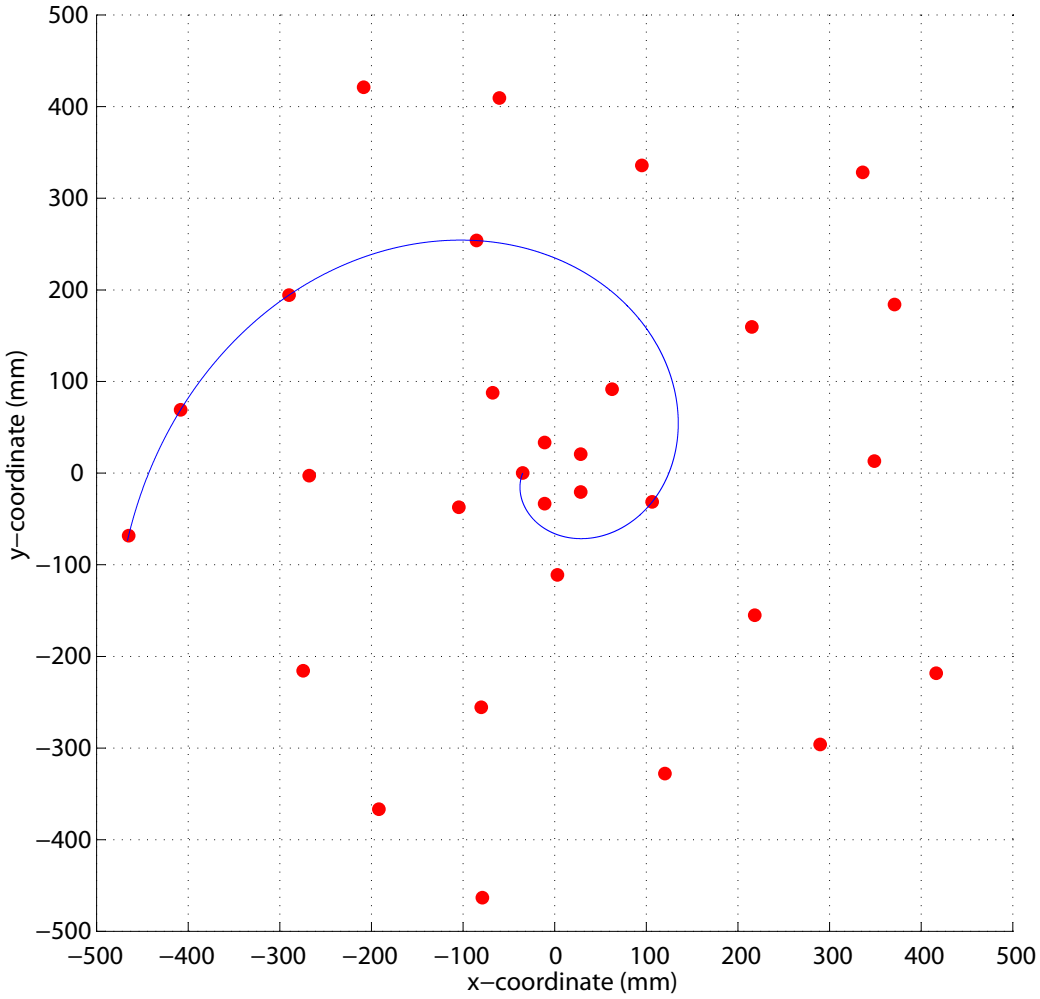

Figure 3.8: Large-scale array layout (viewed from rear)

3.3 Printed Circuit Board Design

The use of a MEMS surface mount device necessitated the use of unique mounting structures. The small-scale array was designed to be incorporated onto a single printed circuit board that would provide the required electrical connections between all microphones and serve as the structural frame. The large-scale array also used printed circuit boards for electrical connections, although individual PCBs were used for each microphone to provide a modular microphone package which could be attached to any accommodating structure.

Small-Scale Array:

The small-scale array is constructed on a standard 1.5 mm thick FR4 PCB, with dimensions 152.4 mm by 203.2 mm, which also provides the structural frame of the microphone array. The layout was completed using FreePCB software [59]. The small-scale array contains 27 microphones. Each microphone requires an additional four passive components, while globally the circuit also includes additional parts such as power supply filtering capacitors and connectors for signals and power distribution. Electrical component selection was based on the formulae and guidelines provided in the microphone specifications [56]. The gain of the amplifier was set to the maximum 20 dB yielding a nominal sensitivity of -18 dB and the high-pass corner frequency was set to 141 Hz. An abbreviated schematic for the 27 microphone design is shown in Figure 3.9. Jumpers in the form of zero ohm resistors were included to allow for gain adjustment.

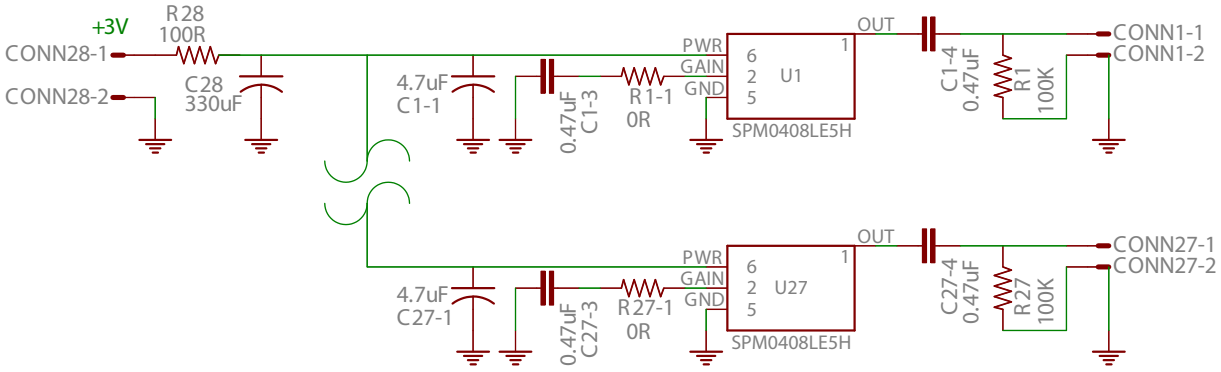

Figure 3.9: Small-scale array partial schematic

A two-layer PCB was used with the lower layer reserved for the ground plane and the upper layer for all power and signal traces, with ground traces inserted between all others to minimize cross-talk. The use of plated drill holes in the PCB for the acoustic pathways enabled the ground plane side of the board to be completely smooth, allowing the PCB to be used directly in the measuring environment. Gerber and drill files for the board layout were created using the FreePCB software, and these files were sent to Alberta Printed

Circuits for PCB fabrication [60]. The PCBs were returned for component population using surface mount components. The printed circuit board design is shown in Figure 3.10.

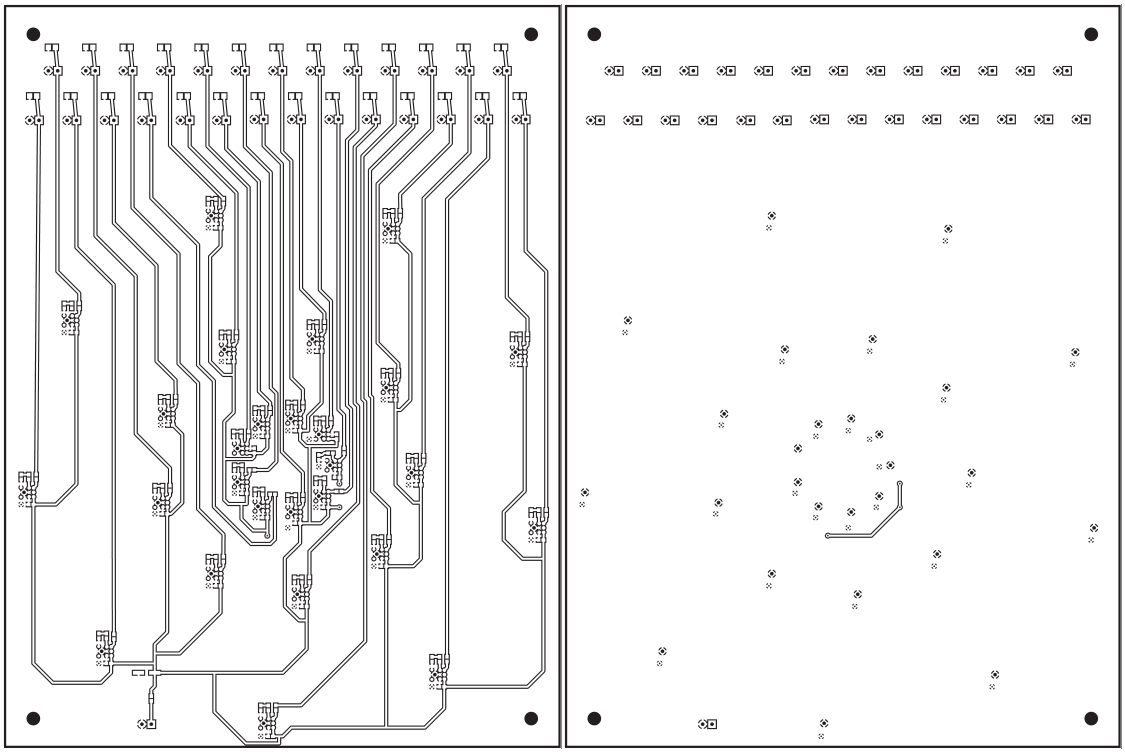

Figure 3.10: Small-scale array PCB component and ground planes (not to scale)

Large-Scale Array:

The large-scale array contains 30 microphones, each mounted to its own PCB with dimensions 38.1 mm by 25.4 mm. The use of individual PCBs allows each microphone to be modular and used in any array configuration. Two-layer PCBs were used with the microphone on one layer with the ground plane and all other components on the other layer. The component layer of each PCB contains two connectors, and passive surface mount components consisting of three resistors and four capacitors for power supply filtering, AC coupling, and gain and filter settings. The schematic for each microphone is shown in Figure 3.11.

The PCB layout is shown in Figure 3.12. The amplifier gain was set to 10 dB and the corner frequency was set to 120 Hz. Since each microphone is located on an individual PCB, a structural frame was required for mounting the microphones in their intended positions.

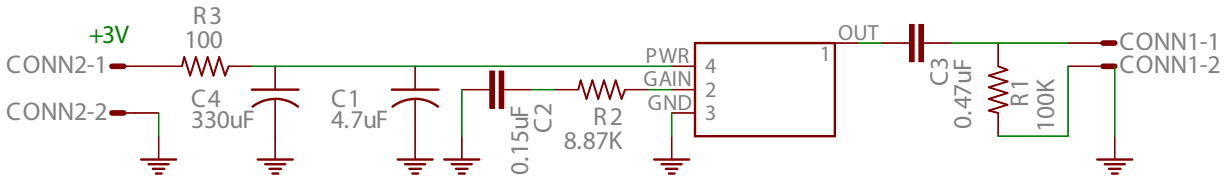

Figure 3.11: Large-scale array individual PCB schematic

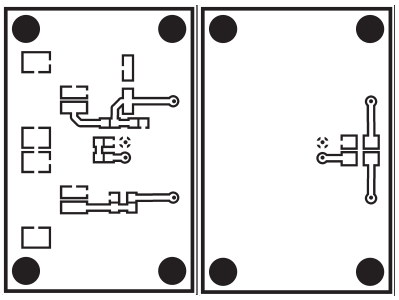

Figure 3.12: Large-scale array PCB design for component and microphone/ground planes (drawn to scale)

3.4 Physical Construction Methods

The use of surface mount microphones necessitated the use of a custom reflow oven for mounting the components to the printed circuit boards. The oven is shown in Figure 3.13 shortly after population of the small-scale array.

The custom reflow oven was utilized throughout fabrication of both microphone arrays. A LabVIEW control system, found in Appendix A, was programmed and implemented to provide the desired reflow profile as specified by the microphone manufacturer. A thermocouple located in the oven provided feedback to the control system through a National Instruments PCI-6251 data acquisition card (DAQ). The oven temperature was monitored through the thermocouple and a normally open (NO) relay was controlled by a 5 volt DC voltage from the DAQ analog output. The DAQ and relay were electrically isolated through a photocoupler to eliminate the possibility of high voltage entering the DAQ. A schematic of the relay configuration is shown in Figure 3.14.

When the thermocouple temperature was below the desired oven temperature, 5 volts DC would be applied from the DAQ to the relay coil, causing the relay to close, and providing the oven with mains power. The oven temperature would then increase until the thermocouple temperature reached the desired oven temperature, at which point the 5 VDC control voltage would be removed from the relay coil and the relay would open, causing the oven to lose its mains connection and cool down. This control system experi-

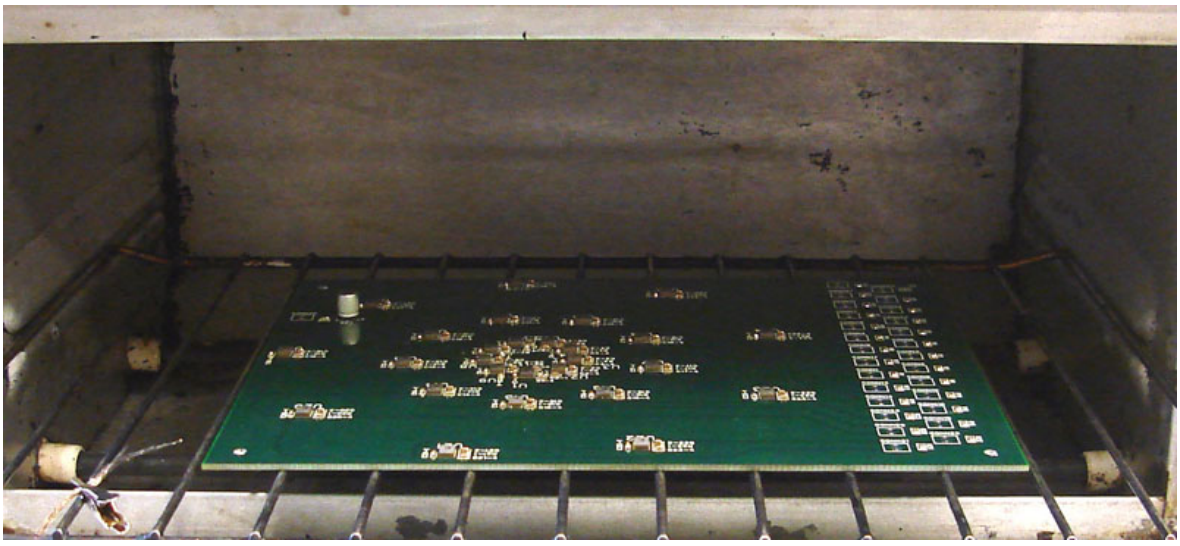

Figure 3.13: Custom reflow oven following small-scale array component population

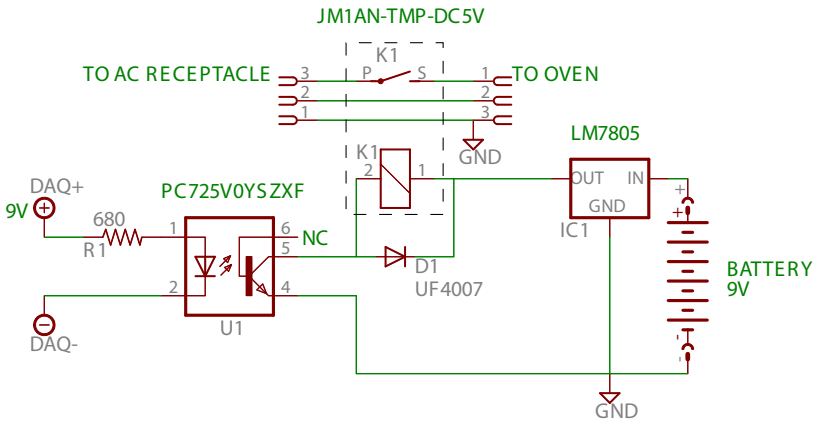

Figure 3.14: Relay controller schematic

enced temperature overshoot of a few degrees but maintained a reflow profile within the manufacturer's specified temperature limits. To avoid damaging of the solder material and the finished solder joint it was desired to keep the heating rate of the oven below 3 °C/s and the cooling rate between 2 and 4 °C/s [61,62]. The average heating rate of the system during the preheat stage was 1.9 °C/s and 1.3 °C/s during the solder melt stage. Following the reflow cycle, cooling was achieved by opening the oven door, varying the opening to match an approximate 2-4 °C/s cooling rate. The recommended reflow profile and a typical reflow profile using the custom reflow oven are shown in Figure 3.15.

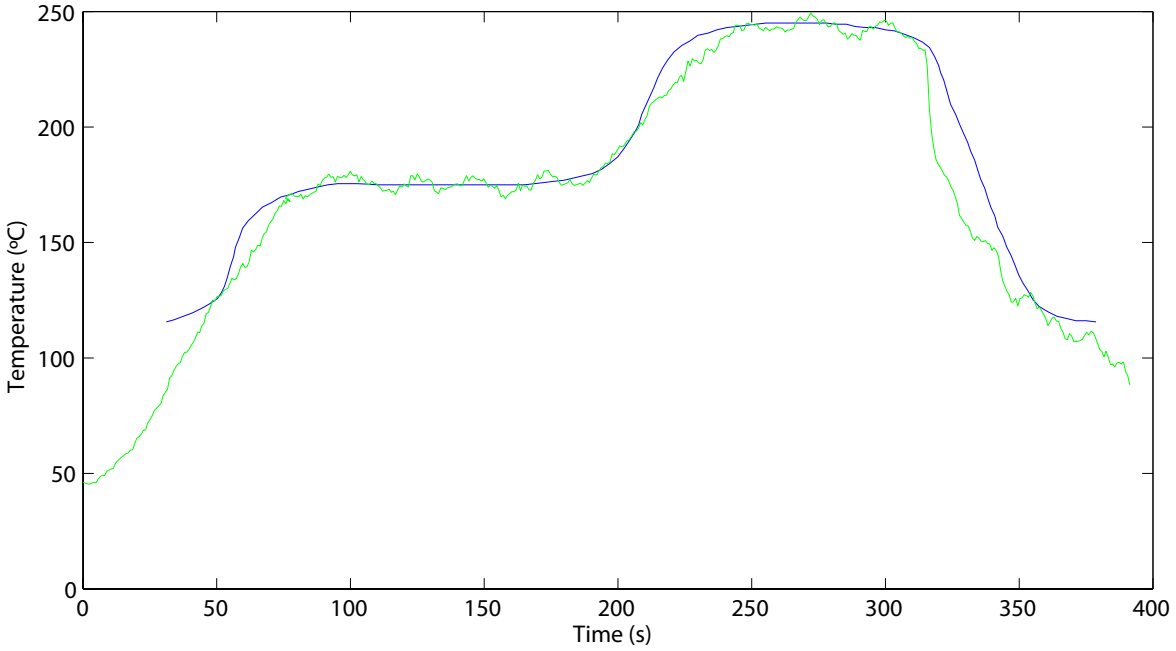

Figure 3.15: Recommended and typical solder reflow profiles — Recommended profile — Actual profile (data from Knowles Acoustics [56, 58])

Small-Scale Array:

The component layer required soldering of 27 microphones and their associated components, each requiring three capacitors and two resistors. The components were soldered to the PCB using Chip Quik SMD4300AX10 solder paste with 57% tin, 43% lead composition [63]. All components except connectors were soldered simultaneously with this method. Connectors were hand-soldered just prior to completing the array. The use of a single PCB for the small-scale array presented a number of challenges in fabrication as all microphones were subjected to the reflow process simultaneously. Due to the bottom-mounted solder pads, once soldered the circuit's microphone functionality could not be

easily verified through continuity testing and had to therefore be verified by acoustic testing. The acoustic testing consisted of analyzing each microphone's time domain signal and power spectrum for occurrences such as DC offset, extraneous noise, or an inconsistent frequency response. When a microphone was found to have any of these problems, it would require another reflow cycle to improve contact between solder pads and lands or to improve the acoustic seal provided by the annular ring surrounding the microphone port. According to the Knowles product literature, each microphone should be limited to a maximum of 3 reflows. Therefore it was necessary for problematic microphones to be replaced individually rather than subjecting the entire array to another reflow cycle to minimize damage to the working MEMS microphones. Individual microphone replacement required rework through the use of a heat gun localized around the non-working microphone. The heat gun process was successful, but offered little repeatability. The completed array is shown in Figure 3.16.

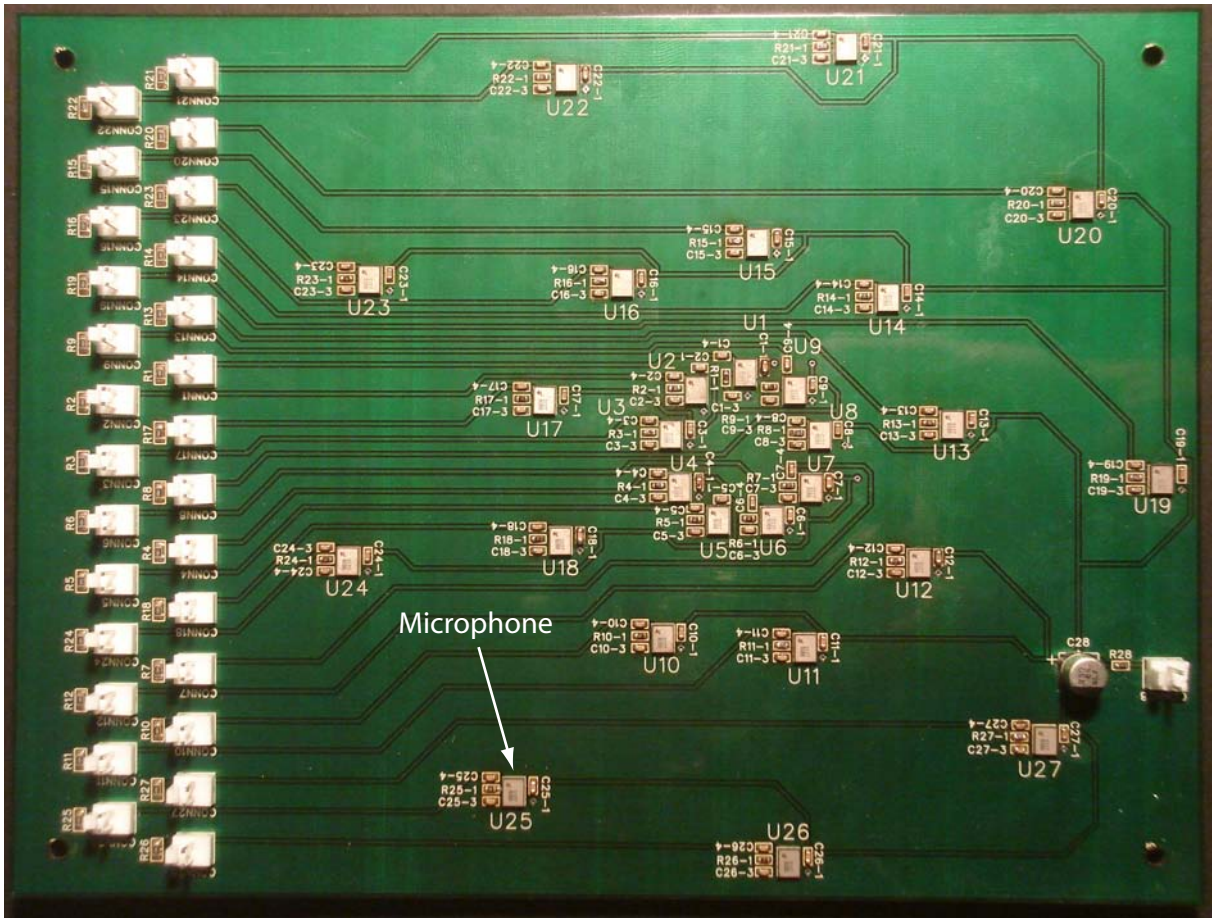

Figure 3.16: Detail view of small-scale array

Large-Scale Array:

The construction of the large-scale array offered fewer challenges due to the use of individual PCBS and top-ported MEMS microphones. The PCBs were constructed in a similar fashion, using solder paste and the custom reflow oven. Reflow was done with ten microphone PCBs per process. The use of a separate PCB for each microphone enabled convenient microphone replacement, and since the four large solder pads on the SPM0408HE5H microphones were easily soldered compared to the eight small pads and annular ring of the SPM0408LE5H microphone used in the small-scale array, microphone replacement due to fabrication error was never necessary. Microphones were placed on one side of the PCB, surrounded by a ground plane, while all other components were placed on the other side. Using different layers for microphone and all other components required that the components be soldered in one reflow process while the microphones be added during a second reflow stage. A completed microphone PCB used in the large-scale array is shown in Figure 3.17.

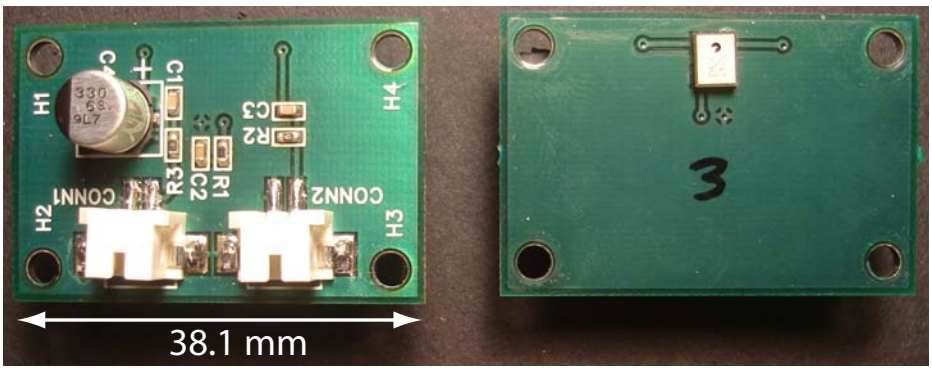

Figure 3.17: Detail view of fabricated microphone PCB used in the large-scale array

An important consideration for both arrays was confidence that the microphone placement matched the intended array layout to minimize errors in the beamforming process due to differences in physical and theoretical intersensor spacings. While the single PCB construction used in the small-scale array allowed the microphones to be precisely located within approximately 0.1 mm, the individual microphone PCBs used in the large-scale array required further efforts to ensure the microphones were placed at their intended locations. A 14-gauge (1.63 mm thick) aluminum sheet with dimensions 1 m by 1 m was used for securing the PCBs to the array. To ensure precision in the fabricated array geometry, the microphone mounting holes in the sheet were lasercut. The microphones were inserted from the rear through holes in the sheet as demonstrated in Figure 3.18.

Having a height of 1.25 mm in addition to the height provided by the presence of the solder connections, the tops of the microphones were nearly coincident with the upper surface of the aluminum sheet. The aluminum sheet was secured to a square frame made

Figure 3.18: Detail view of microphone PCBs from the rear of the array

of 25.4 mm square aluminum tubing. The welded frame was designed to stand upright in a number of configurations. In its vertical position the bottom of the array is 30 cm above ground to reduce the influence of reflections from the floor by increasing the reflected distance. The assembled array is shown in Figure 3.19.

Connectors:

The inputs to the DAQ used in data collection, described in Chapter 5, use RJ50 connectors. While the DAQ typically utilizes each of the eight contacts of the RJ50 connector, in the experimental setup employed only two are required for the microphone signal and ground. To interface with the required RJ50 connector, multi-conductor shielded Belden wire was used to connect the microphone PCBs to the DAQ. Contacts were manually crimped onto the wires and inserted into connector housings. The cable shield was also crimped at one end of the cable, at the PCB connector to reduce electromagnetic interference without creating a ground loop which could increase the electrical noise floor of the system. Heat shrink was used over the end of the cable and connector to improve the durability of the cable assembly. Two-pin connectors were used on the PCBs: through-hole connectors for the small-scale array and surface mount connectors for the large-scale array. A total of 28 cables, 27 for audio signals and one for power, were required for the small-scale array. The large-scale array utilized a terminal block for power and ground distribution and therefore required 61 cables: 30 for audio signals and 31 for power distribution connecting the power supply, terminal block, and microphones. The cable ends and connector details are shown in Figure 3.20.

Figure 3.19: Front view of completed large-scale array

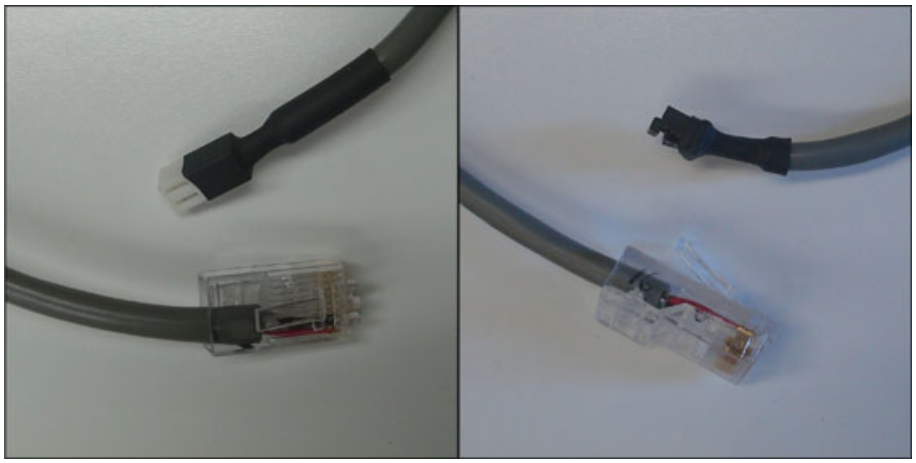

Figure 3.20: Detail views of connectors used in small-scale array (left) and large-scale array (right)

Chapter 4

Microphone Calibration

In order for a microphone array to work effectively, the response of each microphone must be known. It was therefore necessary to develop a methodology for characterizing the performance of the two microphone types. The chosen technique and numerous unsuccessful methods are presented below.

4.1 Calibration Techniques Considered

A number of methods were considered for calibrating the MEMS microphones used in both arrays including free-field, acoustic coupler, electrostatic actuator, and pistonphone. Of these methods, using an acoustic coupler, electrostatic actuator, and pistonphone provide the microphone's pressure sensitivity, while the free-field calibration provides the free-field sensitivity. The free-field sensitivity differs from the pressure sensitivity due to diffraction around the microphone. In the free-field the incident sound wave diffracts around the microphone and creates a varying sound field over the diaphragm. When the microphone diaphragm is placed in an environment where the incoming sound field is uniform, such as when installed coincident to a flat plate or in a small enclosed environment, the sound wave is uniform across the diaphragm and the resultant measurement is the pressure sensitivity [64].

Free-Field:

Free-field microphone calibration is typically performed inside an anechoic chamber. The use of an anechoic chamber provides an environment in which source field measurements are not disturbed by ambient sound levels and in which the energy of the sound source is absorbed by the chamber walls, eliminating reflections and representing the free-field environment [6]. Anechoic chambers that are capable of being used effectively across a wide frequency range are extremely large and expensive. Calibration in an anechoic chamber can be performed using sound source excitation via a sine wave or noise band [65].

Calibration can be performed using one of three methods [66]:

- Simultaneous
- Substitution
- Reciprocity

Simultaneous calibration requires that measurements be made of a sound source by a reference microphone and uncalibrated microphone at the same time. The microphones cannot simultaneously occupy the same physical space so the sound source must be spatially uniform, which can be difficult and costly to achieve in the free-field.

Substitution involves calibrating a reference microphone to a sound source at a known location. The reference microphone is then removed and replaced with an uncalibrated microphone at the same location. This eliminates any problems arising from directionality or spatial non-uniformity of the sound field but requires that the sound source be temporally stable since microphone measurements are not made simultaneously.

Calibration by reciprocity requires three transducers, two of which must have known responses. The technique requires that two of the transducers be capable of operating in reverse as a sound source in addition to receiver, while the third operates strictly as a transmitter. Throughout testing the three microphones are each cycled as source and receiver with two microphones facing each other directly. The transfer functions between the three microphone pairs can be solved simultaneously leading to a highly accurate calibration. The system has a number of drawbacks such as the requirement that the microphones must operate efficiently as both transmitter and receiver, and the considerable time required for calibration of each unknown sensor [64, 65].

For any of the above free-field methods, it is important to use the same microphones or create fittings which have the same geometry to eliminate differences due to the sound waves diffracting around the microphone body.

Coupler:

Calibration using a coupler, such as a plane wave tube, can also be used to provide the pressure response of an uncalibrated microphone using the three methods above. A plane wave tube is a rigid duct which couples to an acoustic source at one end and to one or more microphones at some distance along its length. It is used to propagate plane waves along its length to provide a frequency invariant load such that two devices located at the same axial position are subjected to the same field [6, 67]. There are two types of plane wave tube couplers: normal incidence and grazing incidence. A normal incidence tube places the microphones at the end of the coupler, such that the microphone and sound source face each other. A grazing incidence tube places the microphones at some distance along the tube perpendicular to the coupler. Both methods have been used successfully but grazing incidence can be less reliable over a wide frequency range [68]. Again, source excitation

can be provided by a sine wave or broadband noise. The issue of diffraction experienced by different geometries in the free-field is eliminated through the use of a coupler since the microphone bodies are mounted coincident with the coupler wall.

In the simultaneous calibration method, a plane wave tube coupler overcomes the spatial uniformity issue, since two microphones can easily be placed at the same axial position in the plane wave tube and therefore be exposed to the same sound field. The drawbacks of reciprocity calibration are still present however. The same advantages and disadvantages exist in substitution for the coupler as in the free-field. A drawback of the coupler method is that the measured response is for the pressure sensitivity and may differ from the free-field sensitivity.

A major obstacle in the use of a coupler such as a plane wave tube is that it has limited effectiveness over a wide frequency range due to its geometry. The zero-order mode propagates plane waves at any frequency, but for higher order modes, the waves no longer propagate strictly along the length of the tube. For a tube with circular cross-section, the high-frequency cutoff for data to be considered reliable is calculated by

$$f_H = \frac{0.383c}{d} \tag{4.1}$$

where d is the plane wave tube diameter [69]. The low-frequency cutoff for reliable data is taken as,

$$f_L = \frac{c}{4l} \tag{4.2}$$

where l is the length of the plane wave tube [67].

Electrostatic Actuator:

An electrostatic actuator is a commercial calibrator consisting of a metal grid polarized with direct current at high voltage. Electrostatic pressure is superimposed onto the microphone from the electrostatic actuator in the form of a variable AC voltage [66]. This method is commonly used to provide frequency responses well above the audible range and is commonly used to calibrate condenser microphones. The response is typically comparable to a pressure response obtained in a coupler over a fairly wide frequency range. Advantages of this method are that electrostatic actuators are fairly inexpensive and do not take a significant amount of time to perform a calibration. Furthermore, they are independent of environmental conditions such as air temperature and humidity. However, electrostatic actuators must be used with specified models of microphones since the microphone requires an exposed and conducting diaphragm.

Pistonphone:

A pistonphone is another commercially available product which can be used to obtain the pressure sensitivity of a microphone. It operates on a principle similar to that of a

coupling tube. A closed volume of air is driven by a piston at a specific frequency to create a known pressure in the air chamber. Pistonphones can only be used for specific frequencies, commonly 250 Hz or 1 kHz and at specific sound pressure levels [66, 70].

4.1.1 Preliminary Calibration Attempts

Although a small anechoic chamber was available for free-field calibration, its performance was found unsatisfactory for sensor calibration [71]. Another suitable anechoic chamber was not available at the time of calibration. Furthermore, because the microphones in both the small-scale and large-scale arrays were mounted coincident to a hard planar surface, pressure sensitivity provided a suitable characterization of the microphones. Since testing in an anechoic chamber yields a free-field sensitivity, while the other three methods mentioned above are used for pressure sensitivity, these methods were favoured. The use of an electrostatic actuator was determined to not be feasible as commercially available units are intended to be used with specific microphones and could not be adapted to the compact packaging of the MEMS microphones employed in both arrays. Additionally, these microphones have shown themselves to be unsuitable candidates for electrostatic actuation due to their diaphragm size [64]. Similarly, a commercial pistonphone could not be put to use due to the microphone packaging. More importantly, the specified number of frequencies and sound pressure levels available in a pistonphone would have limited the usefulness of the calibration. Calibration involving a coupler was selected as it generates a pressure response, allows for adaptation to various microphone packages through the use of fittings, and can perform over a range of frequencies.

The geometry of the small-scale array presented a number of challenges for microphone calibration. In order to function, the microphones had to be soldered to a printed circuit board. The microphones were difficult to unsolder without damaging, and therefore had to be calibrated while installed in the array. For simultaneous calibration of the microphones in the small-scale array, the coupler calibration method required that the MEMS microphone and reference microphone be located at different planes, since the reference microphone could not occupy the space immediately adjacent to the MEMS microphone due to the PCB structure. A number of coupler geometries were implemented based on literature involving flush mounted transducers. Efforts were made to perform a simultaneous calibration of a MEMS microphone along with a reference microphone, using a small speaker as a sound generator, coupled through a network of channels in a T-configuration in an enclosed aluminum block. The interface between the MEMS microphone PCB and calibrator was sealed by an O-ring and the reference microphone was sealed with a Teflon insert. A speaker provided the calibration sound source and was monitored by the reference and uncalibrated MEMS microphones. This setup was similar to that employed by NASA for calibrating recessed transducers and allowed for in-situ testing of the microphones in the small-scale array [72]. All internal geometry including channel diameter and distance from

centreline to receiver, was equal for both the MEMS microphone and reference microphone. However, the frequency response obtained in testing the MEMS microphone exhibited resonant peaks which could only be explained by the geometry of the coupling tube. This coupler was refined further and a second design was used for simultaneous calibration. The second coupling tube operated on a similar principle but positioned the two microphones facing each other along the same axis, perpendicular to the sound source. Again an O-ring was used to seal the coupler to the microphone PCB and a Teflon sleeve provided sealing between the reference microphone and the tube. Similar resonant peaks were encountered using this second coupler. As a result of the unexpected frequency response results and the difficulties encountered in testing, simultaneous calibration was ruled out as a possible calibration method for the microphones in the small-scale array. Reciprocity could not be employed due to the lack of suitable reference microphones which could act as transmitters as well as receivers. Further calibration was performed primarily using a normal incidence plane wave tube and a combination of simultaneous and substitution methods as described below.

4.2 Calibration Overview

Microphones were first calibrated with respect to amplitude response to determine the maximum sound pressure level at which they could provide a linear sensitivity. Frequency response was also tested to compare the published frequency response to the measured response. Due to difficulties experienced in the frequency response tests of microphones installed in the small-scale array, covered in detail in Section 4.1.1, it was decided that a single point sensitivity test at 1 kHz was required for each microphone to provide the most useful calibration between microphones. Furthermore, difficulties in the calibration method did not allow for microphone phase to be tested which is discussed in detail in Section 4.2.4.

Much of the calibration was performed using a LabVIEW control system and a National Instruments PCI-6251 16-bit data acquisition card which supplied an analog voltage signal to a B&C DE10 25.4 mm compression driver amplified through a National Semiconductor LM1875 power amplifier circuit. The compression driver was coupled to a plane wave tube located in a small anechoic chamber. Details of the control system, amplifier, and anechoic chamber can be found in McPhee [71]. The microphone sensor was calibrated simultaneously alongside a B&K 4192 reference microphone amplified and conditioned by a B&K 2669-C preamplifier and a B&K 2690-A-0S1 conditioning amplifier. Power to each microphone circuit was provided by an Agilent E3631A DC power supply which supplied 3 VDC. The uncalibrated and reference microphone signals were transmitted through a National Instruments 6143 16-bit data acquisition card and monitored by the LabVIEW control system. Due to the available power of the National Semiconductor

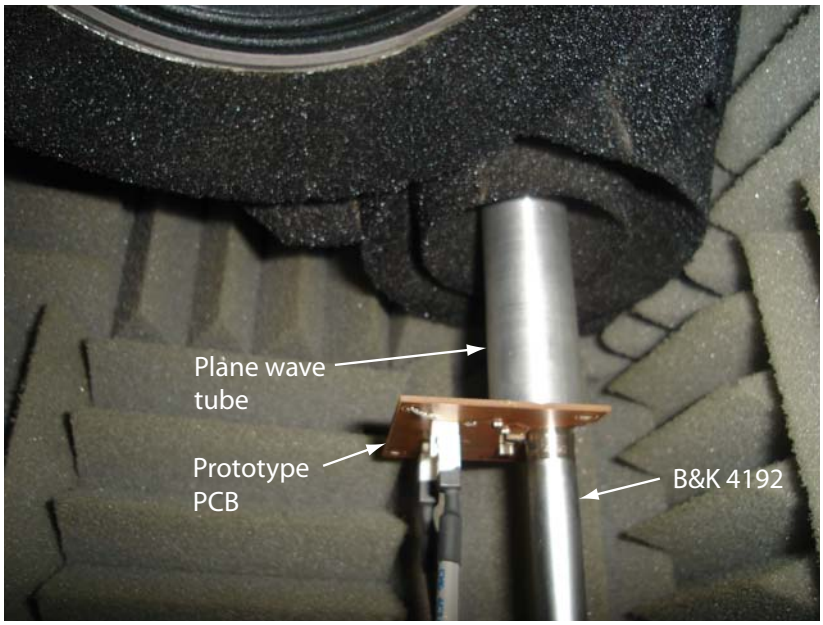

Figure 4.1: Plane wave tube calibration of prototype PCB in anechoic chamber

LM1875 amplifier, white noise was not used to provide the full spectrum sound source; rather pure tones were generated at distinct intervals. The amplitude of the signal emitted by the DE10 compression driver was monitored by the B&K 4192 microphone, and once stabilized at a chosen sound pressure level, measurements were made from the output of the MEMS microphones. An FFT was performed on the incoming MEMS microphone signals and a peak detector was used to determine the frequency and magnitude of the reference and uncalibrated microphone signals. A total of 20 consecutive sensitivity samples within 1% convergence were required at each test frequency for each MEMS microphone under test.

A method was devised to allow the microphones in the small-scale array to be characterized more generally. To overcome the issue of the small-scale array board geometry, six prototype PCBs each containing an SPM0408LE5H microphone and associated components were populated. Each PCB had a notch cut out to enable the reference microphone to be used simultaneously in a plane wave tube calibrator. A 22 mm inner diameter, 101.6 mm long normal incidence plane wave tube described in detail in McPhee was used to calibrate the microphones on these prototype PCBs [71]. Figure 4.1 shows a prototype PCB installed in the anechoic chamber using the plane wave tube for calibration. Calibrations with the plane wave tube were performed both inside and outside the anechoic chamber and no difference was noted in the influence of ambient sound levels.

4.2.1 Amplitude Response Tests

It was important to characterize the microphones in terms of amplitude response, to determine the range of sound pressure levels at which the microphone could be expected to show no variation in sensitivity. Published amplitude responses are uncommon and were not included for either MEMS microphone. The results of such an amplitude response test reveal mechanical limitations in the diaphragm material in response to the increasing pressure, or internal amplifier saturation as the amplitude of the amplified microphone signal begins to reach the supply voltage of the preamplifier. A further limitation can be saturation of the data acquisition hardware itself as the gain of the preamplifier can be adjusted sufficiently high to cause the microphone signals to swing above the data acquisition hardware's maximum input voltage. Operating on a 3 VDC supply, the 1 kHz sensitivity of the SPM0408LE5H microphone with 20 dB internal gain should show evidence of clipping, manifested as a decrease in sensitivity, for signals greater than approximately 113 dB. Similarly, the SPM0408HE5H microphones with 10 dB internal gain operating on 3 VDC should be clipped for signals of 122 dB.

The plane wave tube setup was used for simultaneous calibration with a pure tone. Microphones in both arrays were subjected to amplitude response tests performed with a 1 kHz tone, referenced to the B&K 4192 microphone, between 90 dB and 130 dB, in 0.5 dB steps. The small-scale array microphones were tested using the 6 single PCBs and the microphones in the large-scale array were tested on their individual PCBs. Typical results of the amplitude response testing are shown for one microphone of each type in Figure 4.2.

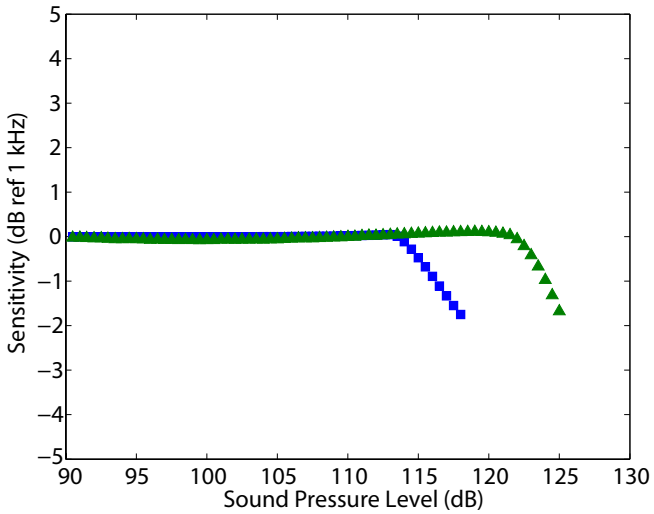

Figure 4.2: Amplitude response calibration results ■ SPM0408LE5H 20 dB gain ▲ SPM0408HE5H 10 dB gain

It is evident that both microphones show little deviation in sensitivity up to a given sound pressure level, at which point a sharp decline in sensitivity is noted. The plummeting sensitivity indicates that a limit has been reached either mechanically or electrically. In this case, the limiting factor was the microphone supply voltage since the peaks of the corresponding amplified input signal were clipped at the amplifier supply voltage. As expected, the SPM0408LE5H microphones show evidence of saturation at approximately 113 dB while the SPM0408HE5H microphones appear to saturate at approximately 121 dB. As further evidence of clipping, lowering the microphone supply voltage below 3 VDC has the effect of lowering the sound pressure level at which the sensitivity diminishes. For high microphone amplifier gains, the microphones should therefore be powered at the highest limits of their supply voltage. However the manufacturer's microphone specifications list the total harmonic distortion of both units as less than 10% at signals of 115 dB, these microphones clearly exhibit adverse behaviour and are therefore less suitable for operation at these sound pressure levels.

4.2.2 Frequency Response Tests

As mentioned above, the usable frequency range of a plane wave tube is limited by its physical dimensions. For the 22 mm diameter, 101.6 mm long tube the reliable frequency range is found to be approximately 850 Hz to 6 kHz. In order to characterize the microphones in the small-scale array, calibration in terms of frequency response was performed on the six single microphone PCBs using simultaneous calibration. The microphones in the large-scale array were calibrated in the same way prior to being installed in their frame. The frequency response was tested at 1/12 octave intervals between 850 Hz and 6 kHz. The control system was configured to output a constant 104 dB signal for each signal, referenced to the B&K 4192 microphone. The sound pressure level was selected as 104 dB instead of the standard 94 dB to improve the signal to noise ratio inside the plane wave tube while ensuring the amplifiers in the microphone packages would not saturate. Detailed frequency response tests were performed on 6 microphones from each array, repeating each calibration at least six times to ensure repeatable results. Typical calibration results for a single microphone from each array, averaged over six tests are shown in Figures 4.3 and 4.4.

In the plane wave tube's usable frequency range, the SPM0408LE5H microphone response differs from the manufacturer's published response quite significantly. Six of each microphone type were tested and found to have very similar responses. It was suggested that the strong increase in sensitivity with increasing frequency is the result of the 1 mm wide, 1.5 mm long acoustic port passing through the small-scale array's PCB, leading to resonance at a lower than expected frequency. The SPM0408HE5H microphone showed much better correlation with the published data. Some of the slight discrepancies in this frequency range can be attributed to the use of the plane wave tube, a pressure field device,

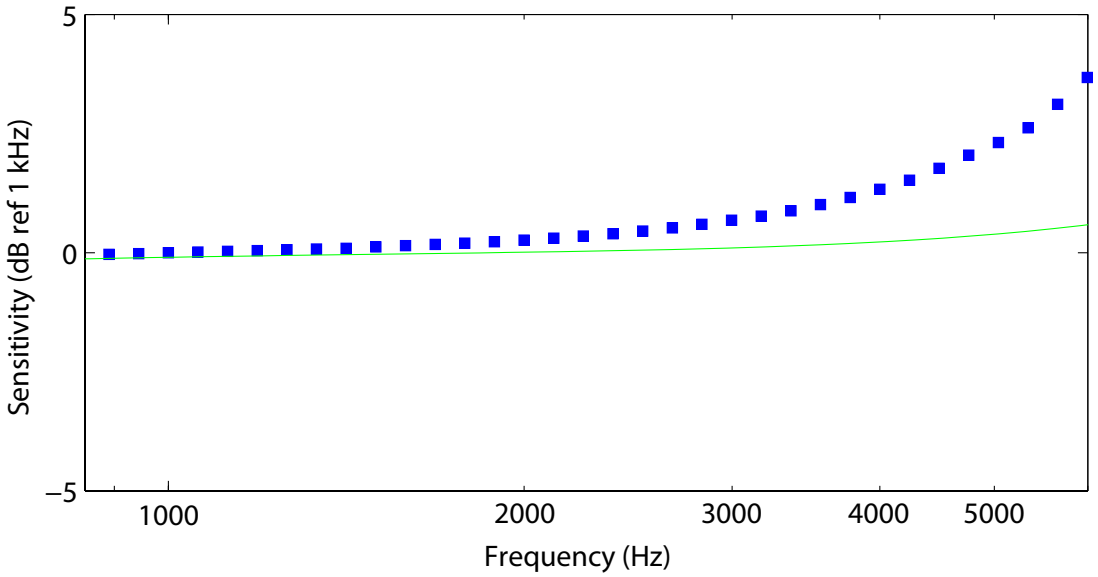

Figure 4.3: Typical frequency response for SPM0408LE5H microphone [56] — Published frequency response ■ Measured frequency response

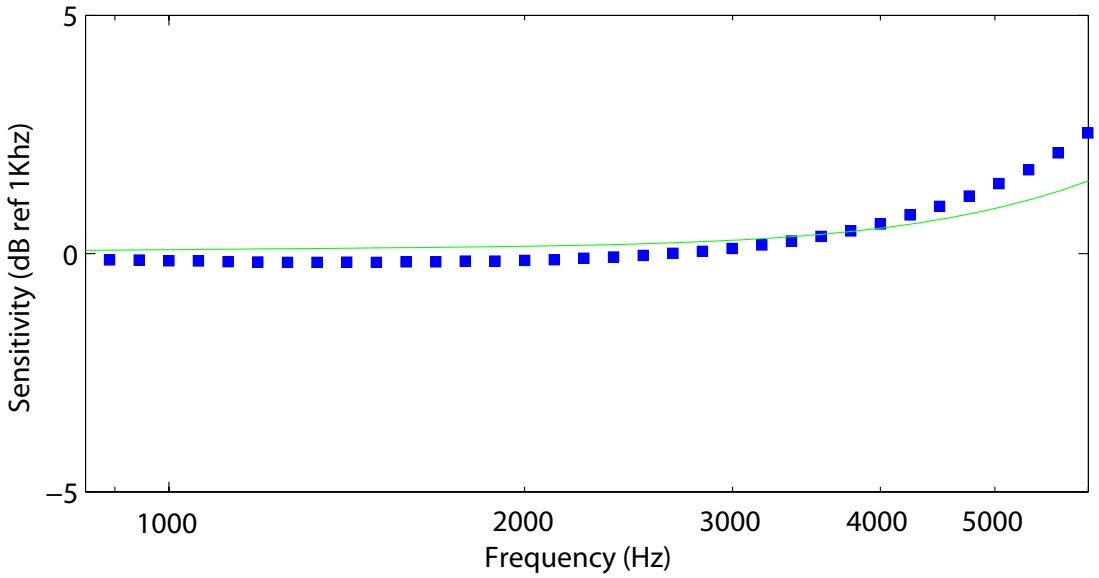

Figure 4.4: Typical frequency response for SPM0408HE5H microphone [58] — Published frequency response ■ Measured frequency response

since the Knowles microphones are reportedly calibrated with respect to their free-field response in an anechoic chamber. Due to the reduced applicability of the limited frequency range available in testing and the strong correlation with the published data in this frequency range, a decision was made to use the published data across the entire published frequency range, 100 Hz to 10 kHz. There was little variation between microphones in the same production batch which was verified by detailed calibration results of numerous Knowles transducers of a similar design over a much wider frequency range; the frequency responses of the various devices were in excellent agreement with one another [73].

Noting that the sensitivities of both microphones tended to increase with increasing frequency, Helmholtz resonance was suspected. Very little could be done to the small-scale array microphones in terms of altering the acoustic pathway through the PCB since it has a fixed thickness and the port hole could not be widened as it is used to seal the acoustic cavity below the microphone port. Acoustic vent materials were not tested and might prove worthwhile in reducing the high frequency sensitivity increase by adding an acoustic resistance. A number of techniques to improve the frequency response of the SPM0408HE5H microphones used in the large-scale array were tested. Noting that the acoustic pathway is provided from one end of the microphone to the other, the casing of a single test microphone was removed, reoriented, and reattached to align the port hole and diaphragm. This had no noticeable effect on the measured frequency response. The case was also removed entirely and again the frequency response measured as before. The frequency of this microphone closely matches the expected response and it is therefore assumed that the response is unaffected by Helmholtz resonance in the tested frequency range. Again, it may be possible to flatten the frequency response by forcing the resonant peak to a higher frequency, using an acoustic vent to provide an acoustic resistance, but this was not tested.

4.2.3 1 kHz Sensitivity Tests

Having performed detailed tests of six of each microphone type and deciding to use the manufacturer's published response over the entire published frequency range, it was necessary to determine the sensitivity of the microphones at a single point along the frequency response to obtain the sensitivity offset at a reference frequency. A single point calibration was performed at 1 kHz, since this is the common reference frequency used in microphone frequency response calibration. For the small-scale array, these tests were performed in-situ using a substitution method. A 20 mm thick aluminum disc with a cylindrical Teflon insert was coupled to the B&C DE10 compression driver. The B&K 4192 reference microphone was coupled to the disc through the Teflon insert. The compression driver was provided with a 1 kHz tone from the DAQ and amplifier and the microphone's output was monitored. The output voltage from the DAQ corresponding to a 104 dB signal was noted. The reference microphone and Teflon insert were removed and the aluminum disc was then

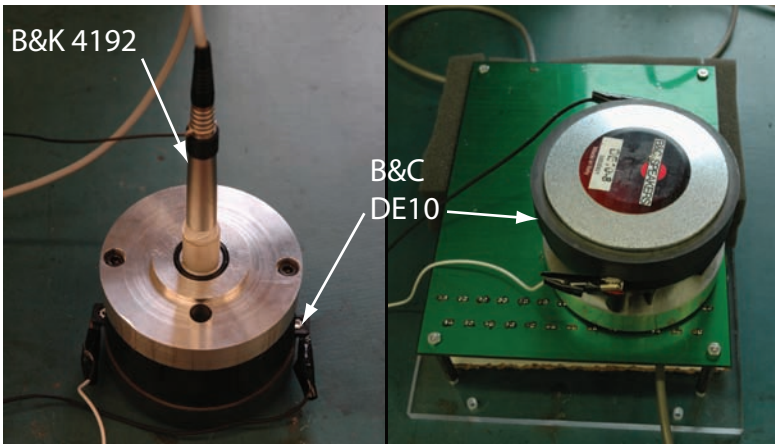

Figure 4.5: Substitution calibration arrangement with small-scale array

placed over each microphone in the array using an O-ring to seal the interface between the disc and PCB. The 104 dB signal was then applied to each microphone and the resulting sensitivity was recorded. The amplitude of the source was verified again once during the tests and once upon completion of the tests to ensure the temporal stability of the sound source. The microphones were each calibrated 6 times and showed deviation of less than 2 mV/Pa between tests. The substitution setup can be seen in Figure 4.5. Calibration results from the 1 kHz sensitivity tests are presented in Appendix B.

Since the large-scale array microphones could be calibrated simultaneously with the reference microphone, the substitution technique was not used. Rather, 1 kHz sensitivity calibration of the microphones in the large-scale array was performed using simultaneous calibration in the plane wave tube calibrator prior to the installation of the microphones in the array structure. These tests were performed 9 times per microphone and showed deviation of less than 1 mV/Pa between successive measurements. The results of the calibration of the microphones in the large-scale array can also be found in Appendix B.

4.2.4 Phase Tests

Due to the difficulties encountered in calibration, detailed phase measurements were not performed. The goal of such a calibration is to ensure that the phase measured by all microphones in response to an acoustic impulse can be related. There are a number of methods for testing the phase response of a microphone over a range of frequencies but none could be readily adapted with the current calibration system. Calibrating microphone phase over a broad frequency range requires that the reference microphone and uncalibrated transducer be subjected to precisely the same sound field, such that the incoming wave has no difference in delay with respect to the reference microphone and uncalibrated microphone. Very

small deviations in microphone position between tests would have a significant influence on the accuracy of phase measurements at high frequencies since a small variation in microphone position would create a measurable difference in microphone phase for signals with short wavelengths. Such controls were difficult to achieve using the substitution or simultaneous methods since the sound source could not be guaranteed to activate in the same fashion for each test and small spatial variations in the calibration setup were difficult to avoid. Since all microphones in each array were obtained from the same production batch, utilize the same preamplification circuitry, and were precisely located on their respective array frames by great care undertaken in design and fabrication of the arrays, phase has been assumed to be consistent throughout the array. The consistency of phase throughout the batch of MEMS microphones was further supported by previous work performed on similar Knowles microphones [53] and on other MEMS microphones of similar design [68]. Phase calibration of the microphones with respect to each other was accomplished once the microphones were installed in the array, using a known sound source at a known location. All microphones showed the expected phase response based on their distance from the impulse sound source. The lack of phase calibration information is considered a minor source of error, although it is certainly worthy of future exploration.

Chapter 5

Experimental Setup

This section outlines the equipment and procedure used in experimental testing of both arrays. Details are provided for hardware and software implemented in data acquisition, signal processing, and source generation. An overview of test cases is presented.

5.1 Data Acquisition

The primary requirement for beamforming is that signals are recorded simultaneously. It is therefore necessary to have data acquisition hardware capable of simultaneously sampling numerous channels at a high data rate. For data collection of both arrays, eight National Instruments NI 9237 modules were used in combination with a National Instruments cDAQ-9178 chassis [74,75]. Each of the eight NI 9237 module contains four 24-bit analog inputs for an available 32 simultaneous analog channels sampling at 50 kHz. The channel inputs are comprised of RJ50 connectors and are commonly employed for strain bridge measurements in the range of ± 25 mV, although choosing to scale by an excitation voltage of 10 V allows the range to be increased to ± 250 mV, making it well suited to amplified microphone measurements. The chassis uses a USB 2.0 Hi-Speed interface, allowing for data transfer of all channels at their maximum sampling rate. A table of microphone connections to the DAQ for both arrays is provided in Appendix A.

All measurements of both arrays were made using this DAQ with the sampling rate of each channel at 50 kHz. Data collection was controlled through a LabVIEW [76] environment allowing the user to vary the collection period and sampling rate if desired. The microphone signal acquisition software can be found in Appendix C. Data were recorded in binary form to reduce file size.

5.2 Signal Processing

Conventional beamforming with diagonal removal was performed in MATLAB in the frequency domain primarily using the algorithm reported in Orlando [17]. The user has the ability to specify the sampling rate of the hardware, length of each FFT block, number of blocks to use in the FFT, source map scanning frequency, scanning grid dimensions, and scanning grid location. Details of block length and number of blocks are provided for each test case in their respective sections.

5.3 Test Cases

A number of source types were used in the experiments. Testing was carried out with the small-scale array using a single monopole sound source at a known location. The monopole source configuration was also implemented for tests conducted with the large-scale array. Additional testing of the large-scale array was performed using a single stationary piezo buzzer, multiple stationary buzzers, and a rotating piezo buzzer. These test cases are outlined in detail below. Due to the absence of a suitable anechoic facility, all tests were performed inside a laboratory with many reflective surfaces. Efforts were made to mitigate the reflectivity of the environment; however, the measured array responses are subject to additional sound sources unaccounted for in the theoretical responses. While this makes comparison of experimental and theoretical results difficult, it does represent a more accurate depiction of array performance in a typical measurement environment. Finally, acoustic testing was performed on a 600 watt turbine with 1.3 m rotor diameter in an open-jet wind tunnel facility.

An important consideration in the analysis of experimental results is that mounting the microphones coincident with a plane wall surface contributes to a doubling of the pressure received at the microphone diaphragm as a result of standing waves created by reflection off the microphone array's plane wall frame. All microphone measurements must be reduced by 6 dB to remove this perceived increase in sound pressure level.

5.3.1 Small-Scale Array with Stationary Monopole Source

Initial testing of the array was performed using a single acoustic source emitting a single tone. The sound source for these preliminary tests consisted of a Philips PM5132 function generator providing a sinusoidal signal to a B&C DE10 compression driver which was connected to a 370 mm long, 12.7 mm inner diameter tube to create a monopole point source. The compression driver and tube were mounted to a sliding stand such that the position of the sound source could be moved precisely along an axis. The test apparatus is shown in use with the small-scale array in Figure 5.1. Specific details of each test case are shown in Table 5.1.

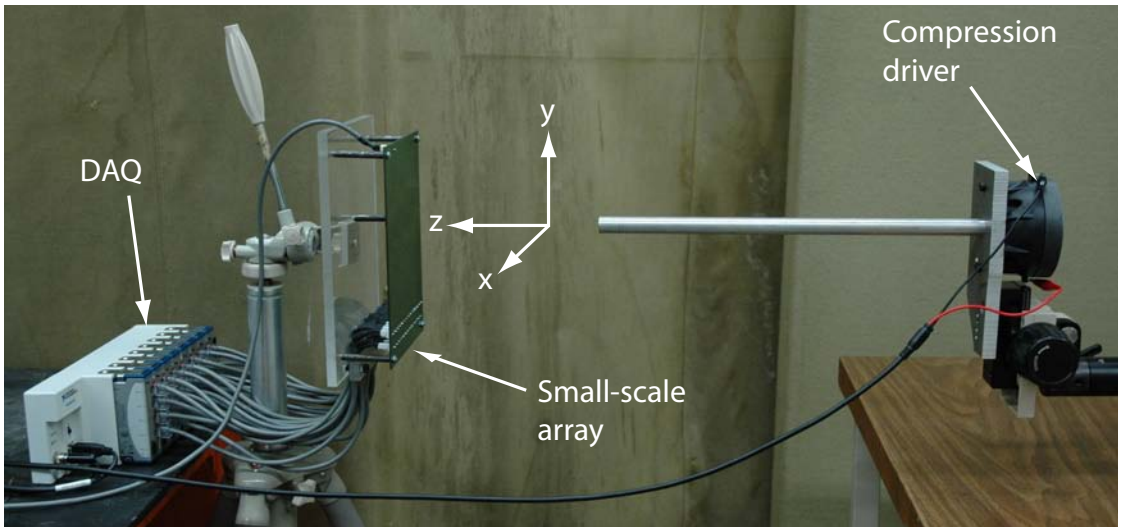

Figure 5.1: Compression driver monopole source setup with small-scale array

The compression driver test apparatus was used as a monopole sound source for source localization in conjunction with the small-scale array in test cases 1–10, for frequencies of 3, 4, 5, 6, and 7 kHz. Cases 1–10 presented in Table 5.1 constitute the extent of testing with the small-scale array, with the distances chosen to represent solid collection angles, the angle subtended by the array's aperture and the source, of 10° and 45°. In all cases the sound source was aligned with the array origin using a laser, in place of the aluminum tube. The array centre to source plane centre distance, z, was varied for each frequency. Since the two source positions used in these tests were performed in close proximity to each other the source could be slid along the stand without moving its base, allowing for laser positioning accuracy of approximately ± 1 mm. Each microphone recorded approximately 8.2 seconds of audio for each test case.

Further testing of the small-scale array in the small closed-loop wind tunnel revealed limitations in the array's applicability. The goal of using the small-scale array in the small closed-loop wind tunnel was abandoned when preliminary testing indicated the background noise in the facility was far too high for the microphones. The array was placed flush in the wind tunnel, replacing one of the test section walls. Even at modest wind speeds, the output voltages from the amplified microphones were saturated. The primary cause of high background noise was microphone self-noise due to the boundary layer. The microphone array may be of further use in this facility by lowering the gain of the preamplifiers, which can be readily accommodated, or by recessing the microphone array, possibly behind a Kevlar® sheet as implemented in the Virgina Polytechnic Institute and State University Stability Wind Tunnel [29], but this was not tested.

Table 5.1: Small-scale array test cases with stationary compression driver source

Test case	z (mm)	Source f (kHz)
1	164	3
2	164	4
3	164	5
4	164	6
5	164	7
6	385	3
7	385	4
8	385	5
9	385	6
10	385	7

5.3.2 Large-Scale Array with Stationary Monopole Source

The compression driver and tube configuration was used to provide a monopole source for testing the large-scale array, as shown in Figure 5.2, with sinusoidal inputs of 1, 3, 5, 7, and 9 kHz at source distance of 333 mm, 500 mm, 1000 mm, and 2000 mm.

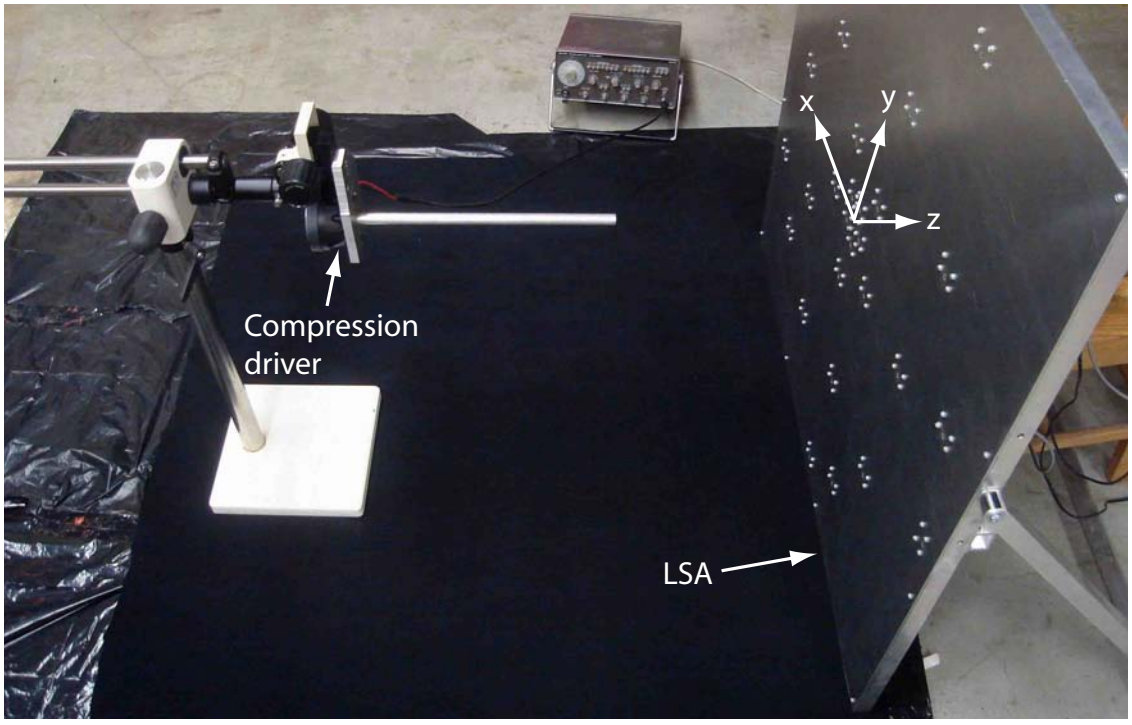

Figure 5.2: Compression driver monopole source setup with large-scale array

Table 5.2: Large-scale array test cases with stationary compression driver source

Test case	z (mm)	Source f (kHz)
11	333	1
12	333	3
13	333	5
14	333	7
15	333	9
16	500	1
17	500	3
18	500	5
19	500	7
20	500	9
21	1000	1
22	1000	3
23	1000	5
24	1000	7
25	1000	9
26	2000	1
27	2000	3
28	2000	5
29	2000	7
30	2000	9

Details of Cases 11–30 can be found in Table 5.2. The distances from the source to the array used in testing the large-scale array represent solid collection angles of 70°, 50°, 26°, and 13° respectively. Since the sound source was located at greater distances from the array, the base of the stand had to be moved for each distance. Consequently the laser alignment technique was inherently less accurate and was able to provide accuracy in the positioning of the source of approximately ±5 mm. Approximately 3.3 seconds of audio were recorded.

5.3.3 Large-Scale Array with Stationary Buzzer Sources

Since a known, rotating sound source would ultimately be tested, a portable device was required for sound generation. Piezo buzzers were selected for their inherent convenience and flexibility. Piezo buzzers were selected as a sound source as they can be operated directly from a battery power source, where the sound pressure level is determined by the input voltage, so they could be utilized as a known, moving sound source. Since they did not require a power supply connected to the mains supply they could be easily

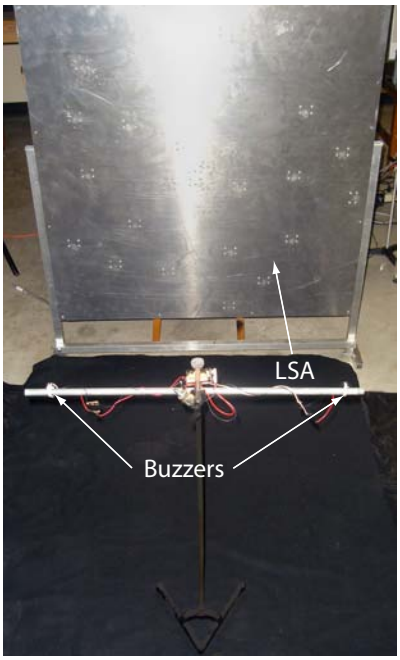

Figure 5.3: Multiple buzzer source configuration

rotated without adding unnecessary complications such as slip rings. Before attempting to measure a rotating buzzer source it was necessary to quantify the performance of a piezo buzzer by comparing with measurements of the compression driver sound source under similar circumstances. Preliminary test results indicated that a single buzzer source was a suitable sound generator and exhibited similar behaviour to the monopole source tested earlier.

The piezo drivers were capable of reaching sound pressure levels of approximately 100 dB and operated at a fixed frequency. The buzzer sound pressure levels were controlled by potentiometers controlling the input voltage. Two buzzer types were chosen to provide greater flexibility in testing. The buzzer types are distinguished by their nominal frequencies: 2.9 kHz and 4.4 kHz. Tests to characterize the array's performance in the presence of multiple sources were conducted using two stationary buzzer sources attached to a horizontal rod mounted to a retort stand, as shown in Figure 5.3, using two separation distances and two source frequencies.

In these test cases efforts were made to roughly align the sound sources with the array; however, the important dimension in assessing array performance was the separation distance between the sources. Two buzzers were placed along the same plane and the frequencies and distance between sources were varied. These tests were used to demonstrate the array's ability to resolve multiple sources at the same frequency in a source map and suppress sources at frequencies other than those of interest. The source sound pressure

Table 5.3: Large-scale array test cases with multiple stationary buzzer sources

Test case	z (mm)	Source separation (mm)	Source f (kHz)
31	1000	280	4.4
32	1000	530	4.4
33	1000	530	2.9, 4.4

levels of both buzzers were matched within approximately 1 dB. Details of these test cases are outlined in Table 5.3.

5.3.4 Large-Scale Array with Rotating Buzzer Source

Additional testing was performed with rotating buzzer sources. A rotating source, intended to represent a small-scale wind turbine, was created by attaching two aluminum bars with 3.2 mm thickness, 25.4 mm width, and 420 mm length to the collar of a DC motor. Each buzzer was located at a radial distance of 475 mm. The rotor plane was located at a distance of 1000 mm from the array. This setup can be seen in Figure 5.4. These tests were performed with the intent of determining the effect of mainlobe spreading in time-averaged source maps due to source motion and to dedopplerize a moving source in the time domain.

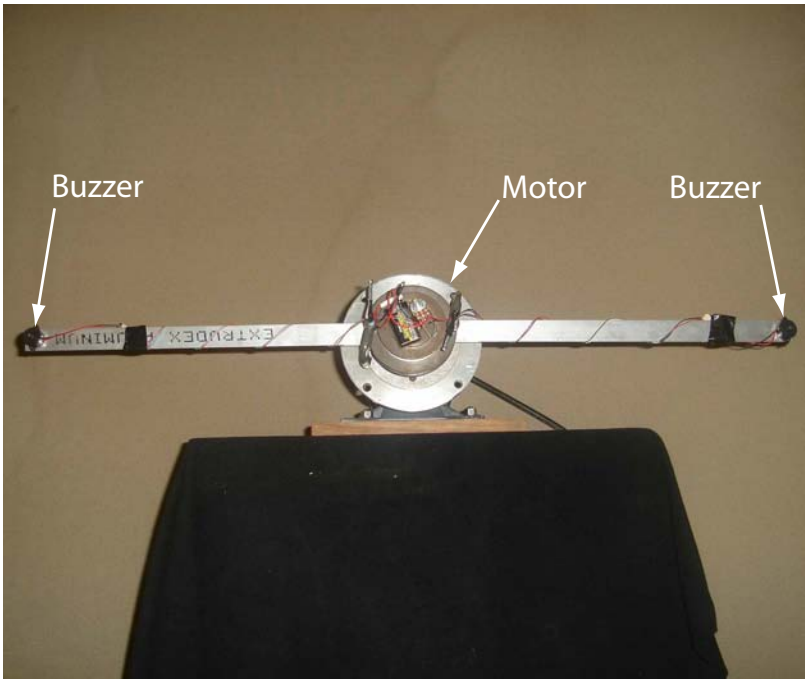

Figure 5.4: Rotating buzzer source setup

Buzzers were attached to the ends of the aluminum bars to provide a known rotational sound source. Tests were conducted using a single buzzer source at a fixed rotational rate. The rotating axis was approximately 230 mm above the array's origin, so the array's focus was at an upward angle of roughly 13°. Details of the rotational test case can be found in Table 5.4.

Table 5.4: Large-scale array test cases with rotating buzzer source

Test case	z (mm)	Rotational speed (rpm)	No. of sources	Source f (kHz)
34	1000	170	1	4.4

5.3.5 Large-Scale Array Tests with Small Wind Turbine

Tests were conducted in an open-jet wind tunnel with a 610 mm square test section. The tunnel discharges into atmospheric conditions in the laboratory and incorporates external diffuser vanes to redistribute the flow upward through the laboratory. No acoustic treatment was added to the facility or measuring environment. A three-bladed, 600 watt turbine was placed along the centreline of the test section outlet at a distance of 1600 mm from the tunnel outlet, as shown in Figure 5.5.

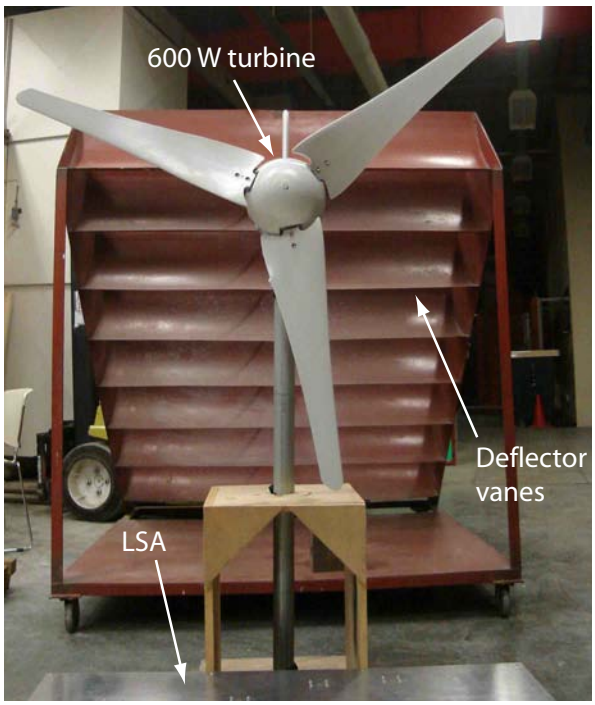

Figure 5.5: 600 watt, 1.3 m diameter turbine test configuration as seen from the open-jet test section

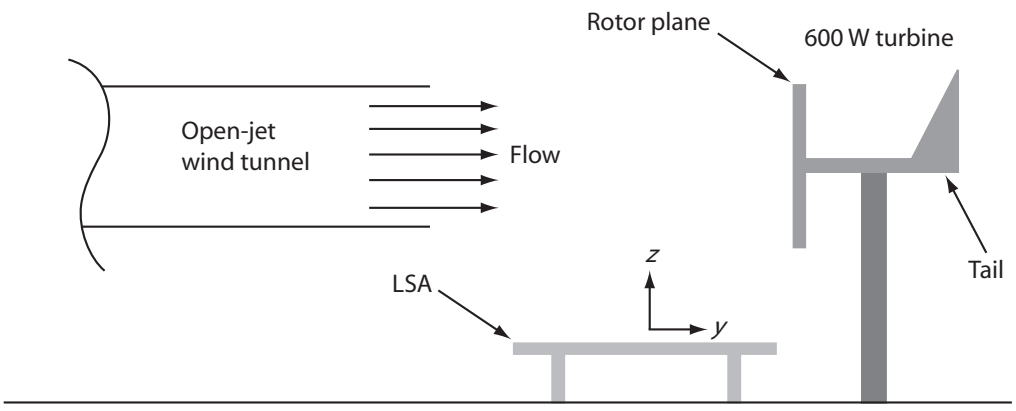

Figure 5.6: Simplified diagram of open-jet wind tunnel testing of 600 W wind turbine (not to scale)

The turbine has a rotor diameter of approximately 1.3 m, with unknown airfoil geometry having a chord ranging from 152 mm near the root to 46 mm at the tip. The turbine is an upwind design with a tail controlling yaw, providing alignment with the freestream velocity. The large-scale microphone array was positioned slightly above the floor, approximately 850 mm below the centreline of the test section. As opposed to a parallel arrangement between the array and scan plane as in all previous experimental configurations, the array was laid along the floor, perpendicular to the rotor plane. The array's centre was located at an upstream distance of approximately 510 mm from the turbine rotor plane, 1000 mm below the centre of the turbine rotor. A diagram showing the experimental setup is shown in Figure 5.6.

Data sampling occurred for approximately 1.64 seconds, during which the turbine rotor made many revolutions at a constant speed. The turbine generator was not connected to a load and was therefore allowed to freewheel. Four wind speeds were tested: 2.5 m/s, 3.5 m/s, 4.5 m/s, and 5.5 m/s. Freestream wind speed measurements were made with a Kestrel 1000 anemometer along the tunnel centreline at a distance of 1 metre from the test section outlet. The tested wind speeds corresponded to respective rotational rates of the turbine of approximately 295 rpm, 360 rpm, 550 rpm, and 640 rpm, measured with a strobe light. The respective nominal Reynolds numbers at the tip of the blade were approximately 59 000, 72 000, 110 000, and 130 000. In all cases background noise levels observed at the centre of the microphone array during wind tunnel operation were approximately 70 dB at frequencies less than 600 Hz decreasing to roughly 40 dB at frequencies above 4 kHz.

Chapter 6

Experimental Results

The following chapter provides results of experimental testing used to validate the performance of both arrays. Source maps are presented for measurements made in the non-anechoic measuring environment. Comparisons between experimental and theoretical source maps in response to known sources are presented. The large-scale array's ability to localize and distinguish multiple sources is also demonstrated. Results from testing of a known, rotating source are presented. Experimental results from wind tunnel testing of a 600 watt, 1.3 metre turbine are included. For clarity and brevity all source maps are shown in two dimensions with filled contours. For definitions of parameters in the scan plane and array coordinate system refer to Figure 2.2.

6.1 Small-Scale Array with Stationary Monopole Source

The following figures reveal the array's response to a single sinusoidal source oriented along the z-axis of the array, using the configuration shown in Figure 5.1. Both theoretical and measured responses are shown for comparison. Referring to Table 5.1, Cases 1, 3, 5, 6, 8, and 10 are presented to demonstrate the effects of increasing frequency and source distance. Source maps for additional cases can be found in Appendix D. For ease of comparison between theoretical and measured results, all source maps in this section are normalized by their maximum sound pressure levels and are therefore referenced to a maximum of 0 dB. A dynamic range of 9 dB is shown. All source maps are based on one-third octave bands surrounding the specified frequency. Source maps for Cases 1–5 encompass one square metre scan area with a grid spacing of 5 mm with the centre of the source map being located on the array's z-axis. Source maps used in Cases 6–10 also locate the centre of the scan plane along the z-axis and represent a scanning grid of 4 square metres with a grid spacing of 10 mm. FFT computations are based on block lengths of 8192 samples with a total of 50 blocks being averaged.

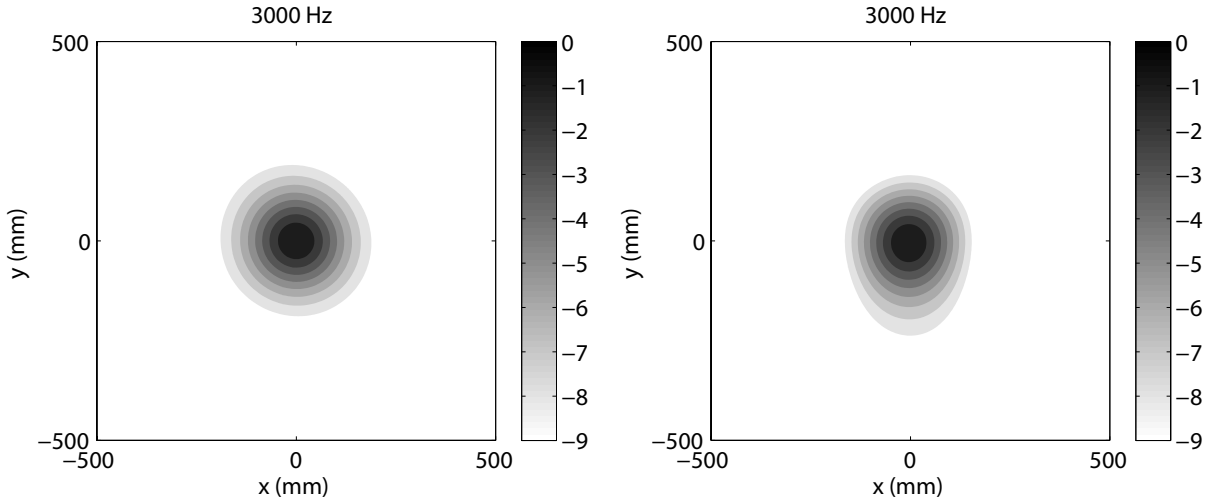

Figure 6.1: Theoretical (left) and measured (right) SSA response for Case 1: 3 kHz monopole source along z-axis at 164 mm, 74.0 dB peak

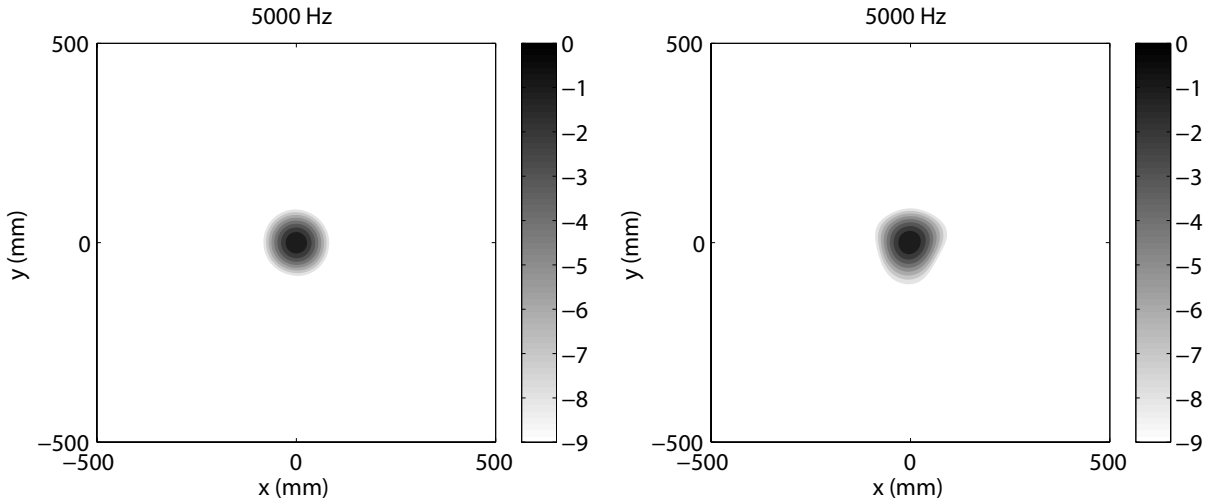

Figure 6.2: Theoretical (left) and measured (right) SSA response for Case 3: 5 kHz monopole source along z-axis at 164 mm, 84.2 dB peak

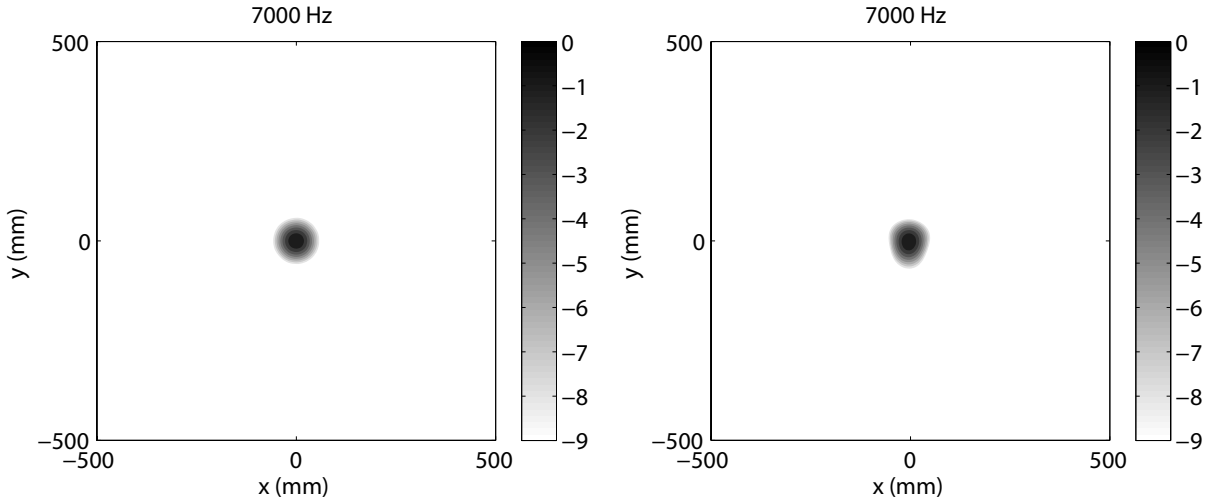

Figure 6.3: Theoretical (left) and measured (right) SSA response for Case 5: 7 kHz monopole source along z-axis at 164 mm, 88.2 dB peak

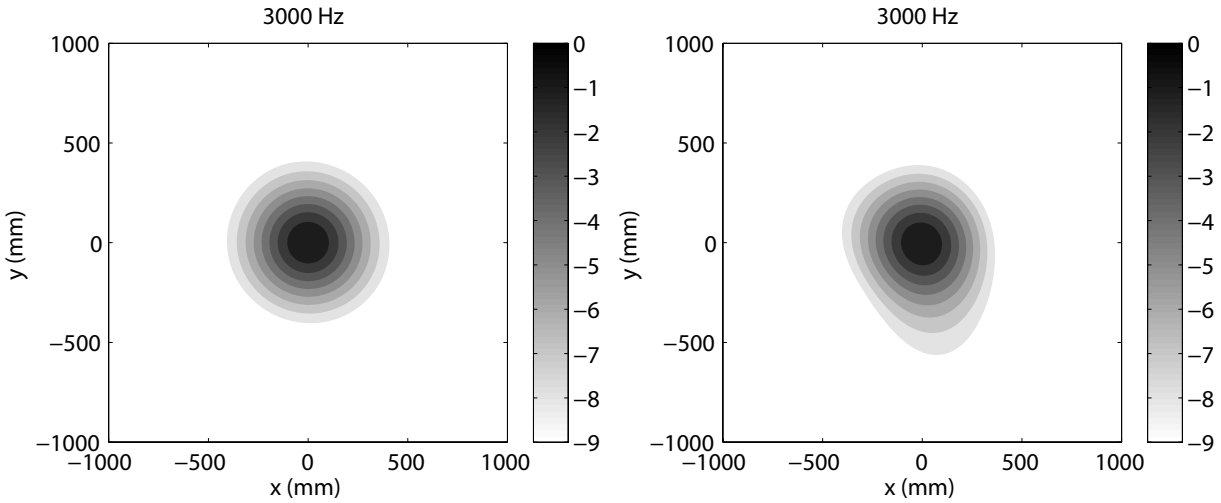

Figure 6.4: Theoretical (left) and measured (right) SSA response for Case 6: 3 kHz monopole source along z-axis at 385 mm, 74.7 dB peak

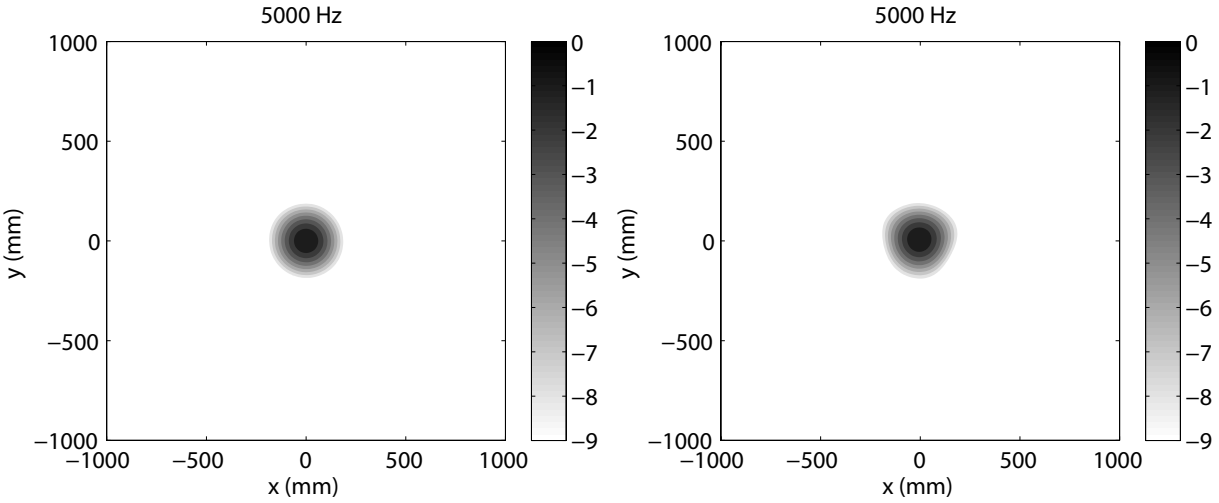

Figure 6.5: Theoretical (left) and measured (right) SSA response for Case 8: 5 kHz monopole source along z-axis at 385 mm, 83.0 dB peak

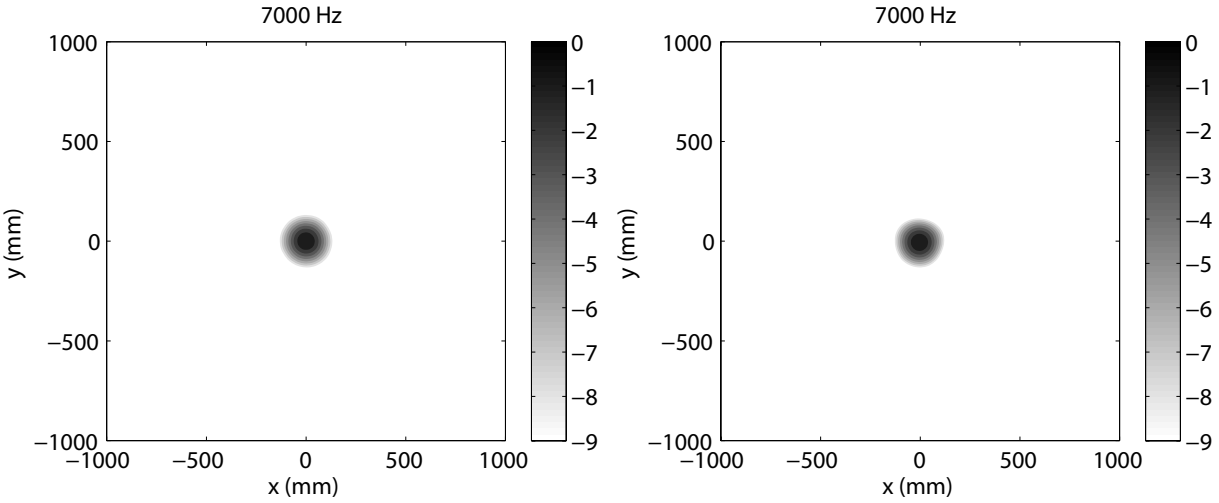

Figure 6.6: Theoretical (left) and measured (right) SSA response for Case 10: 7 kHz monopole source along z-axis at 385 mm, 88.6 dB peak

All source maps indicate that the array is able to locate the source within the precision of the laser alignment technique. Qualitatively the beamwidth is noted to decrease with increasing frequency. Figure 6.7 shows the -3 dB beamwidths obtained from the theoretical and measured source maps from Cases 1–10. These beamwidths are shown as a function of source frequency. Sidelobes are not present in any of the maps, indicating that at

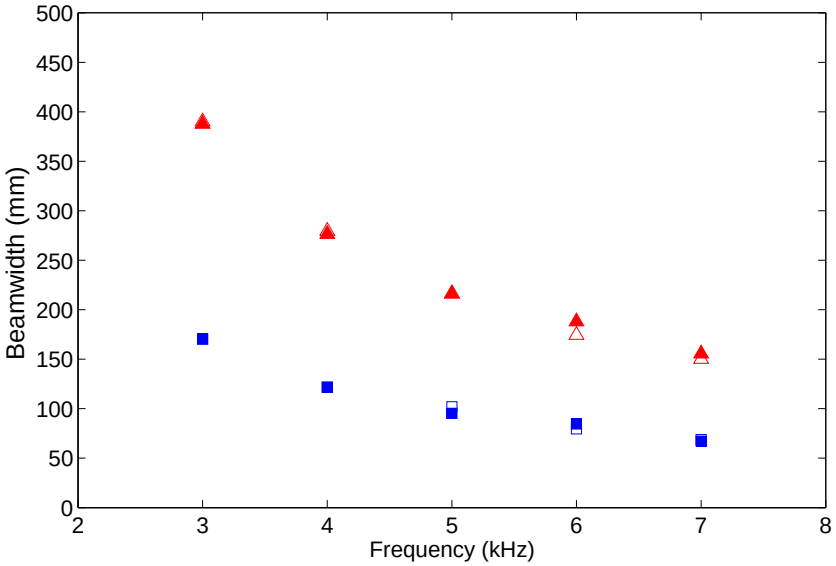

Figure 6.7: SSA beamwidth as a function of monopole source frequency □ Theoretical at 164 mm ■ Measured at 164 mm △Theoretical at 385 mm ▲ Measured at 385 mm

the distances tested, the array's signal-to-noise ratio is greater than 9 dB. At such close distances, the acoustic environment does not seem to have significant influence on the sound field.

It is apparent that at closer distances and at higher frequencies the beamwidth decreases. The beamwidth is shown to be inversely proportional to source frequency as expected. As mentioned, the beamwidth is an important parameter in determining the functionality of the array since it dictates the array's spatial resolution. Based on the results of the small-scale array tests, two 7 kHz sources at 164 mm would require at least 67 mm separation to be resolved as separate sources; otherwise, the two sources would be represented a single, spread out mainlobe. Similarly, two 3 kHz sources at 385 mm would require a minimum of 388 mm separation to be resolved. The intended application of the small-scale array was to measure an aeroacoustic source such as an airfoil with a chord length on the order of 50 mm in the small-scale wind tunnel with its 152.4 mm test section. However, based on the beamwidths presented in the frequency range tested, it would be difficult to precisely determine the location of multiple acoustic sources since the beamwidth would be greater than the airfoil chord, making it difficult to distinguish leading edge noise from trailing edge noise for instance. However, provided trailing edge noise is the dominant mechanism in wind tunnel airfoil tests, as it has shown to be in low turbulence conditions, the difference in sound pressure levels between sources should be great enough that the array should suffice in locating emissions from the trailing edge.

Furthermore, the primary value of the small-scale array is its ability to improve the signal-to-noise ratio over measurements made with a single microphone. The small-scale array was not successful in preliminary testing in the small closed-loop wind tunnel, due to the high levels of self-noise due to the boundary layer as mentioned in Section 5.3.1. However the performance of the array in the test cases above reveals its potential in aeroacoustic applications, provided the test section of the closed-loop wind tunnel can be modified to locate the microphone array outside of the flow.

6.2 Large-Scale Array with Stationary Monopole Source

Presented below are the large-scale array's theoretical and measured responses to a monopole source along its z-axis as shown in Figure 5.2. Filled contour source maps normalized by the maximum sound pressure level are presented for Cases 11–15, 18, 23, and 28, detailed in Table 5.2. These cases are selected to show the variation in array response with respect to increasing frequency at constant distance, and increasing distance at constant frequency. One-third octave bands are used. A dynamic range of 9 dB is shown. All source maps place the centre of the scan plane along the z-axis and represent 4 square metres with a grid spacing of 10 mm. Fast Fourier transform computations are based on 20 blocks containing 8192 samples. Additional source maps for cases not shown here are presented in Appendix D.

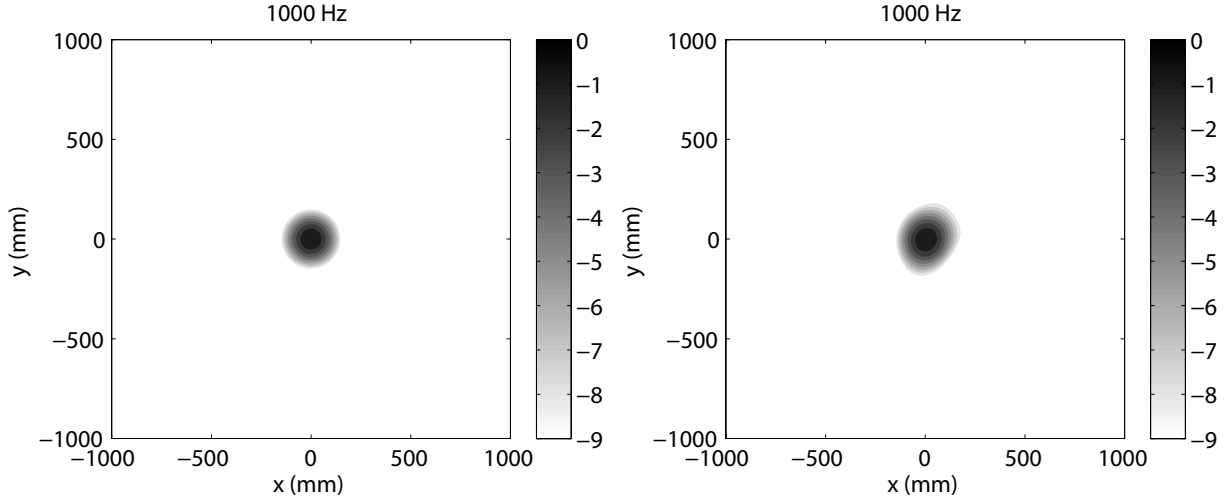

Figure 6.8: Theoretical (left) and measured (right) LSA response for Case 11: 1 kHz monopole source along z-axis at 333 mm, 95.3 dB peak

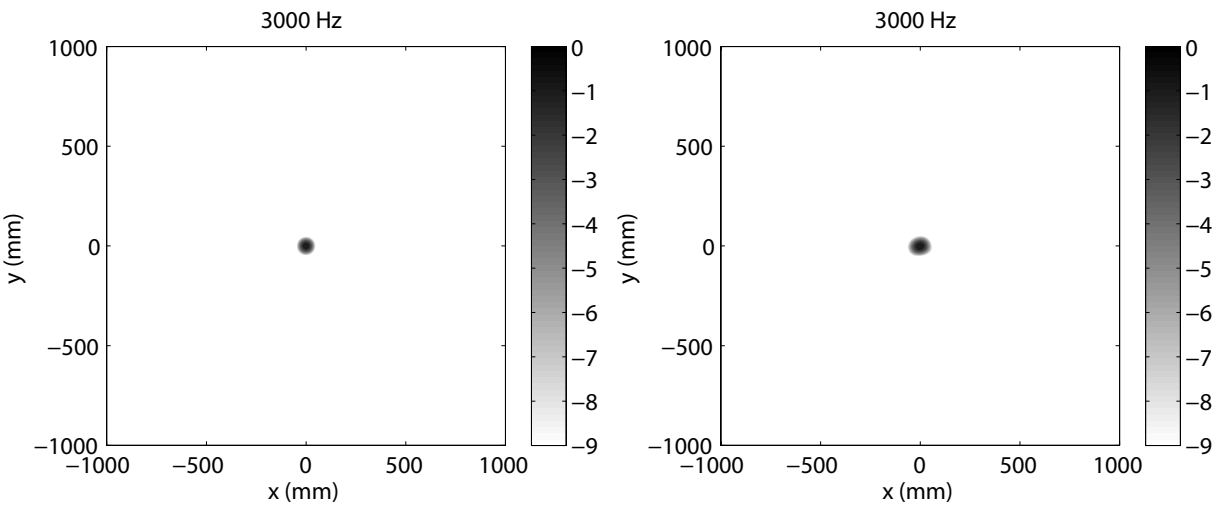

Figure 6.9: Theoretical (left) and measured (right) LSA response for Case 12: 3 kHz monopole source along z-axis at 333 mm, 92.1 dB peak

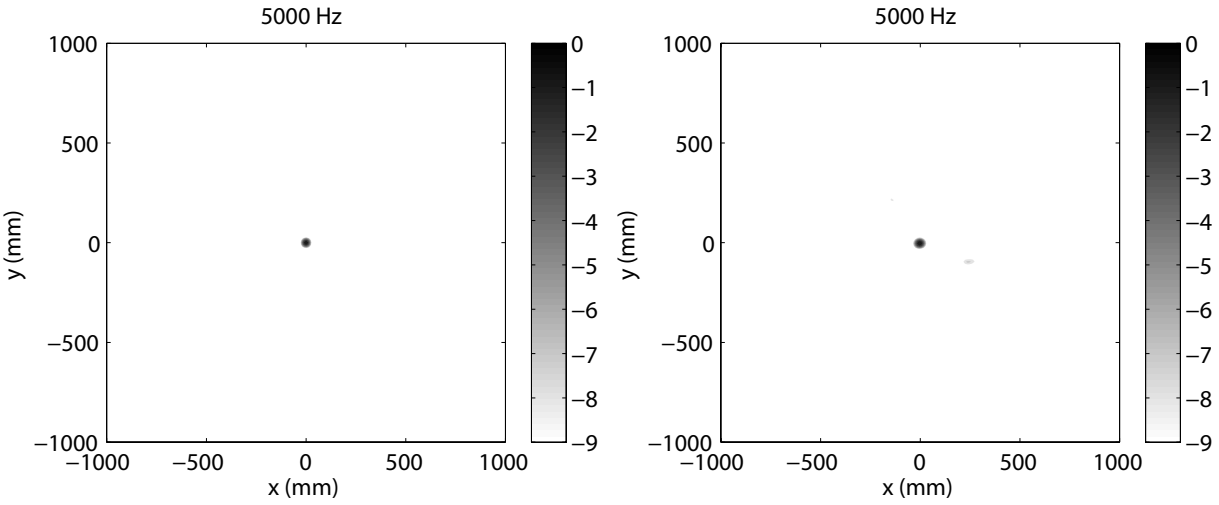

Figure 6.10: Theoretical (left) and measured (right) LSA response for Case 13: 5 kHz monopole source along z-axis at 333 mm, 97.1 dB peak

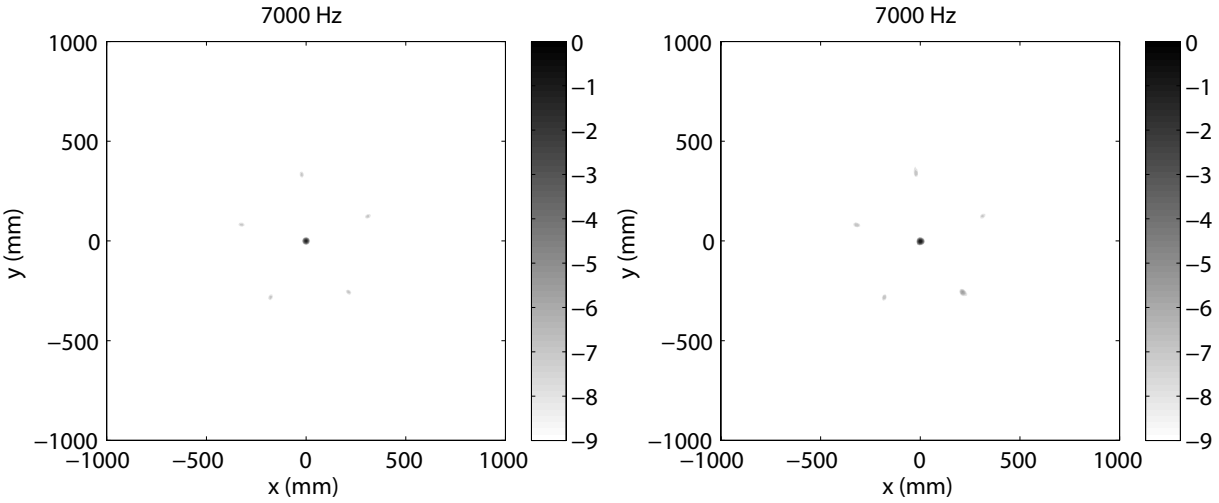

Figure 6.11: Theoretical (left) and measured (right) LSA response for Case 14: 7 kHz monopole source along z-axis at 333 mm, 93.2 dB peak

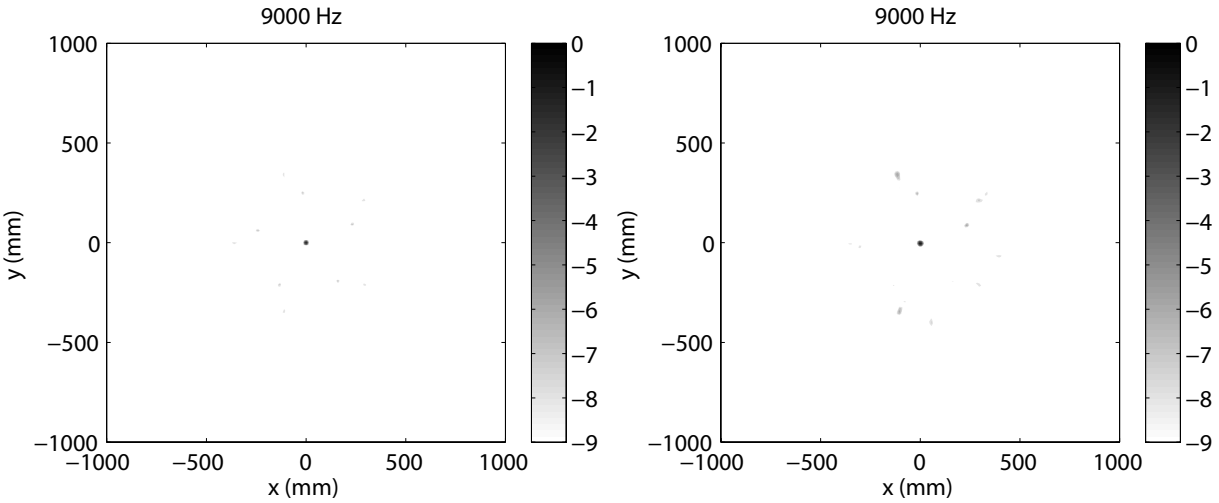

Figure 6.12: Theoretical (left) and measured (right) LSA response for Case 15: 9 kHz monopole source along z-axis at 333 mm, 93.9 dB peak

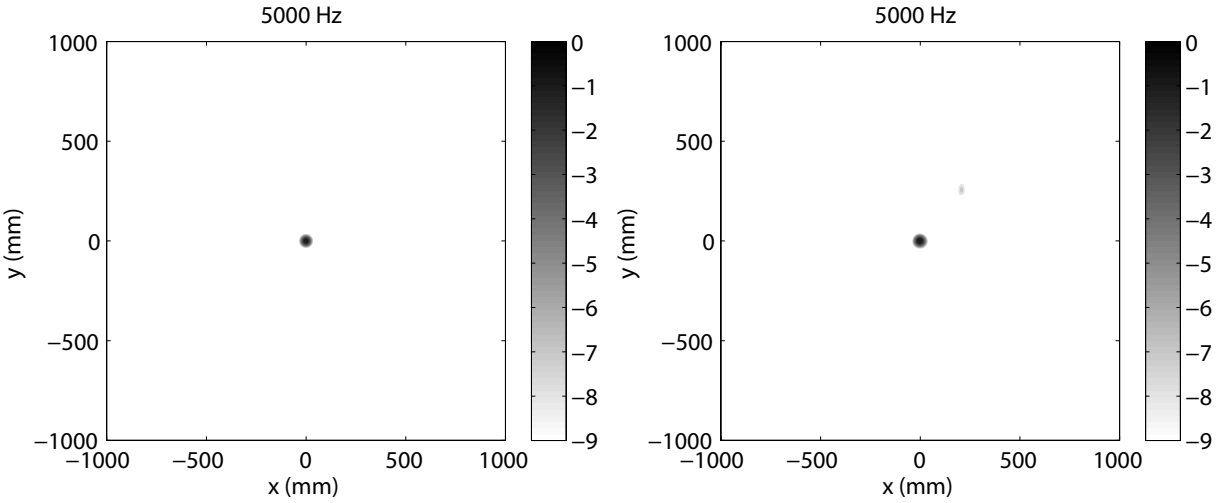

Figure 6.13: Theoretical (left) and measured (right) LSA response for Case 18: 5 kHz monopole source along z-axis at 500 mm, 89.5 dB peak

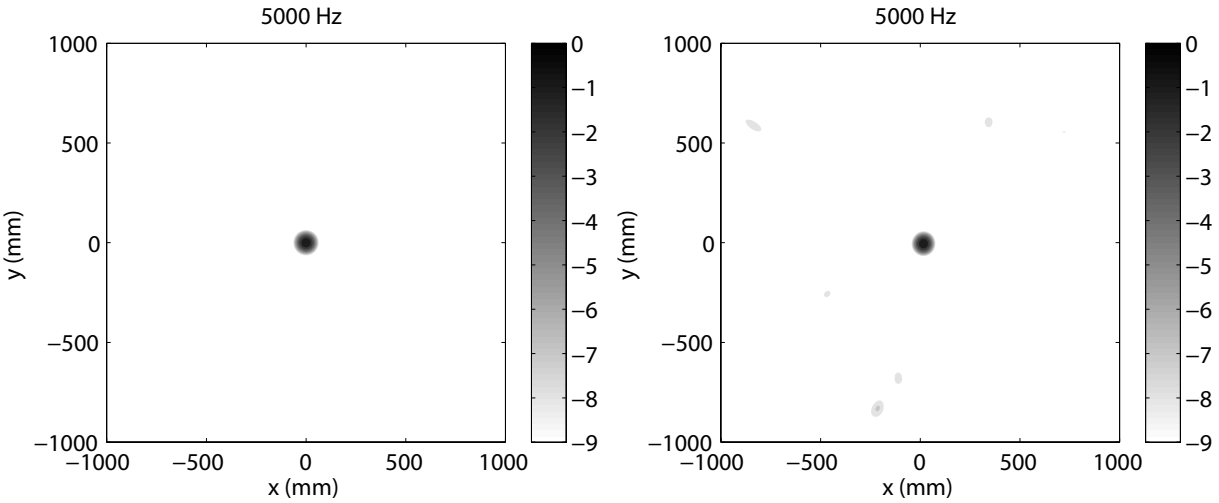

Figure 6.14: Theoretical (left) and measured (right) LSA response for Case 23: 5 kHz monopole source along z-axis at 1000 mm, 84.6 dB peak

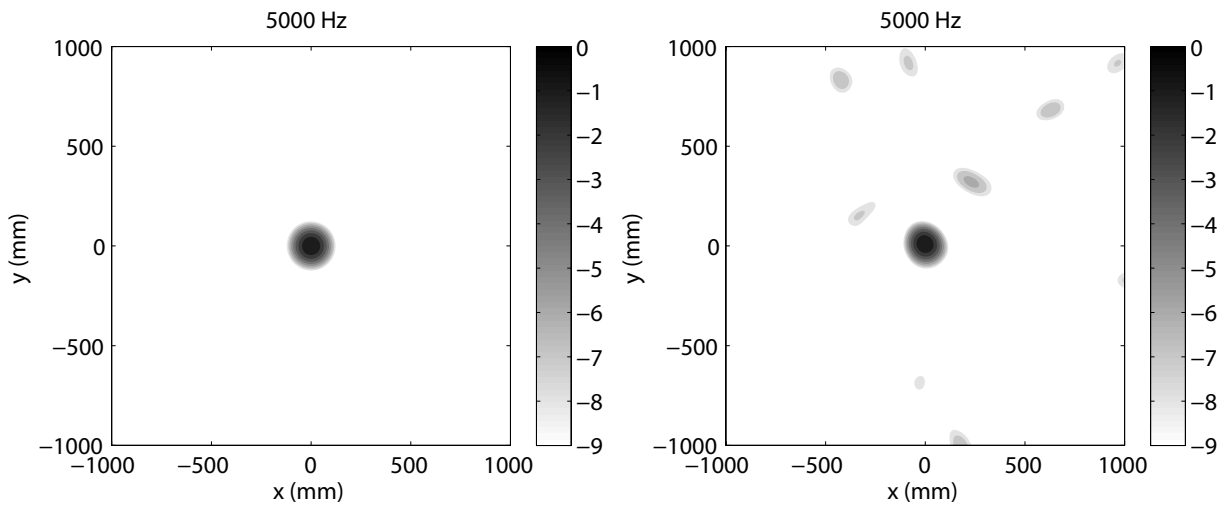

Figure 6.15: Theoretical (left) and measured (right) LSA response for Case 28: 5 kHz monopole source along z-axis at 2000 mm, 77.6 dB peak

In all cases the array is successful at spatially locating the single sound source at its physical location within experimental error. Noting the directional spreading of mainlobes and the presence of spurious sidelobes, it is apparent that the source maps become contaminated with reflections from the hard surfaces in the measuring environment, particularly at greater distances from the array, where the path from the source to the array allows for increased opportunity for reflection of an omnidirectional source such as a monopole. Spurious sidelobes are present primarily in the 1000 mm and 2000 mm test cases, and more prevalent at higher frequencies. Under the test conditions, the signal-to-noise ratio of the array is at least 9 dB at a distance of 333 mm and decreases to a worst case 6 dB at higher frequencies and greater distances when sidelobes become more prevalent. The implication of the sidelobes is that a second physical source could only be correctly identified if its sound pressure level differed by less than the difference between the mainlobe peak and sidelobe levels. Due to the finite number of microphones used in the array it is expected that the source maps will show sidelobes under certain conditions and nowhere is this more evident than in Case 14, where the sidelobes present in the theoretical and measured source maps appear at the same locations. However, Case 14 demonstrates the array's performance in close proximity to a source where the environment has less influence on the acoustic field measured by the array. This yields strong evidence that the sidelobes present in other cases, particularly those at 1000 mm and 2000 mm are indeed heavily influenced by reflections from various surfaces in the measurement environment and would be suppressed to a great extent in a treated environment. The increased presence of sidelobes in the measured source maps at higher frequencies such as 7 kHz and 9 kHz may also indicate that the incoming sound field is subject to diffraction around the perimeter of the

array as the wavelengths of the incoming sound source begin to match the distances from the outer microphones to the array's outer edges. Diffraction effects could be mitigated by enlarging the array frame while maintaining the current microphone positions, or by using the array as part of a larger planar surface, as it would be when flush-mounted in a closed-loop wind tunnel.

While the large-scale array's performance may appear inferior to that of the small-scale array based on visual impressions of the source maps, it is important to note that small-scale array testing was performed over a narrower frequency range and within 385 mm of the source where reflections from various surfaces in the environment have less influence on the transmission of sound waves. Under similar conditions, such as Cases 12-14, the large-scale array's source maps appear consistent with the theoretical maps and the beamwidths recorded by the large-scale array under similar conditions are nearly an order of magnitude smaller, indicating the large-scale array's resolution is far superior to that of the small-scale array, making it a much more useful apparatus across a wide range of applications.

The theoretical and measured -3 dB beamwidths obtained from testing the large-scale array in Cases 11–30 are shown in Figure 6.16.

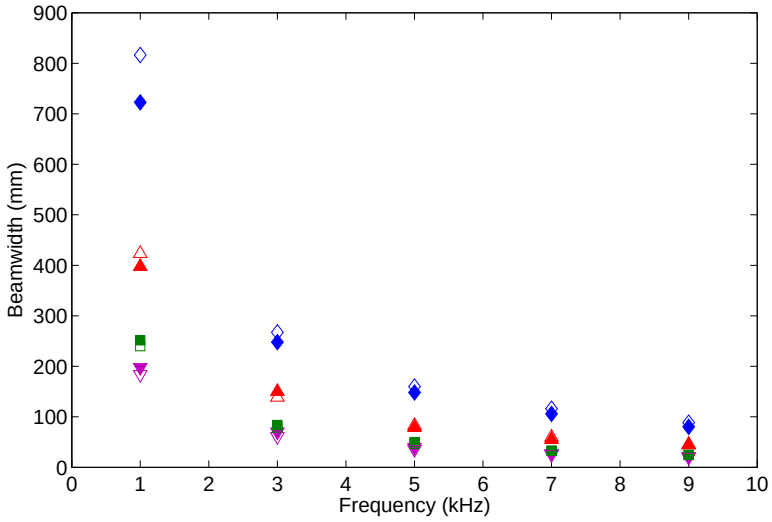

Figure 6.16: LSA beamwidth as a function of monopole source frequency ▽ Theoretical at 333 mm ▼ Measured at 333 mm □ Theoretical at 500 mm ■ Measured at 500 mm △ Theoretical at 1000 mm ▲ Measured at 1000 mm ◊ Theoretical at 2000 mm ♦ Measured at 2000 mm

Once again the beamwidth is noted to be inversely proportional to source frequency. The greatest discrepancies in beamwidth are encountered at the lower tested frequencies. The large-scale array offers considerable improvements over the small-scale array in terms

of resolution as evidenced by the magnitude of beamwidths in the experimental results. In wind tunnel testing, the array is intended to be placed within roughly 1000 mm of a source. The beamwidths measured under such a condition would range from 398 mm at 1 kHz to 44 mm at 9 kHz. The array could therefore uniquely identify acoustic sources emanating from multiple locations along an airfoil, provided the sound pressure levels of the various sources were within the dynamic range between mainlobe and highest sidelobe.

Plotting the beamwidths as a function of source distance in Figure 6.17 reveals that the beamwidths are proportional to source distance as expected.

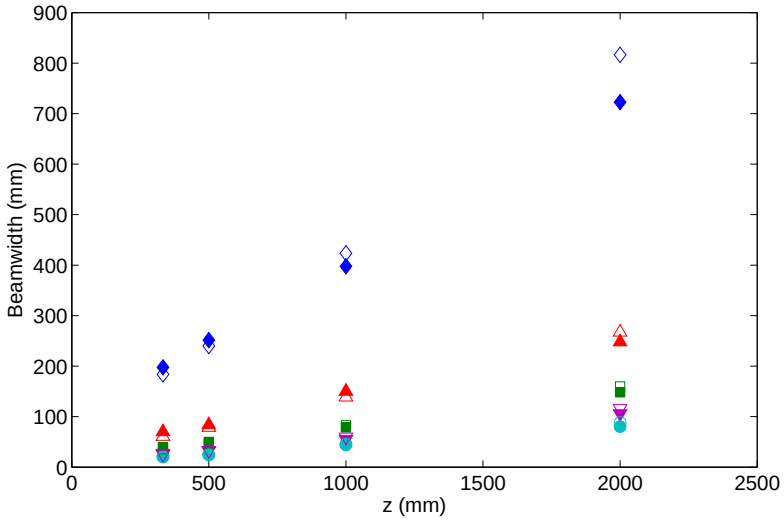

Figure 6.17: LSA beamwidth as a function of distance to monopole source ◊ Theoretical at 1 kHz ♦ Measured at 1 kHz△ Theoretical at 3 kHz ▲ Measured at 3 kHz □ Theoretical at 5 kHz ■ Measured at 5 kHz ▽ Theoretical at 7 kHz ▼ Measured at 7 kHz ○ Theoretical at 9 kHz ● Measured at 9 kHz

6.2.1 Error in Monopole Source SSA and LSA source maps

The source maps reveal artifacts of the acoustic environment which would not likely be present in measurements made in an acoustically treated facility. Therefore, comparisons of measured responses to theoretical responses are likely to contain greater error than would be encountered in measurements made in an anechoic chamber. However, the results shown do represent the array's ability to measure and locate sound sources in a typical measuring environment and provide examples of the types of artifacts expected to be encountered in practice. The following section deals with error in the measured responses of the known monopole sources by comparing the theoretical and measured source maps with respect to the previously established metrics: -3 dB beamwidth and root mean square error for the

entire source map.

In comparing experimental error in beamwidth for the small-scale array, shown in Figure 6.7, the error ranges from a minimum of 0.1%, at a distance of 164 mm and frequency of 4 kHz in Case 2, to a maximum of 7.8%, experienced at a distance of 385 mm and frequency of 6 kHz in Case 9. Beamwidths measured by the large-scale array show slightly greater error, particularly at the further distances tested, where the influence of the acoustic environment has greater influence, and also at lower frequencies. The error in beamwidth ranges from 0.6% at a distance of 500 mm and frequency of 9 kHz in Case 20 to 15.1% at a distance of 333 mm and frequency of 3 kHz in Case 12.

Root mean square error is used to quantify the error between the experimental and theoretical source maps. The root mean square error is tabulated from the relative error at each grid point in the experimental and theoretical source maps using Equation 2.32 and is shown in Table 6.1 and Table 6.2.

	3 kHz	4 kHz	5 kHz	6 kHz	7 kHz
164 mm	3.0	0.80	2.1	0.92	0.66
385 mm	7.6	1.3	2.1	1.1	0.47

Table 6.1: Root mean square error (%) in small-scale array measured responses

	1 kHz	3 kHz	5 kHz	7 kHz	9 kHz
333 mm	2.0	1.0	1.0	1.2	1.3
500 mm	2.7	1.3	1.1	1.3	1.1
1000 mm	6.3	1.9	2.0	2.3	2.3
2000 mm	6.8	5.1	3.7	3.4	4.0

Table 6.2: Root mean square error (%) in large-scale array measured responses

The root mean square error is apparently low because it represents the error averaged over the entire source map. While relative error between measured and theoretical source maps at a given spatial location can be as high as 100%, in the majority of source maps there are large portions where there is no difference in response, and consequently, these regions have the effect of lowering the overall error. Locations of mainlobes and sidelobes have much greater local error than the value calculated by the root mean square method. The root mean square error is generally observed to increase with increasing source distance and decreasing frequency. At greater distances or at lower frequencies the beamwidth is larger and the mainlobe therefore occupies a greater portion of the source map. Source maps with larger lobes lend themselves to higher root mean square error since the relative error between measured and theoretical source maps tends to be greatest around the perimeter of irregularly shaped lobes.

6.3 Large-Scale Array with Stationary Buzzer Sources

Source maps for Cases 31–33 using multiple piezo buzzer sources, as shown in Figure 5.3 and detailed in Table 5.3 are presented with the origin of the source map along the array's z-axis. The source maps contain a scanning area of 4 square metres with a 10 mm grid spacing. Computations are averaged over 20 blocks, each containing 8192 samples. Source maps are presented with reconstructed amplitudes with a dynamic range of 9 dB. Figure 6.18 shows two 4.4 kHz buzzers, 280 mm apart, emitting simultaneously at a distance of 1000 mm from the array.

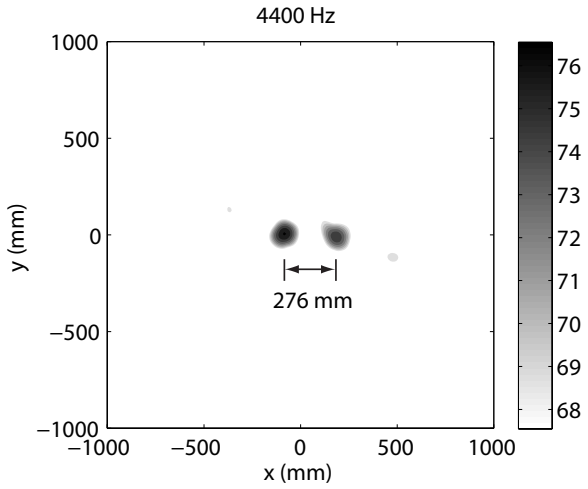

Figure 6.18: Case 31: Measured response to two 4.4 kHz buzzers with 280 mm separation at 1000 mm

The source maps reveal two well-defined mainlobes. During the experiment, the buzzers were matched within approximately 1 dB. This difference in sound pressure levels between the two mainlobes is consistent in the source map. The buzzers were located 280 mm apart, within approximately ±5 mm. The scaled distance between mainlobes in the source map is approximately 276 mm. Therefore the source map locates the two buzzers within experimental error. The effect of an increased distance between sources is demonstrated in Figure 6.19.

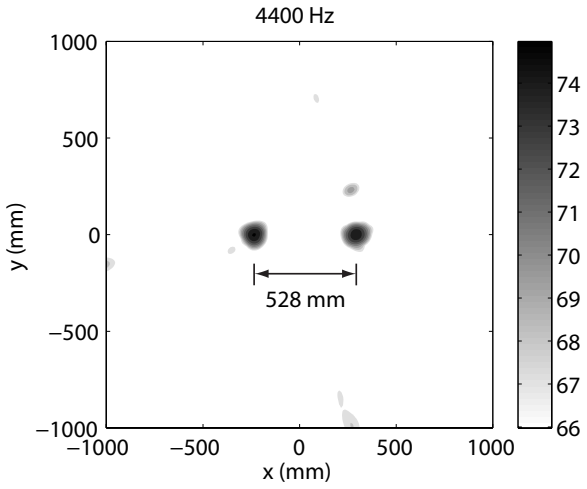

Figure 6.19: Case 32: Measured response to two 4.4 kHz buzzers with 530 mm separation at 1000 mm

The 4.4 kHz source sound pressure levels were again matched within 1 dB and this difference is adequately reconstructed in the source maps. The 530 mm distance between buzzers is measured as a scaled distance of 528 mm in the source map, which is within the expected margin of error. The source maps in Figure 6.20 shows the array's response to two sources at different frequencies. One 2.9 kHz source and one 4.4 kHz source matched within 1 dB and emitting simultaneously are represented by one-third octave band source maps with scan frequencies centred at each source frequency.

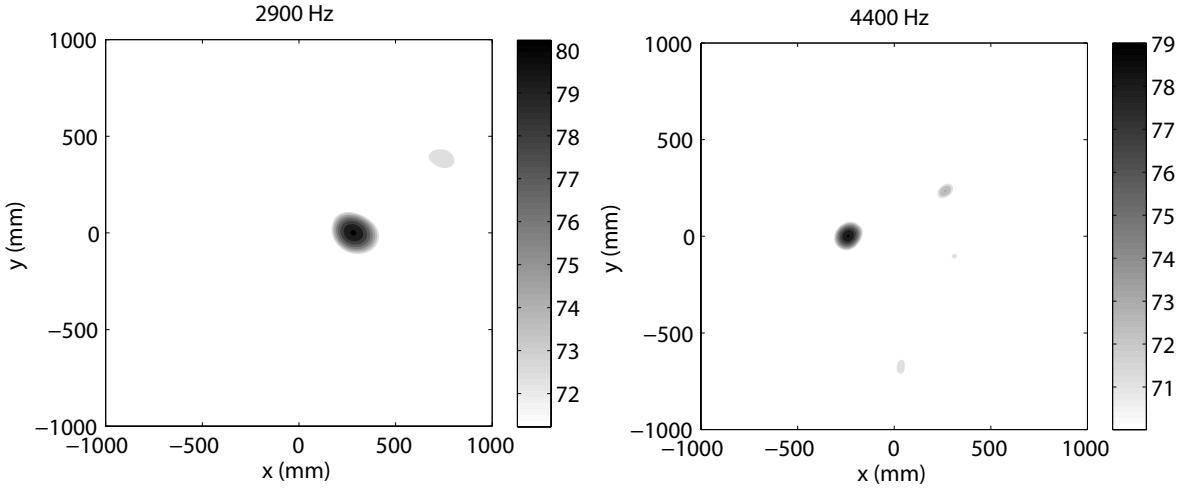

Figure 6.20: Case 33: Measured response to simultaneous 2.9 kHz (left) and 4.4 kHz (right) source with 53 cm separation at 1000 mm

The sources were separated by a physical distance of 530 mm ±5 mm. Although not shown, overlaying the two source maps allows the distance between mainlobes to be measured. The distance between mainlobes in the source map is 527 mm, within the expected margin of error. The beamwidth of the 2.9 kHz source is noticeably larger than the beamwidth of the 4.4 kHz source as expected. The source maps verify the array's ability to suppress acoustic contributions at frequencies other than the desired scan frequency. The sidelobes present in each source map are expected, since they are consistent with the sidelobes present in single source tests at similar frequencies at 1000 mm.

6.4 Large-Scale Array with Rotating Buzzer Source

The following discussion concerns the testing of a rotating buzzer source as shown in Figure 5.4. Beamforming was first attempted on the rotating buzzer source in the time domain using the refinements for moving sources with the purpose of dedopplerizing the time signals. While the dedopplerizing algorithm was completed, the computational requirements were beyond the capabilities of the available hardware for signals of reasonable length. It was noted that while the Doppler effect would cause the source frequency to change with respect to microphone position, even at high rotational rates the use of 1/3 octave bands would capture the source signal throughout its shifted range. Conventional frequency domain beamforming was therefore applied. A time-averaged source map is shown in Figure 6.21, obtained from frequency domain beamforming over 2 seconds. The scan area encompasses four square metres, with 10 mm grid spacing. The source map is centred along the array's z-axis. The black circle represents the trajectory taken by the buzzer during its rotation.

The source map reveals considerable spreading of the mainlobe. The circular motion of the buzzer is noted, with the greatest sound pressure levels encountered at the lower portions of the circle. The axis of rotation was located approximately 230 mm above the array centre, so the vertical offset in the buzzer trajectory is expected. It is also expected that the source amplitudes would be greater at azimuthal positions near the bottom of the arc, corresponding to a position with decreased average distance from the source to the microphones in the array.

To minimize the effects of source motion and source map mainlobe spreading, beamforming in the frequency domain was applied to shorter block lengths. In Figure 6.22, an example source map is overlaid on a still image of the rotating source captured over 0.033 seconds, to demonstrate the motion of the sound source in the source maps shown in this section.

Ten sequential source maps for Case 34, discussed in Table 5.4, are shown in Figures 6.23 to 6.27. Blocks containing 1667 samples were used, representing an elapsed time of 0.033 seconds.

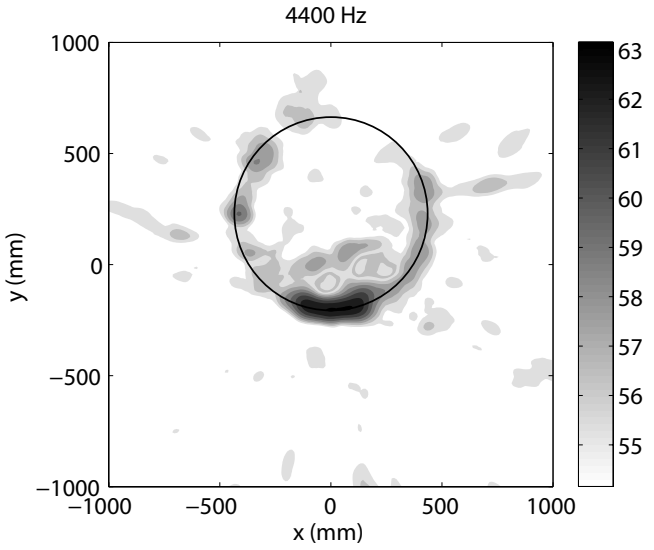

Figure 6.21: Time-averaged source map for buzzer source rotating at 170 rpm

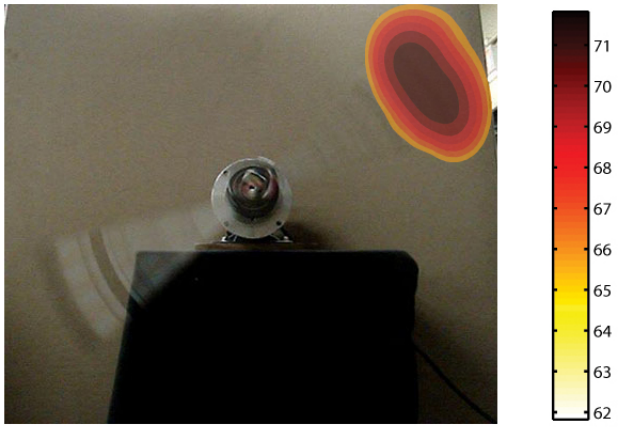

Figure 6.22: Example rotating buzzer source map overlaid over still image, both gathered over 0.033 s

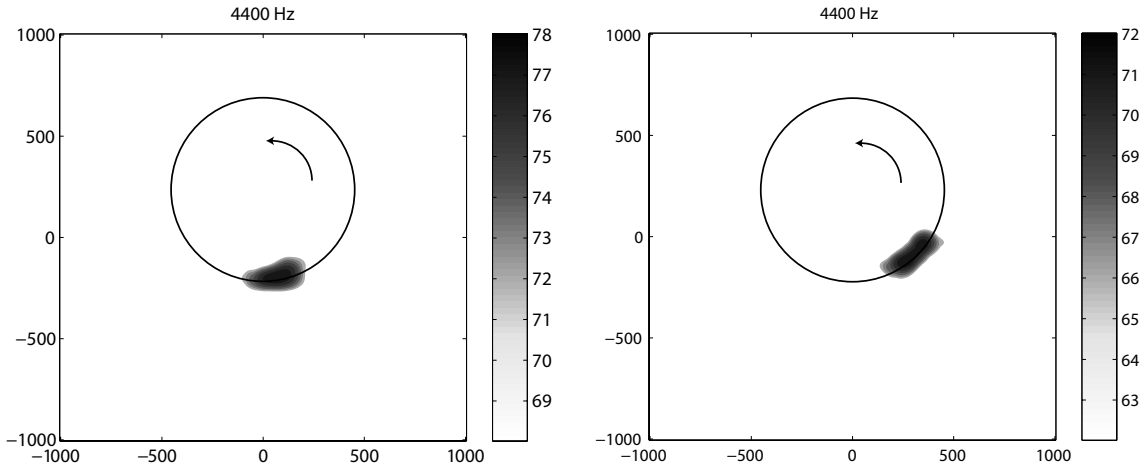

Figure 6.23: Case 34: Measured response for 4.4 kHz buzzer rotating at 170 rpm at 1000 mm, t = 0 s (left), t = 0.033 s (right)

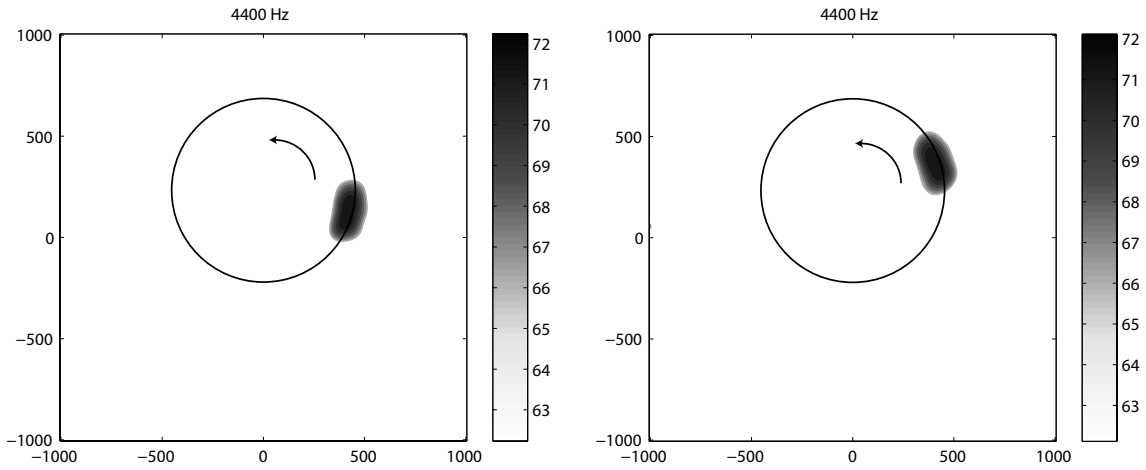

Figure 6.24: Case 34: Measured response for 4.4 kHz buzzer rotating at 170 rpm at 1000 mm, t = 0.067 s (left), t = 0.100 s (right)

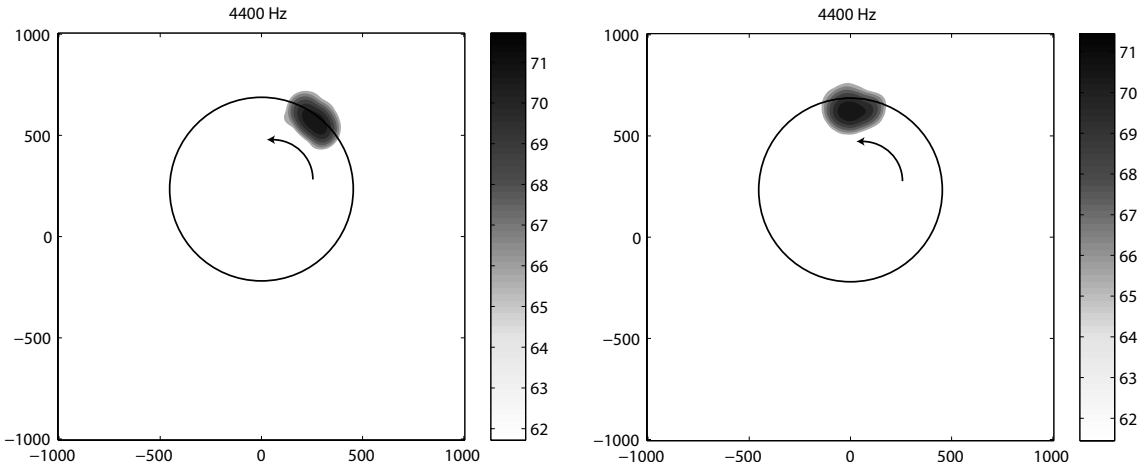

Figure 6.25: Case 34: Measured response for 4.4 kHz buzzer rotating at 170 rpm at 1000 mm, t = 0.133 s (left), 0.167 s (right)

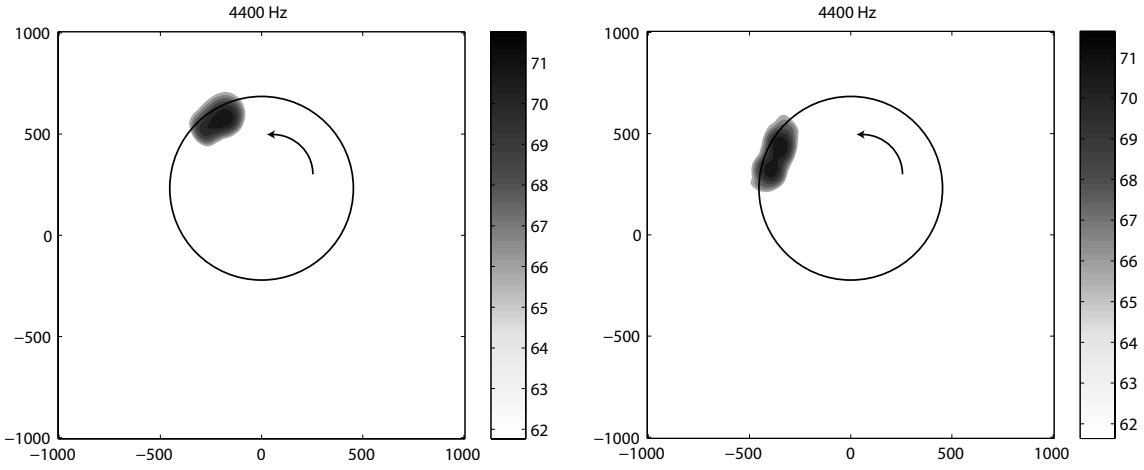

Figure 6.26: Case 34: Measured response for 4.4 kHz buzzer rotating at 170 rpm at 1000 mm, t = 0.200 s (left), t=0.233 s (right)

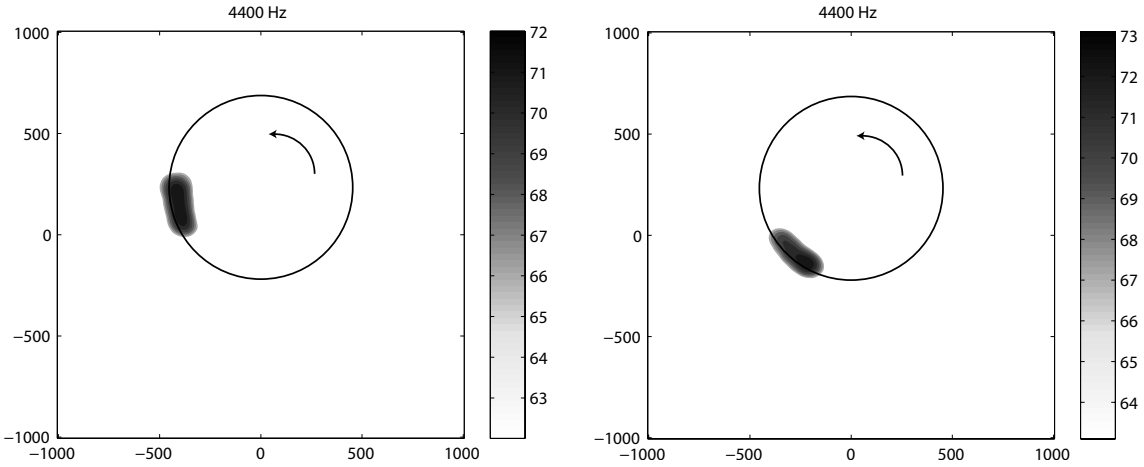

Figure 6.27: Case 34: Measured response for 4.4 kHz buzzer rotating at 170 rpm at 1000 mm, t = 0.267 s (left), 0.300 s (right)

It is apparent that the mainlobes in the source maps follow the spatial location of the source over one revolution. Referring to Figure 6.22, the spreading of the mainlobe over the 0.033 second averaging period is consistent with the movement of the source in that length of time. Since the centre of the rotor plane is above the centre of the array, the source increases in amplitude in its lower positions, as the distance between the source and each microphone decreases in these positions. The use of one-third octave bands adequately captures the change in frequency due to the Doppler shift. However, dedopplerizing the recorded time signals by accounting for the motion of the source would improve the ability to accurately locate the source and minimize mainlobe spreading. Based on the spreading of the mainlobes over the sampling period, it would be unfeasible to precisely locate noise emissions, such as distinguishing leading edge and trailing edge noise. Incorporating a computationally feasible algorithm capable of dedopplerizing the time signals is a worthwhile endeavour to improve the value of the experimental results. Significant improvements in the mainlobe spreading and source map accuracy would be gained by accounting for the motion of the source using the dedopplerization algorithm of Sijtsma [26].

6.5 Large-Scale Array Tests with Small Wind Turbine

Results and discussion of the acoustic tests of the 600 W turbine in the open-jet wind tunnel are presented below. The acoustic spectra are investigated over the range of flow speeds with comparisons to background levels. Source maps are presented for the 5.5 m/s freestream wind speed test cases for a range of source frequencies. A discussion of their

interpretation is provided. Finally, the probable generation mechanisms of aeroacoustic emissions are discussed.

6.5.1 Acoustic Spectra

Narrowband acoustic spectra obtained from a single MEMS microphone located near the centre of the large-scale array, during operation of the wind turbine in the open-jet facility described in Section 5.3.5, are shown in Figures 6.28 to 6.31. Background levels with the tunnel in operation and the turbine removed from the flow are included for comparison.

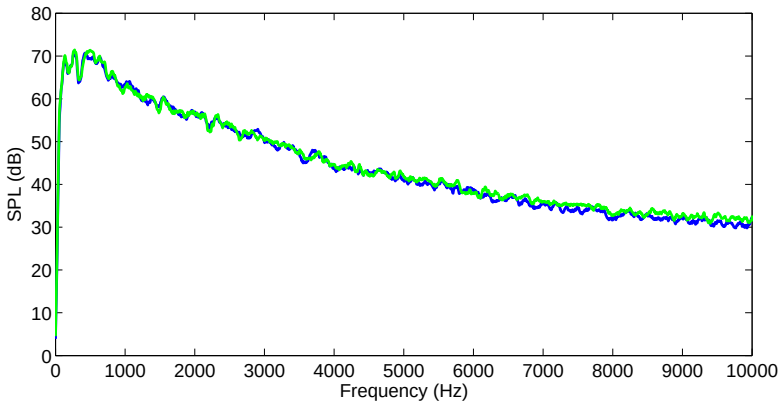

Figure 6.28: Acoustic spectra from single microphone during 2.5 m/s wind tunnel tests — Background noise — Turbine in flow

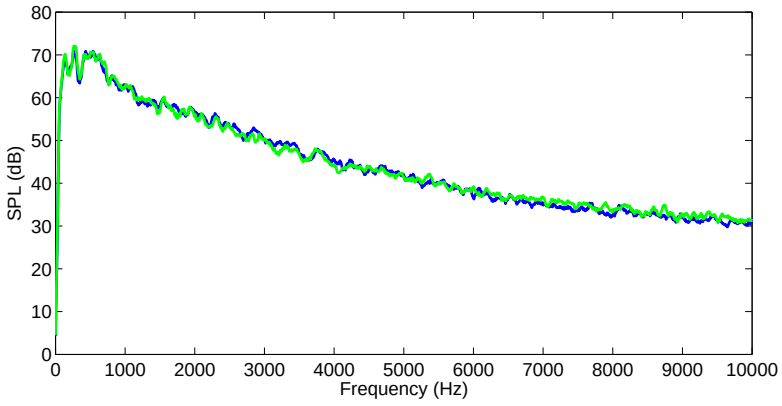

Figure 6.29: Acoustic spectra from single microphone during 3.5 m/s wind tunnel tests — Background noise — Turbine in flow

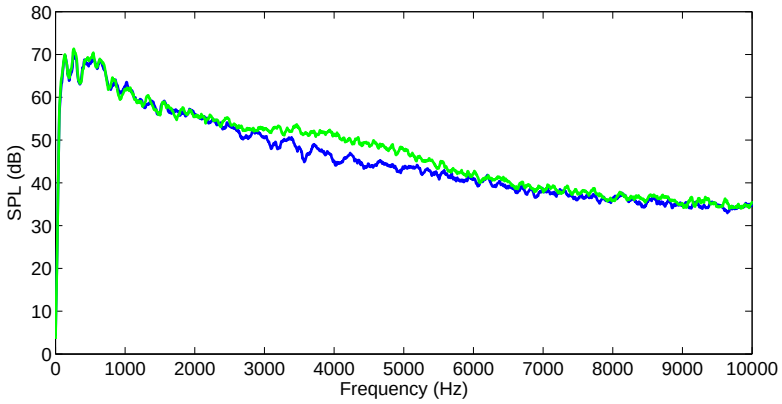

Figure 6.30: Acoustic spectra from single microphone during 4.5 m/s wind tunnel tests — Background noise — Turbine in flow

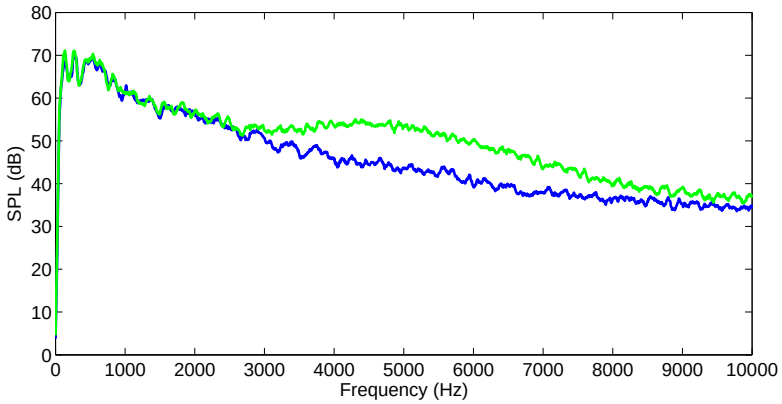

Figure 6.31: Acoustic spectra from single microphone during 5.5 m/s wind tunnel tests — Background noise — Turbine in flow

Figures 6.28 and 6.29 demonstrate that acoustic emissions produced by the turbine blades at freestream speeds of 2.5 and 3.5 m/s are not sufficient to overcome the background noise levels due to mechanical noise from the wind tunnel fan and tunnel-related acoustic emissions such as boundary layer noise at the test section outlet. It is evident from the spectra in Figure 6.30 that the acoustic contributions from the turbine at a freestream speed of 4.5 m/s, rotating at 550 rpm, are noticeably higher than background levels and reveal an increase in sound pressure level between roughly 3 and 6 kHz, with the greatest difference in sound pressure level being roughly 5 dB higher around 4 kHz. Similarly Figure 6.31 demonstrates that increasing the freestream speed to 5.5 m/s causes a significant increase in aeroacoustic emissions from the turbine rotating at 640 rpm. The acoustic

emissions from the turbine are considerable between roughly 3 kHz and 10 kHz, with the greatest difference noted as 10 to 12 dB between 4.5 and 6.5 kHz. The Doppler effect is undoubtedly contributing to the spreading of the peaks over a wide frequency due to the perceived change in frequency at each microphone due to the motion of the sound source emitted by the rotating turbine.

6.5.2 Time-Averaged Source Maps

Time-averaged source maps for the 5.5 m/s tests are shown in Figures 6.33 to 6.37 for one-third octave bands centred at 3 kHz, 4 kHz, 5 kHz, 6 kHz, and 7 kHz. The source maps contain a 4 square metre scanning area surrounding the turbine rotor plane, centred on the turbine hub, with 10 mm grid spacing. Frequency domain computations are based on 20 blocks of 8192 samples. Sound pressure levels are provided over a range of 9 dB. The black circles in Figures 6.33 to 6.37 represent the trajectory travelled by the blade tips as illustrated in Figure 6.32.

Figure 6.32: Representation of blade tip trajectory in wind turbine source maps

The effects of the shear layer between the freestream flow at the source and quiescent air at the array, and the convection of sound due to the freestream flow have not been included in the analysis of the microphone signals but are considered minor sources of error due to the low flow speeds and relatively short transmission distances. Based on the results obtained in tests of a rotating buzzer source, it is evident that using smaller sampling times in conventional frequency domain beamforming does not allow for precise localization of a rotating sound source, since the movement of the source over any reasonable sampling

length is too great to precisely capture in space. This is particularly true for the turbine blades which at 640 rpm are rotating approximately nearly four times as frequently as the buzzer source tested previously. For this reason, only time-averaged source maps collected over roughly 17.5 rotations are presented.

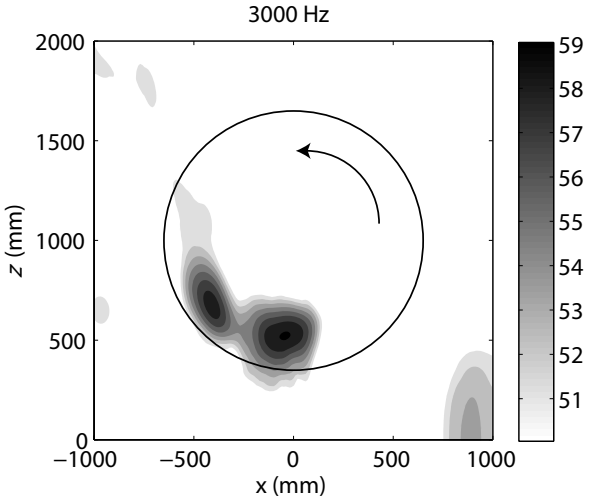

Figure 6.33: Time-averaged 3 kHz source map for counter-clockwise rotating wind turbine with 5.5 m/s freestream speed

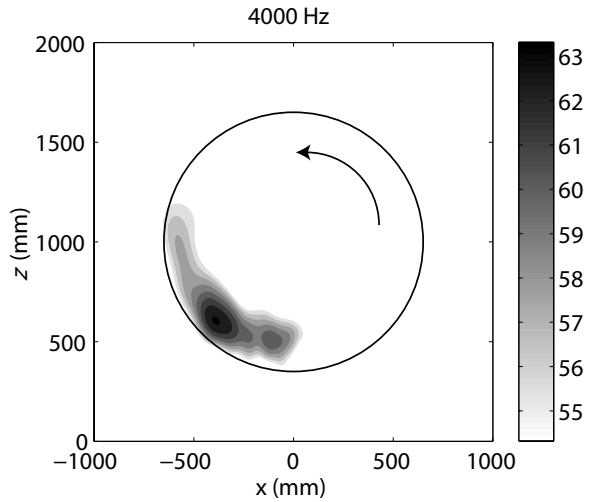

Figure 6.34: Time-averaged 4 kHz source map for counter-clockwise rotating wind turbine with 5.5 m/s freestream speed

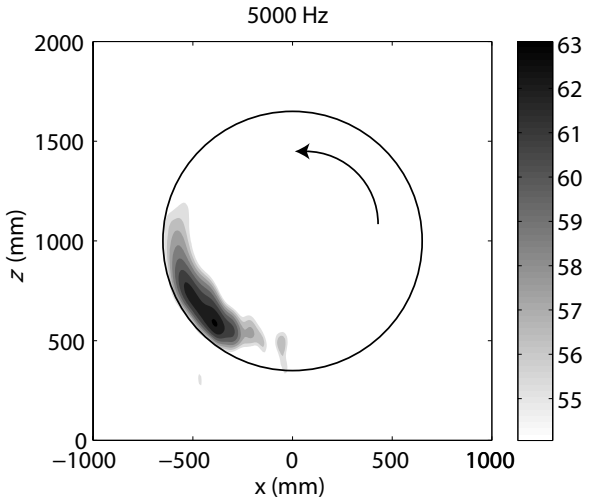

Figure 6.35: Time-averaged 5 kHz source map for counter-clockwise rotating wind turbine with 5.5 m/s freestream speed

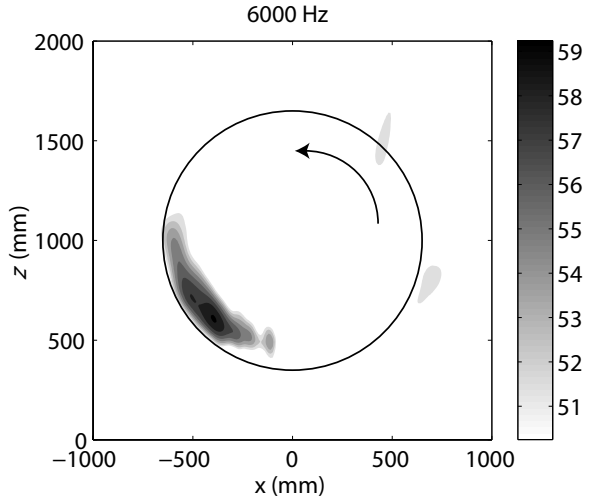

Figure 6.36: Time-averaged 6 kHz source map for counter-clockwise rotating wind turbine with 5.5 m/s freestream speed

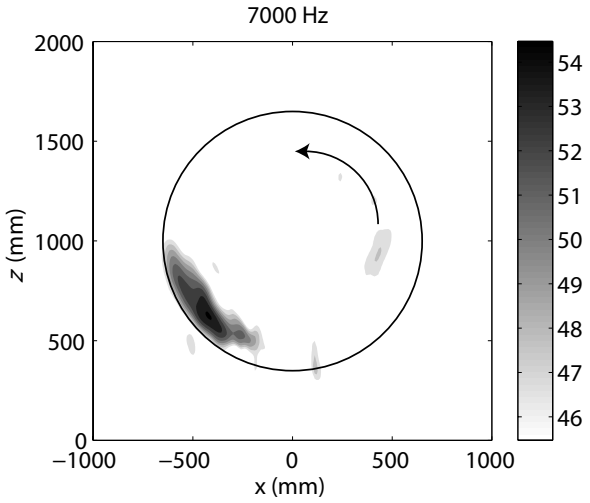

Figure 6.37: Time-averaged 7 kHz source map for counter-clockwise rotating wind turbine with 5.5 m/s freestream speed

Analyzing the time-averaged source maps reveals a wealth of information regarding the acoustic emissions of the 600 watt turbine. The sound pressure levels in the source maps represent time-averaged amplitudes and the mainlobes are spatially extended over the source maps because the turbine completed roughly 17.5 revolutions in the 1.64 second sampling time. The mainlobes are located in the lower left quadrant in all source maps. Mechanical noise is apparently not an issue and is not detected in the dynamic range presented, likely due to the minimal number of mechanical parts in the turbine's nacelle. Noting the direction of blade rotation in Figures 6.33 to 6.37, it is evident that the sound pressure levels measured below the turbine are at their highest as the blades travel downward toward the array. Comparing the left and right sides of the source maps reveals that the sound radiated downward from the blades during the downward rotation is at least 7 dB higher than the sound radiated downward by the blades during upward rotation. Thus, to an observer below the turbine, at the centre of the array, the maximum sound pressure levels are encountered three times per revolution, each time a downward travelling blade reaches an azimuth of roughly 120° to 130°. Since the tests were performed in an open-jet wind tunnel facility, a velocity gradient across the turbine rotor was not present, so the flow conditions at any position in the rotor should be virtually identical. Consequently, the emissions should be independent of blade azimuth and the asymmetry in the rotor plane noted in the source maps must be the result of factors other than flow.

Based on the analysis of similar time-averaged source maps from previous experiments of scale-model and full-scale turbines, the observed pattern of mainlobes in the source maps can be explained by dipole directivity and convective amplification [3, 41]. Applying the directivity function described in Equation 2.34 to this specific test setup, with a stationary

observer located at the centre of the array, yields a predicted source directivity pattern which is consistent with the experimentally obtained source maps. Figure 6.38 shows the expected directivity effects as a result of blade azimuth measured counterclockwise, in which 0° is referenced to an upward vertical position.

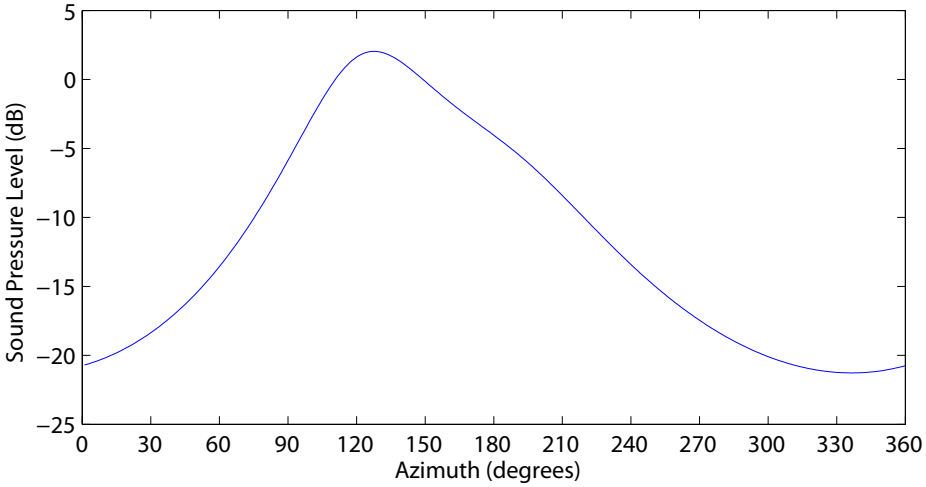

Figure 6.38: Effects of dipole directivity and convective amplification from one blade over one revolution

Dipole directivity has the greatest influence on the sound pressure levels over the range of azimuth angles, while convective amplification is most prevalent at an azimuth of roughly 120°. The location of the maximum due to convective amplification corresponds to the angular position at which the blade's linear velocity vector due to rotational motion is aligned with the source-observer line. Thus the sound emissions are momentarily directed at the array before being transmitted more efficiently to other locations due to the rotational motion of the blade. The effects of dipole directivity arise from the variation in radiation efficiency from a dipole source as the angle from the centre of the dipole source to the observer is changed as the blades rotate. Interpreting the effects of the high frequency directivity model as angular sectors of a circle, shown in Figure 6.39, reveals a relative sound pressure level pattern which matches the location of the mainlobes in the experimental source maps. An estimate of the radial location of sound emissions from the rotor is not included in this model so a portion of a sector at an inner radius will have the same apparent intensity as an outer radial position. An azimuth of approximately 128° is noted as being the expected location of the mainlobe from the rotating turbine according to the dipole directivity and convective amplification model. The theoretical difference between the maximum and minimum sound pressure level predicted by the directivity function in Equation 2.34 is approximately 23 dB, so it is not surprising that sound emissions are not evident in the experimental source maps during the upward portions of blade rotation.

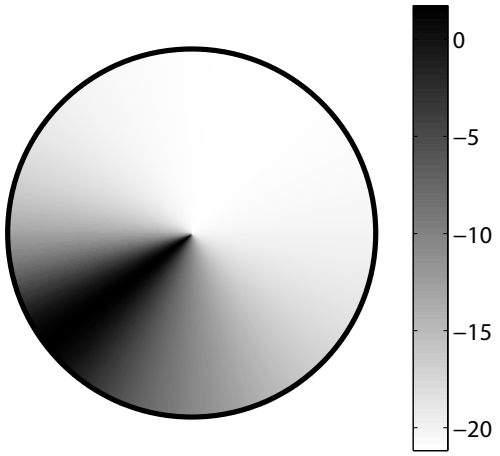

Figure 6.39: Expected relative sound pressure levels as a function of blade azimuth

Replacing the $sin^2(\theta/2)$ term by $sin^2\theta$ in Equation 2.34 to account for low frequency radiation for acoustic wavelengths approximately equal to the length of the blade chord, as mentioned in Section 2.4.2, leads to a maximum directivity function at 195°, which does not accurately represent the experimental results. Therefore the high frequency directivity function appears valid even for acoustic wavelengths greater than the blade tip chord. However, the spreading of the mainlobe in Figure 6.33, the 3 kHz source map, does reveal two mainlobes: one consistent with the position noted in the other source maps and one at roughly 175°, approaching the 195° maximum predicted by the low frequency directivity function. The second mainlobe may arise from a change in the dipole directivity as the acoustic wavelength at 3 kHz is greater than the chord. The low frequency directivity function does not predict two local maxima in sound pressure level over the rotation of a blade. Since the predicted maximum due to convective amplification for this case is still located at 120°, it is possible that the first mainlobe arises from the effects of convective amplification and the second mainlobe is due to the change in dipole directivity and the combination of the two effects is not adequately captured in the proposed low frequency model for this particular configuration. Sound reflections from the turbine stand may also explain the mainlobe at the 175° azimuth as the increased presence of sidelobes in this source map would suggest.

6.5.3 Assessment of Noise Generation Mechanisms

The main location of emissions is noted to be at the outer portion of the turbine rotor, consistent with the findings of previous wind tunnel and field tests [3, 40, 41]. The radial location of the mainlobe in the source maps moves from approximately 77% of the rotor diameter at 3 kHz to 87% of the rotor diameter at 7 kHz. The peak radial location

encountered between 5 and 7 kHz is approximately 5 to 8% more radially inward than in similar tests in that frequency range [3, 40, 41], which may be the result of differences in turbine blade geometry. The source maps alone do not provide sufficient information to determine the mechanisms of sound generation. Noting the similarity in the results with previous findings, it stands to reason that the mechanism of sound production can be compared with previous literature. In order to determine the likely sound production mechanism with the available data, it is necessary to consider the likelihood of all potential noise generation sources based on operating conditions and previous findings. The following noise sources are examined: tip noise, separation stall and deep stall, leading edge noise due to and in-flow turbulence, blunt trailing edge noise, laminar boundary layer vortex shedding, and turbulent boundary layer trailing edge noise.

Considering tip vortex noise, the mainlobes are located close to but not at the tip of the rotor, indicating that tip noise is not a dominant sound generation mechanism for this turbine. Furthermore, the location of the source is more radially inward than in the field tests of Oerlemans et al. where tip noise was dismissed as a significant contributor of sound emissions [3].

In regards to separation stall noise, it is unlikely that the blade is stalled at locations near the tip under these operating conditions since the turbine was freewheeling, or operating without generator load, and therefore able to rotate at a greater rate than intended. The increase in rotational rate increases the tangential velocity experienced by the blade, while maintaining a relatively low and constant freestream speed of 5.5 m/s, thereby decreasing the angle of attack. Furthermore, Cho et al. [40] found that operating in stalled conditions significantly increased the turbine emissions at low frequencies. In their experiments, considerable increases were noted at frequencies below 2 kHz, and the location of emissions at other frequencies moved radially inward [40]. Comparing the 5.5 m/s spectra to lower speeds and to background noise shows no indication of an increase in sound pressure levels at low frequencies. Separation-stall is therefore not considered a significant source of sound production in these tests. Deep stall can be ruled out by the same reasoning.

Based on the source maps alone, it is not possible to distinguish between leading edge and trailing edge noise sources. Leading edge noise could be present as a contributing noise source, arising from in-flow turbulence interacting with the leading edge of the turbine airfoils. To assess the likelihood of leading edge noise, the high frequency dipole directivity function can be considered, realizing that the dipole directivity dependence will be inverted, as discussed in Section 2.4.2. Based on the inverted directivity dependence, the maximum sound pressure level is expected to occur at an azimuth of approximately 234°, which is clearly not observed in the experimental source maps. Based on this analysis it is suggested that leading edge noise is not a concern for this turbine under these operating conditions.

Blunt trailing edge noise becomes an issue when the trailing edge thickness is 20% greater than boundary layer displacement thickness. Because the airfoil geometries for

this turbine are unknown and the twist and chord vary along the length, estimates or measurements of the boundary layer thickness cannot be easily obtained from literature or testing. However, since the blades have a very thin trailing edge, blunt trailing edge vortex shedding is not likely the cause.

The Reynolds number in the 5.5 m/s in the test cases presented here ranges from roughly 50 000 at the root of the blade to 130 000 near the tip. In this regime, laminar boundary layer vortex shedding is commonly expected. For a static two-dimensional airfoil, vortex shedding appears in a spectrum as a peak with a certain bandwidth. The spectral results shown in Figures 6.30 and 6.31 indicate a fairly narrow range of frequencies at which the turbine produces audible noise. The shape of the spectral peaks is consistent with other experiments concerning laminar boundary layer vortex shedding from airfoils [49,50]. While noise arising from vortex shedding is expected to appear as a sharp peak in a spectrum, the apparent width of the rounded spectral peaks in Figures 6.30 and 6.31 could arise from a number of factors: varying velocities, chord lengths, and angles of attack along the blade which would contribute to vortex shedding across a wide range of frequencies; shifting of the peak frequencies due to the Doppler effect; and incoherence of the vortex street. Based on the flow regime and spectral results, it is likely that laminar boundary layer vortex shedding is the primary mechanism of generation. Turbulent boundary layer trailing edge noise is a broadband noise source identified as a prominent contributor to noise emissions from commercial turbines, with operating Reynolds numbers greater than one million. It is also possible that turbulent boundary layer trailing edge noise is a contributing factor to the experimentally measured noise emissions to some extent, resulting in a broadening of the spectral peaks. It is likely that along portions of the blade, the flow transitioned to turbulence prior to the trailing edge due to the increase in Reynolds number near the tip or due to turbulence present in the jet of air emitted from the wind tunnel.

Assuming trailing edge noise to be the primary mechanism of acoustic emissions, the location of the mainlobe is expected to move radially outward with increasing frequency. For laminar boundary layer vortex shedding, the shedding frequency is proportional to velocity and inversely proportional to chord length and for turbulent boundary layer trailing edge noise, the frequency of emissions is proportional to the boundary layer thickness. By design, the blade chord decreases at greater radial positions and the relative flow speed over the airfoil increases, so the laminar boundary layer shedding frequency should increase at greater radial positions. Furthermore, emissions resulting from turbulent boundary layer trailing edge noise would be expected to move radially outward due to the decrease in boundary layer thickness accompanying the decreasing chord and increasing velocity of the turbine blade. Based on the above observations, it is suggested that trailing edge noise is the dominant sound generation mechanism for the 600 watt turbine under the conditions tested. While it was not tested, it would be expected that the sound levels produced from this turbine could be reduced by tripping the boundary layer.

Chapter 7

Conclusions and Recommendations

7.1 Conclusions

Aeroacoustic emissions were identified as a notable concern for wind turbines. Based on a review of literature, microphone arrays were selected as a research technique for the investigation and localization of aeroacoustic sources. A systematic search of low-cost microphones was undertaken, with microelectromechanical microphones ultimately selected based on their cost, specifications, electrical simplicity, and prior use in a limited number of microphone arrays. A small-scale array with dimensions 152.4 mm by 203.2 mm, using bottom-ported Knowles Acoustics SPM0408LE5H microphones, was designed for use in a small, non-anechoic, closed-loop wind tunnel to improve the signal-to-noise ratio of aeroacoustic measurements of wind turbine airfoils. A large-scale array with dimensions roughly 1 m by 1 m, using top-ported Knowles Acoustics SPM0408HE5H microphones was designed as a portable measurement apparatus capable of locating noise sources from small rotating wind turbines in conjunction with open-jet wind tunnels or field measurements. Printed circuit boards for microphone connections and array structure were designed, sent out for production, and populated in-house using a custom reflow oven. A large mounting frame was constructed for the large-scale array and connectors were assembled. Beamforming algorithms were implemented to allow simulation of sound sources and conditions expected to be encountered in testing.

Calibration of the microphones presented various challenges and ultimately, a plane wave tube calibration method was implemented over a relatively narrow frequency range. A combination of simultaneous and substitution methods were used to characterize the microphones in terms of amplitude response, frequency response, and 1 kHz sensitivity. Microphone phase was also tested on the completed arrays in response to a known source at a known position.

A number of experiments were devised to validate array performance and applicability to a rotating wind turbine. The testing of both small-scale and large-scale arrays was

performed using a known monopole source at a number of frequencies and distances. The mainlobe locations in the source maps were within the margin of error of the physical positioning of the sound source. Experimental beamwidths showed the expected behaviour with increasing distance and frequencies. Beamwidth measurements were compared for experimental and theoretical responses to a monopole source and were found to range from 0.1% to 7.8% for the small-scale array and 0.6% to 15.1% for the large-scale array. Spurious sidelobes were present, particularly at distances greater than 1 m and at higher frequencies. Relative error between experimental results and theoretical predictions was tabulated as root mean square error over the source map and found to range from 0.47% to 7.5% for the small-scale array and 1.0% to 6.8% for the large-scale array. The error was largely attributed to reflections in the non-anechoic measuring environment and diffraction of sound waves around the array edges at higher frequencies. Preliminary tests of the small-scale array in the small, closed-loop wind tunnel revealed its high susceptibility to boundary layer noise.

Testing the large-scale array in response to multiple sources revealed that the distance between mainlobes in the source map was well within the margin of error in positioning the sound sources for two separation distances. Similarly, multiple sources at different frequencies were resolved independently, verifying the array's ability to suppress frequencies other than those of interest. Dedopplerization algorithms were unsuccessfully implemented due to hardware limitations. A rotating sound source was located spatially and tracked over one full revolution using conventional beamforming over 0.033 second lengths of time. Source maps demonstrated considerable mainlobe spreading which made source localization ineffective.

Experimental results from the acoustic testing of a 1.3 metre rotor diameter, 600 watt turbine in an open-jet wind tunnel indicated strong evidence of trailing edge noise at freestream speeds of 4.5 m/s and 5.5 m/s. Speeds of 2.5 m/s and 3.5 m/s were insufficient to produce acoustic emissions able to overcome the background noise levels. Acoustic spectra from the 4.5 m/s tests indicated acoustic contributions in a frequency range from approximately 3 to 6 kHz with a maximum increase of approximately 5 dB at 4 kHz. Spectral results from the 5.5 m/s tests revealed acoustic emissions from the turbine from approximately 3 to 10 kHz with the greatest increase over background levels being 10 to 12 dB higher between 4.5 and 6.5 kHz. Source maps for the 5.5 m/s tests reveal that the turbine's aeroacoustic emissions are most prevalent at the outer portions of the radius, but not necessarily at the tip. The azimuthal location of the greatest sound pressure levels was found to be roughly 120° to 130°, measured from the upward vertical, for most test conditions. An analytical model based on dipole directivity and convective amplification confirmed this sector to be the approximate expected azimuthal location of the source in the time-averaged source maps.

7.2 Recommendations

Having demonstrated the capabilities of both arrays in response to known sound sources, and having shown the large scale array's ability to localize aeroacoustic sources from a rotating wind turbine, it is evident that the measurement equipment can be readily applied in numerous applications. It would be a worthwhile study to determine the effect of tripping the boundary layer of the 600 W turbine. This could be accomplished by applying various treatments to the leading edge of the blade, including a commercial leading edge tape product or similar grit strip. The large-scale array in particular can be incorporated into numerous experimental applications. An obvious extension of this work is to investigate the sound production mechanisms from small-scale wind turbines operating in the field. Since the large-scale array is likely too small to be of value in acoustic tests of a full-scale wind turbine, an array on the order of tens of metres would be required. Another suitable application for the large-scale array is to identify and distinguish trailing edge noise mechanisms in two-dimensional airfoil tests in the open-jet wind tunnel.

However, prior to further investigations, there a number of advancements which could be made to the beamforming processing software. Simplifications in the processing of results have left significant room for improvement, such as incorporating into the beamforming analysis the discrepancies in sound transmission due to the shear layer in the open-jet wind tunnel facility, the influence of convection of sound due to flow, and the effect of dedopplerizing the pressure signals.

The difficulties encountered in calibration present the requirement for an anechoic chamber for precise calibration of microphones. In order to obtain frequency response and phase calibrations over a wide range, access to an anechoic chamber would be necessary. The change in frequency response due to the addition of an acoustic resistance is worthy of future consideration, as the deviations in measured and expected frequency response may be reduced by covering the microphone ports with an acoustic vent.

The small-scale array shows promise in its ability to localize sources but is currently limited in its wind tunnel applicability due to amplifier saturation from high levels of background noise in a flush-mounted configuration. Two methods of increasing array performance in the small wind tunnel would be to attempt to recess the small-scale array behind an acoustically permeable wall and to reduce the gain of the microphone preamplifiers to increase the available headroom.

References

[1] *Ontario Regulation 359/09*, 2009. 1

[2] Wagner, S., R. Bareiss and G. Guidati, *Wind Turbine Noise*. Springer-Verlag, New York, NY, 1996. 2

[3] Oerlemans, S., P. Sijtsma and B. Méndez López, *Location and quantification of noise sources on a wind turbine*. Journal of Sound and Vibration, 299(4-5):869–883, February 2007. 2, 18, 26, 27, 29, 30, 31, 32, 99, 101, 102

[4] Soderman, P. T. and C. S. Allen, *Aeroacoustic Measurements*, chap. Microphone Measurements In and Out of Airstream, 1–61. Springer, Berlin, 2002. 2, 33, 34

[5] Sperandi, B., *The application of particle image velocimetry in a small scale wind tunnel*. Master's thesis, University of Waterloo, Waterloo, Ontario, CA, 2002. 2

[6] Raichel, D. R., *The Science and Applications of Acoustics, Second Edition*. Springer-Verlag, New York, NY, second ed., 2006. 4, 5, 39, 53, 54

[7] Fox, R. W., A. T. McDonald and P. J. Pritchard, *Introduction to Fluid Mechanics*. John Wiley & Sons, Inc., Hoboken, NJ, 6th ed., 2006. 5

[8] Howe, M. S., *Acoustics of Fluid-Structure Interactions*. Cambridge University Press, New York, NY, 1998. 6

[9] Underbrink, J. R., *Aeroacoustic Measurements*, chap. Aeroacoustic Phased Array Testing in Low Speed Wind Tunnels. Springer, Berlin, 2002. 7, 21, 23, 24, 41

[10] Johnson, D. H. and D. E. Dudgeon, *Array Signal Processing: Concepts and Techniques*. Prentice-Hall, Englewood Cliffs, NJ, 1993. 8, 9, 20

[11] Oerlemans, S., *Detection of aeroacoustic sound sources on aircraft and wind turbines*. Ph.D. thesis, University of Twente, Enschede, The Netherlands, 2009. 10, 14, 16

[12] Brooks, T. F. and W. M. Humphreys Jr, *Effect of Directional Array Size On The Measurement of Airframe Noise Components*. In *5th AIAA/CEAS Aeroacoustics Conference*, AIAA-99-1958, 1999. 10

[13] Oerlemans, S. and P. Sijtsma, *Determination of Absolute Levels from Phased Array Measurements Using Spatial Source Coherence*. In *8th AIAA/CEAS Aeroacoustics Conference*, AIAA-2002-2464, Breckenridge, CO, June 2002. 10

[14] Sarradj, E., *A fast signal subspace approach for the determination of absolute levels from phased microphone array measurements*. Journal of Sound and Vibration, 329(9):1553–1569, April 2010. 10

[15] Humphreys Jr, W. M., T. F. Brooks, W. W. Hunter Jr and K. R. Meadows, *Design and Use of Microphone Directional Arrays for Aeroacoustic Measurements*. In *36th AIAA Aerospace Sciences Meeting*, AIAA-98-0471, Reno, NV, January 1998. 11, 12

[16] Gough, C., *Springer Handbook of Acoustics*, chap. Musical Acoustics. Springer, New York, NY, 2007. 11

[17] Orlando, S. M., *Laser Doppler Anemometry and Acoustic Measurements of a S822 Airfoil at Low Reynolds Numbers*. Master's thesis, University of Waterloo, 2011. 13, 66

[18] Brooks, T. F. and W. M. Humphreys Jr, *A Deconvolution Approach for the Mapping of Acoustic Sources (DAMAS) Determined from Phased Microphone Arrays*. Journal of Sound and Vibration, 294:856–879, 2006. 13, 14

[19] Oerlemans, S., L. Broersma and P. Sijtsma, *Quantification of airframe noise using microphone arrays in open and closed wind tunnels*. International Journal of Aeroacoustics, 6:309–333, 2007. 13, 18

[20] Amiet, R. K., *Refraction of Sound by a Shear Layer*. Journal of Sound and Vibration, 58 (3):467–482, Sept. 1978. 14

[21] Dougherty, R. P., *Extensions of DAMAS and Benefits and Limitations of Deconvolution in Beamforming*. In *11th AIAA/CEAS Aeroacoustics Conference*, AIAA-2005-2961, May 2005. 14

[22] Ehrenfried, K. and L. Koop, *Comparison of Iterative Deconvolution Algorithms for the Mapping of Acoustic Sources*. AIAA Journal, 45(7):1584–1595, July 2007. 14

[23] Sijtsma, P., *CLEAN Based on Spatial Source Coherence*. International Journal of Aeroacoustics, 6(4):357–374, December 2007. 14

[24] Ravetta, P., R. Burdisso and W. F. Ng, *Noise Source Localization and Optimization of Phased-Array Results*. AIAA Journal, 47(11):2520–2533, November 2009. 14

[25] Dougherty, R. P. and G. G. Podboy, *Improved Phased Array Imaging of a Model Jet*. In *15th AIAA/CEAS Aeroacoustics Conference*, AIAA-2009-3186, Miami, FL, May 2009. 14, 18

[26] Sijtsma, P., S. Oerlemans and H. H., *Location of rotating sources by phased array measurements*. In *7th AIAA/CEAS Aeroacoustics Conference*, AIAA-2001-2167, Maastricht, NL, May 2001. 16, 93

[27] Oerlemans, S. and P. Sijtsma, *Effect of Wind Tunnel Side-Plates on Airframe Noise Measurements with Phased Arrays*. In *6th AIAA/CEAS Aeroacoustics Conference*, AIAA-20000-1938, Lahaina, HI, June 2000. 18

[28] Soderman, P. T., F. Kafyeke, J. Boudreau, N. J. Burnside, S. M. Jaeger and R. Chandrasekharan, *Airframe noise study of a Bombardier CRJ-700 aircraft model in the NASA Ames 7- by 10-foot wind tunnel*. International Journal of Aeroacoustics, 3(1):1–42, 2004. 18

[29] Remillieux, M. C., H. E. Camargo, P. A. Ravetta, R. A. Burdisso and W. F. Ng, *Novel Kevlar-Walled Wind Tunnel for Aeroacoustic Testing of a Landing Gear*. AIAA Journal, 46(7):1631–1639, July 2008. 18, 33, 67

[30] Mendoza, J. M., D. K. Nance and K. K. Ahuja, *Source Separation from Multiple Microphone Measurements in the Far Field of a Full Scale Aero Engine*. In *14th AIAA/CEAS Aeroacoustics Conference*, AIAA-2008-2809, Vancouver, BC, May 2008. 18

[31] Hutcheson, F. V. and T. F. Brooks, *Measurement of Trailing Edge Noise Using Directional Array and Coherent Output Power Methods*. In *8th AIAA/CEAS Aeroacoustics Conference*, AIAA-2002-2472, Breckenridge, CO, June 2002. 18

[32] Mendoza, J., T. F. Brooks and W. M. Humphreys, *Aeroacoustic Measurements of a High-Lift Wing/Slat Model*. In *8th AIAA/CEAS Aeroacoustics Conference*, AIAA-2002-2604, Breckenridge, CO, June 2002. 18

[33] Hutcheson, F. V. and T. F. Brooks, *Effects of Angle of Attack and Velocity on Trailing Edge Noise*. In *42nd AIAA Aerospace Sciences Meeting*, AIAA-2004-1031, Reno, NV, January 2004. 18, 31

[34] Sarradj, E. and T. Geyer, *Noise Generation by Porous Airfoils*. In *13th AIAA/CEAS Aeroacoustics Conference*, AIAA-2007-3719, Rome, IT, May 2007. 18

[35] Shannon, D. and S. C. Morris, *Trailing edge noise measurements using a large aperture phased array*. International Journal of Aeroacoustics, 7(2):147–176, 2008. 18

[36] Choudhari, M. M., D. P. Lockard, M. G. Macaraeg, B. A. Singer, C. L. Streett, G. R. Neubert, R. W. Stoker, J. R. Underbrink, M. E. Berkman, M. R. Khorrami and S. S. Sadowski, *Aeroacoustic Experiments in the Langley Low-Turbulence Pressure Tunnel*. NASA-TM-2002-211432, 2002. 18

[37] Khorrami, M. R., M. E. Berkman and M. Choudhari, *Unsteady Flow Computations of a Slat with a Blunt Trailing Edge*. AIAA Journal, 38(11):2050–2058, November 2000. 18

[38] Jacob, M. C., G. Robert, N. Fremion and S. Guerrand, *In-flow acoustic measurements on high speed trains*. In *6th AIAA/CEAS Aeroacoustics Conference*, AIAA-2000-2011, Lahaina, HI, June 2000. 18

[39] Marcolini, M. A. and T. F. Brooks, *Rotor Noise Measurement Using a Directional Microphone Array*. Journal of the American Helicopter Society, 37(11):11–22, 1992. 18

[40] Cho, T., C. Kim and D. Lee, *Acoustic measurement for 12% scaled model of NREL Phase VI wind turbine by using beamforming*. Current Applied Physics, 10(2):S320–S325, March 2010. 18, 30, 101, 102

[41] Oerlemans, S., J. G. Schepers, G. Guidati and Wagner, *Experimental demonstration of wind turbine noise reduction through optimized airfoil shape and trailing-edge serrations*. In *European Wind Energy Conference*, Copenhagen, DK, 2001. 18, 30, 99, 101, 102

[42] Michel, U., J. Helbig, B. Barsikow and M. Hellmig, *Flyover noise measurements on landing aircraft with a microphone array*. In *4th AIAA/CEAS Aeroacoustics Conference*, AIAA-98-2336, Toulouse, FR, June 1998. 18

[43] Siller, H., U. Michel, C. Zwiener and G. Saueressig, *Reduction of Approach Noise of the MD-11*. In *12th AIAA/CEAS Aeroacoustics Conference*, AIAA-2006-2464, Cambridge, MA, May 2006. 18

[44] Oerlemans, S., M. Fisher, T. Maeder and K. Kögler, *Reduction of Wind Turbine Noise using Optimized Airfoils and Trailing-Edge Serrations*. AIAA Journal, 47(6):1470–1481, 2009. 18

[45] Finch, R. D., *Introduction to Acoustics*. Pearson Education, Inc., Upper Saddle River, NJ, 2005. 21

[46] Steinberg, B. D., *Principles of Aperture and Array System Design*. Wiley-Interscience, New York, NY, 1976. 22

[47] Dougherty, R. P., *Spiral-shaped array for broadband imaging*. US Patent No. 5,838,284, 1998. 23, 24

[48] Underbrink, J. R., *Circularly symmetric, zero redundancy, planar array having broad frequency range applications*. US Patent No. 6,205,224, 2001. 24

[49] Brooks, T. F., D. S. Pope and M. A. Marcolini, *Airfoil Self-Noise and Prediction*. Reference Publication 1218, NASA, July 1989. 27, 28, 29, 30, 31, 103

[50] Migliore, P. and S. Oerlemans, *Wind Tunnel Aeroacoustic Tests of Six Airfoils for Use on Small Wind Turbines*. J. Sol. Energy Eng., 126(4):974–985, November 2004. 29, 103

[51] Nash, E. C., M. V. Lowson and A. McAlpine, *Boundary layer instability noise on aerofoils*. J. Fluid Mech., 382:27–61, 1999. 29

[52] Arnold, D., T. Nishida, L. N. Cattafesta and M. Sheplak, *A directional acoustic array using silicon micromachined piezoresistive microphones*. J. Acoust. Soc. Am., 113:289–298, January 2003. 36

[53] Humphreys Jr, W. M., Q. A. Shams, S. S. Graves, B. S. Sealey, S. M. Bartram and T. Comeaux, *Application of MEMS Microphone Array Technology to Airframe Noise Measurements*. In *11th AIAA/CEAS Aeroacoustics Conference*, AIAA-2005-3004, May 2005. 36, 64

[54] Orlando, S., A. Bale and D. Johnson, *Design and Preliminary Testing of a MEMS Microphone Phased Array*. In *Berlin Beamforming Conference*, BeBec-2010-21, Berlin, DE, February 2010. 36

[55] Knowles Acoustics, *Surface Mount MEMS Microphones*, July 2009, `http://www.knowles.com/search/product.htm?x_sub_cat_id=3`. 36

[56] Knowles Acoustics, *SPM0408LE5H*, April 2009, `http://www.knowles.com/search/prods_pdf/SPM0408LE5H.pdf`. 37, 44, 48, 61

[57] Knowles Acoustics, *Sisonic Design Guide*, May 2008, revision 2.1. 38, 39, 40

[58] Knowles Acoustics, *SPM0408HE5H*, September 2009, `http://www.knowles.com/search/prods_pdf/SPM0408HE5H.pdf`. 40, 48, 61

[59] FreePCB, July 2009, `http://www.freepcb.com/`. 44

[60] Alberta Printed Circuits, November 2009, http://www.apcircuits.com. 45

[61] Zhai, C. J., Sidharth and R. Blish II, *Board Level Solder Reliability Versus Ramp Rate and Dwell Time During Temperature Cycling*. IEEE Transactions on Device and Materials Reliability, 3(4):207–212, December 2003. 48

[62] Nordic Semiconductor, *QFN Soldering Reflow Guidelines*, December 2006, Application Note nAN400-08. 48

[63] Chip Quik Inc., *Chip Quik SMD4300AX10 Solder Paste Product Sheet*. http://www.chipquikinc.com/store/paste/prod_smd4300ax10.htm. 48

[64] Zuckerwar, A. J., G. C. Herring and B. Elbing, *Calibration of the pressure sensitivity of microphones by a free-field method at frequencies up to 80 kHz*. J. Acoust. Soc. Am., 119(1):320–329, January 2006. 53, 54, 56

[65] Crocker, M. J., ed., *Handbook of Acoustics*. John Wiley & Sons, Inc., New York, NY, 1998. 53, 54

[66] Wong, G. S. K., *Springer Handbook of Acoustics*, chap. Microphones and Their Calibration. Springer, New York, NY, 2007. 54, 55, 56

[67] *AES Information Document - Plane-Wave Tubes: Design and Practice*. Journal of the Audio Engineering Society, 39:476–80, June 1991. 54, 55

[68] Arnold, D. P., S. Gururaj, S. Bhardwaj, T. Nishida and M. Sheplak, *A Piezoresistive Microphone for Aeroacoustic Measurements*. In *2001 ASME International Mechanical Engineering Congress and Exposition*, New York, NY, November 2001. 54, 64

[69] Magalotti, R., C. Zuccatti and P. Pasini, *Building a plane-wave tube: experimental and theoretical aspects*. Journal of the Audio Engineering Society, 47:596–601, July/August 1999. 55

[70] Brüel & Kjær, *Pistonphone type 4228*. www.bksv.com/doc/bp0881.pdf. 56

[71] McPhee, A. D., *The Development of a Research Technique for Low Speed Aeroacoustics*. Master's thesis, University of Waterloo, Waterloo, ON, 2008. 56, 57, 58

[72] Marcolini, M., P. Lorber, W. T. Miller Jr and A. F. Covino Jr, *Frequency response calibration of recess-mounted pressure transducers*. Tech. Rep. 104031, NASA, March 1991. 56

[73] Hazlett, T., *Personal correspondence*. Knowles Acoustics, 2009, http://www.knowles.com. 62

[74] National Instruments Corporation, *NI 9237 Specifications*. http://sine.ni.com/nips/cds/view/p/lang/en/nid/208791. 65, 122

[75] National Instruments Corporation, *NI 9178 Specifications*. http://www.ni.com/pdf/manuals/372838a.pdf. 65, 122

[76] National Instruments Corporation, *NI LabVIEW*. http://www.ni.com/labview/. 65

[77] Blackstock, D., *Fundamentals of Physical Acoustics*. John Wiley & Sons, Inc., New York, NY, 2000.

[78] Horowitz, S., T. Nishida, L. Cattafesta and M. Sheplak, *Development of a micromachined piezoelectric microphone for aeroacoustics applications*. Journal of the Acoustical Society of America, 122, no 6:3428–3436, Dec 2007.

[79] Oerlemans, S. and B. Méndez López, *Acoustic Array Measurements on a Full Scale Wind Turbine*. In *11th AIAA/CEAS Aeroacoustics Conference*, AIAA-2005-2963, Monterey, CA, May 2005.

Appendices

Appendix A

Reflow Temperature Controller: LabVIEW Software

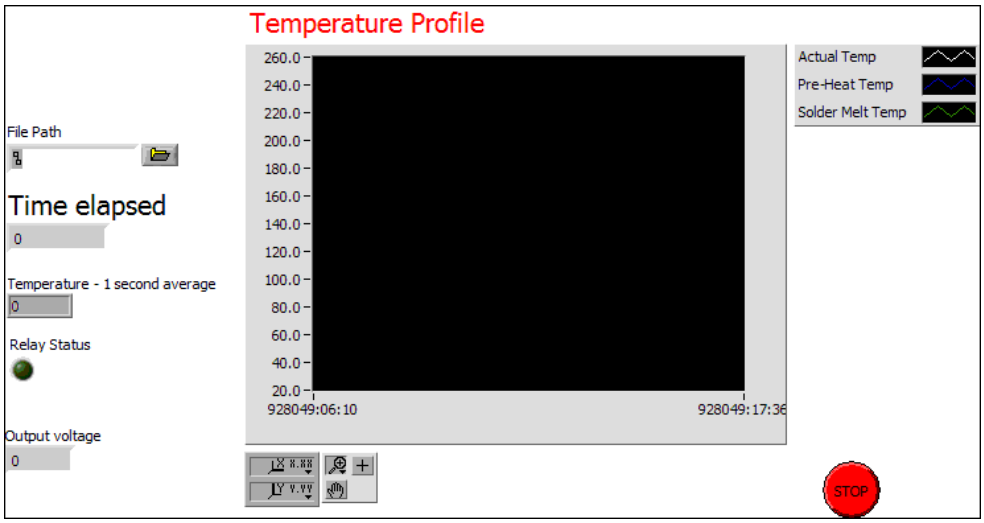
Temperature Profile
260.0
240.0
220.0
200.0
180.0
160.0
140.0
120.0
100.0
80.0
60.0
40.0
20.0
928049:06:10
928049:17:36
Actual Temp
Pre-Heat Temp
Solder Melt Temp
File Path
Time elapsed
0
Temperature - 1 second average
0
Relay Status
Output voltage
0
STOP

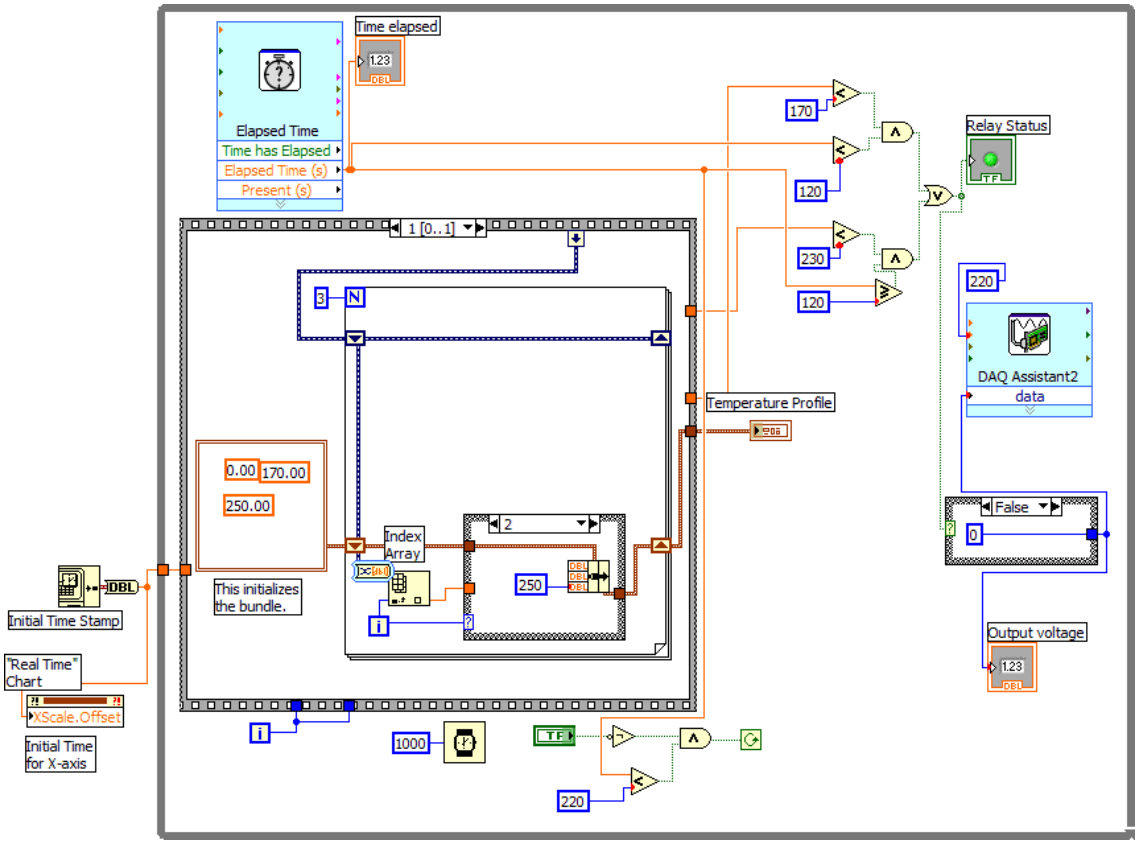
Time elapsed
Elapsed Time
Time has Elapsed
Elapsed Time (s)
Present (s)
1 [0..1]
3
N
0.00
170.00
250.00
This initializes the bundle.
Index Array
2
250
i
1000
170
120
230
120
220
Relay Status
DAQ Assistant2
data
Temperature Profile
False
0
Output voltage
Initial Time Stamp
"Real Time" Chart
XScale.Offset
Initial Time for X-axis

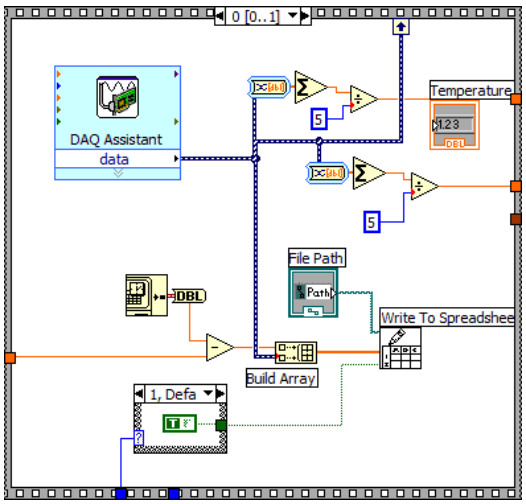
0 [0..1]
DAQ Assistant
data
5
Temperature
1.23
DBL
5
File Path
Path
DBL
Write To Spreadshee
Build Array
1, Defa
T F

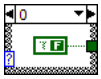
0
T F

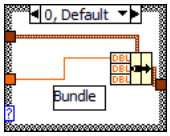
0, Default
DBL
DBL
DBL
Bundle

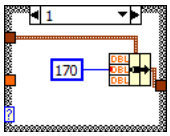
1
170
DBL
DBL
DBL

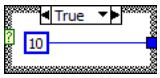
True
10

Appendix B

Microphone Array Details

Presented below are the microphone coordinates referenced to the array centre for both microphone arrays. A list of microphone sensitivities for both arrays and a connection guide for the data acquisition system are also included.

B.1 Microphone Array Coordinates

Table B.1: Small-scale array coordinates

Sensor Number	x-coordinate (mm)	y-coordinate (mm)
1	-12.95	0
2	-9.91	-8.38
3	-2.29	-12.70
4	6.60	-11.18
5	12.19	-4.57
6	12.19	4.57
7	6.60	11.18
8	-2.29	12.70
9	-9.91	8.38
10	32.26	-13.97
11	33.78	10.16
12	19.30	29.46
13	-4.06	35.05
14	-25.65	24.13
15	-35.05	-2.03
16	-28.19	-21.08
17	-8.13	-34.29
18	15.75	-31.50
19	5.08	70.10
21	-68.33	17.02
22	-63.25	-30.73
23	-28.70	-64.26
24	19.30	-67.82
25	58.42	-39.37
26	70.10	7.37
27	49.02	50.55

Table B.2: Large-scale array coordinates

Sensor Number	x-coordinate (mm)	y-coordinate (mm)
1	-35	0
2	-10.82	-33.29
3	28.32	-20.57
4	28.32	20.57
5	-10.82	33.29
6	106.45	-31.30
7	62.66	91.56
8	-67.72	87.89
9	-104.51	-37.25
10	3.13	-110.91
11	-85.46	253.86
12	-267.85	-2.83
13	-80.08	-255.61
14	218.35	-155.15
15	215.03	159.72
16	-289.96	194.38
17	-274.47	-215.70
18	120.32	-327.69
19	348.84	13.17
20	95.27	335.83
21	-408.25	69.23
22	-191.99	-366.88
23	289.59	-295.97
24	370.97	183.96
25	-60.32	409.66
26	-465.03	-68.18
27	-78.86	-463.34
28	416.29	-218.18
29	336.14	328.49
30	-208.54	421.20

B.2 Microphone Sensitivities

Table B.3: Small-scale and large-scale array microphone sensitivities at 1 kHz

Microphone Number	SSA (mV/Pa at 1 kHz)	LSA (mV/Pa at 1 kHz)
1	112.8	40.7
2	119.4	37.5
3	117.6	38.0
4	117.4	38.6
5	120.2	37.7
6	119.2	36.9
7	118.3	36.8
8	122.9	37.5
9	118.2	37.4
10	121.8	37.9
11	119.2	38.7
12	120.5	38.8
13	120.8	37.0
14	123.1	38.3
15	117.8	38.5
16	118.8	38.8
17	120.4	38.8
18	109.3	41.7
19	119.4	41.7
20	117.1	41.5
21	120.2	42.5
22	118.9	39.6
23	118.4	41.0
24	122.0	39.5
25	120.4	39.1
26	115.8	38.8
27	106.0	41.0
28	N/A	38.8
29	N/A	38.6
30	N/A	39.6

B.3 Data Acquisition System Connection Lists

Table B.4: NI 9178 cDAQ [75] and NI 9237 [74] module connection list (NC = No connection)

Module	Channel	SSA Microphone number	LSA Microphone number
1	0	26	27
	1	25	26
	2	27	30
	3	11	NC
2	0	10	17
	1	12	16
	2	7	22
	3	24	21
3	0	18	13
	1	5	12
	2	4	11
	3	6	25
4	0	8	10
	1	3	9
	2	17	1
	3	2	8
5	0	1	2
	1	9	3
	2	13	4
	3	19	5
6	0	14	6
	1	16	7
	2	23	14
	3	15	15
7	0	20	18
	1	22	19
	2	21	20
	3	NC	24
8	0	NC	23
	1	NC	28
	2	NC	29
	3	NC	NC

Appendix C

Microphone Signal Acquisition: LabVIEW Software

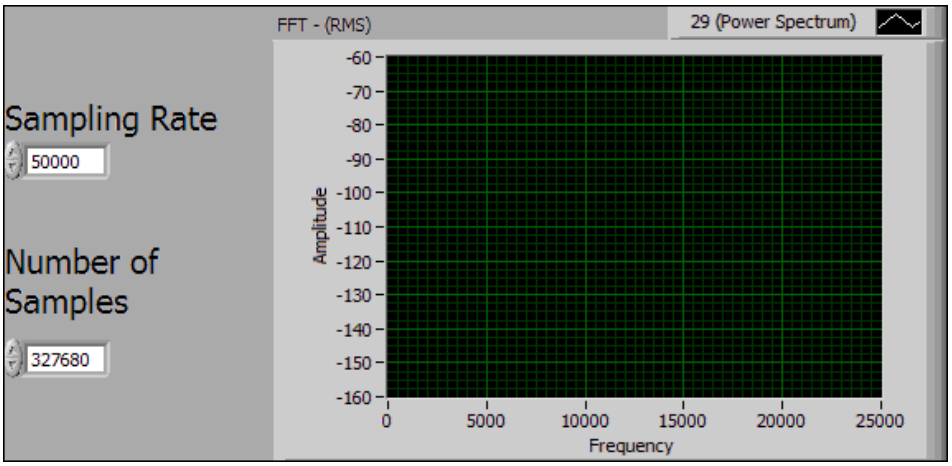
FFT - (RMS)
29 (Power Spectrum)
Sampling Rate
50000
Number of Samples
327680
Amplitude
-60
-70
-80
-90
-100
-110
-120
-130
-140
-150
-160
0
5000
10000
15000
20000
25000
Frequency

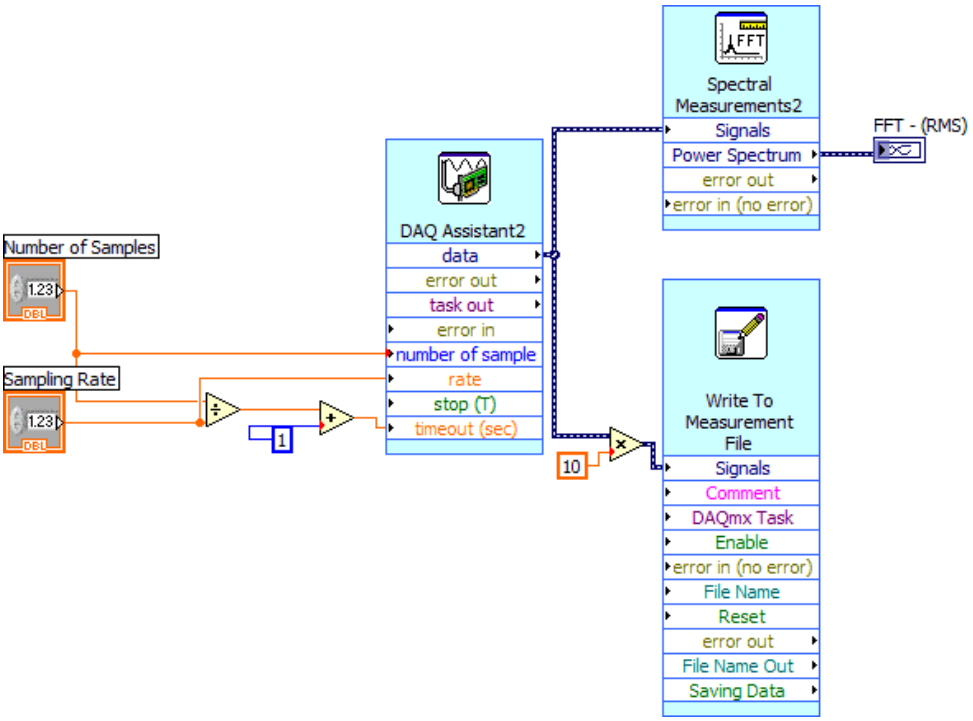
Spectral Measurements2
Signals
Power Spectrum
error out
error in (no error)
FFT - (RMS)
DAQ Assistant2
data
error out
task out
error in
number of sample
rate
stop (T)
timeout (sec)
Number of Samples
Sampling Rate
1.23
DBL
1
10
Write To Measurement File
Signals
Comment
DAQmx Task
Enable
error in (no error)
File Name
Reset
error out
File Name Out
Saving Data

Appendix D

Additional Source Maps

Source maps from test cases 2, 4, 7, 9, 16, 17, 19–22, 24–27, and 29–30, which were not presented in Chapter 6 are included below. Details regarding processing can be found within each section.

D.1 Small-Scale Array with Stationary Monopole Source

All plots in this section are normalized by their maximum sound pressure levels, with the centre of the source map on the array's z-axis. A dynamic range of 9 dB is shown. Source maps for Cases 2 and 4 enclose one square metre scan area with a grid spacing of 5 mm. Source maps in Cases 7 and 9 represent 4 square metres with a grid spacing of 10 mm. Block lengths of 8192 samples were used, with a total of 50 blocks being averaged.

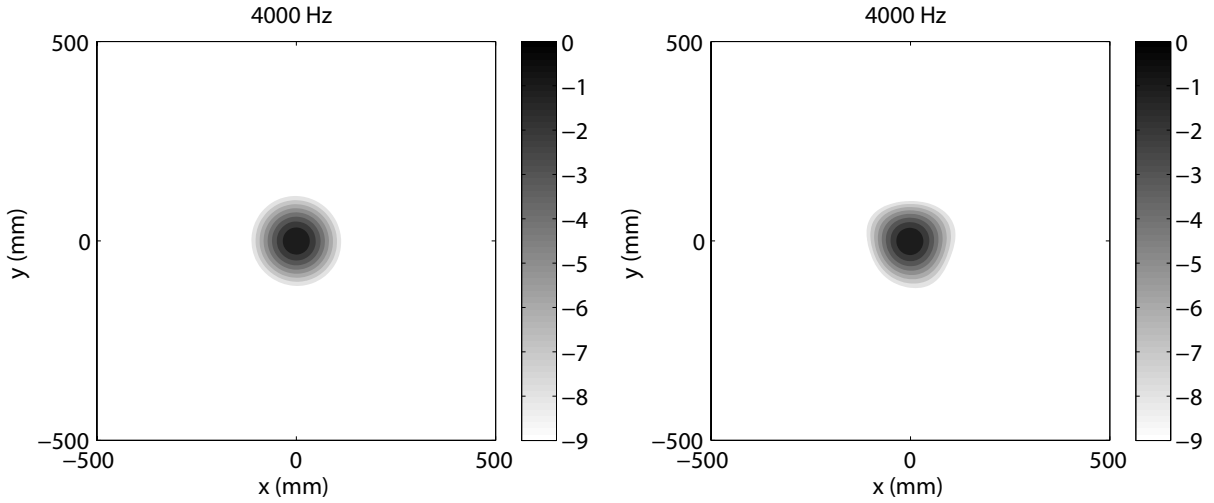

Figure D.1: Theoretical and measured SSA response for Case 2: 4 kHz monopole source along z-axis at 164 mm, 72.6 dB peak

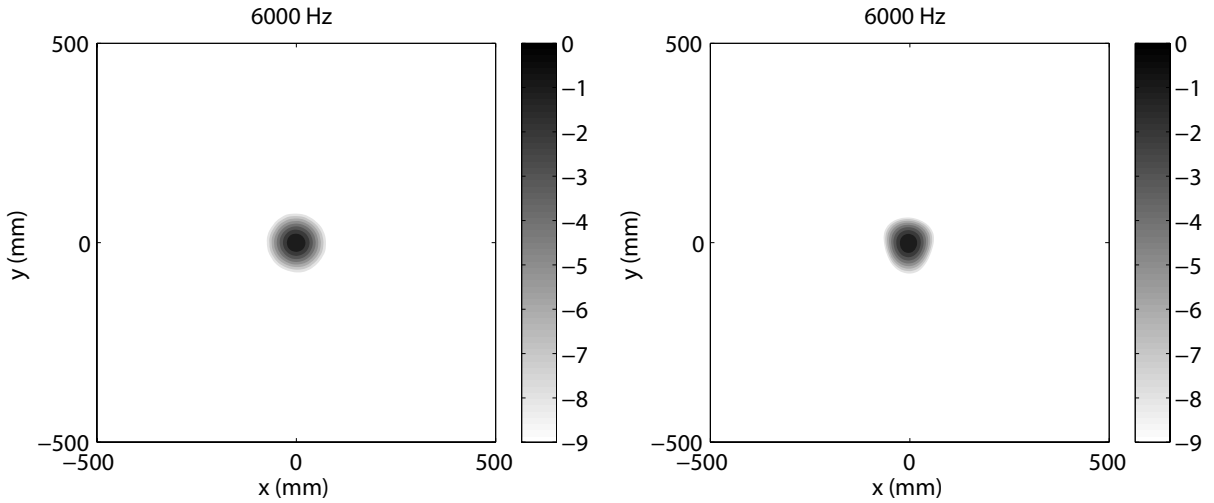

Figure D.2: Theoretical and measured SSA response for Case 4: 6 kHz monopole source along z-axis at 164 mm, 78.8 dB peak

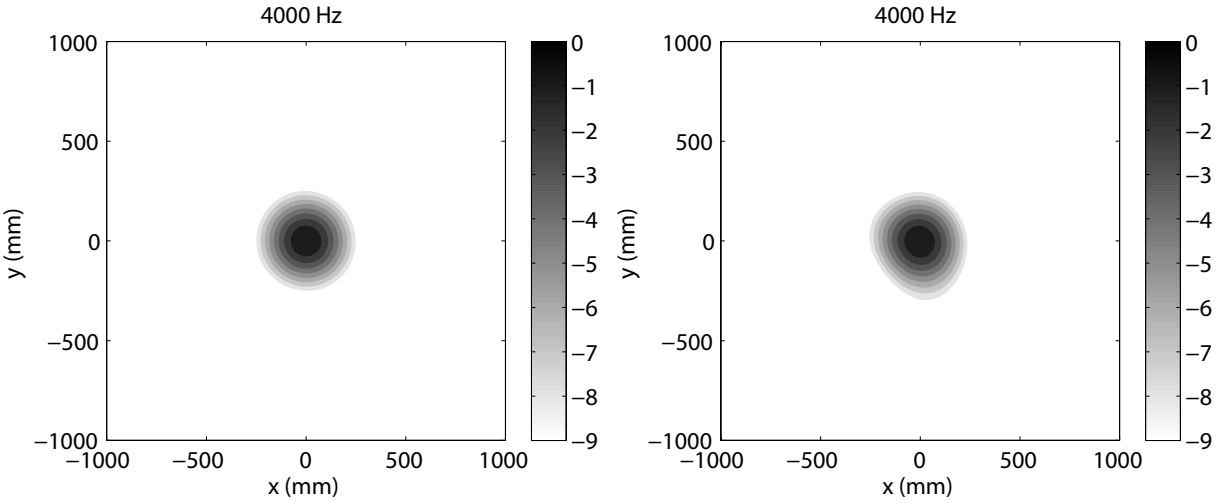

Figure D.3: Theoretical and measured SSA response for Case 7: 4 kHz monopole source along z-axis at 385 mm, 72.7 dB peak

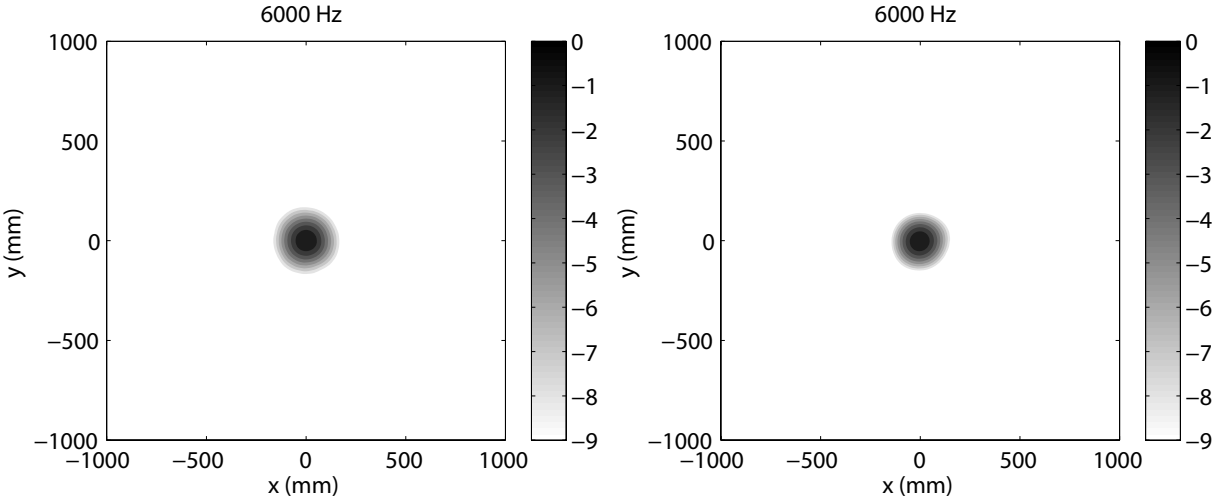

Figure D.4: Theoretical and measured SSA response for Case 9: 6 kHz monopole source along z-axis at 385 mm, 77.7 dB peak

D.2 Large-Scale Array with Stationary Monopole Source

Additional source maps containing the large-scale array's theoretical and measured responses to a monopole source along its z-axis are presented below. Source maps normal-

ized by the maximum sound pressure level are presented for Cases 16, 17, 19–22, 24–27, and 29–30. A dynamic range of 9 dB is shown. All source maps present 4 square metres with a grid spacing of 10 mm, with the centre of the scan plane along the array's z-axis. Block lengths of 8192 samples were used, with a total of 20 blocks averaged for the FFT calculations.

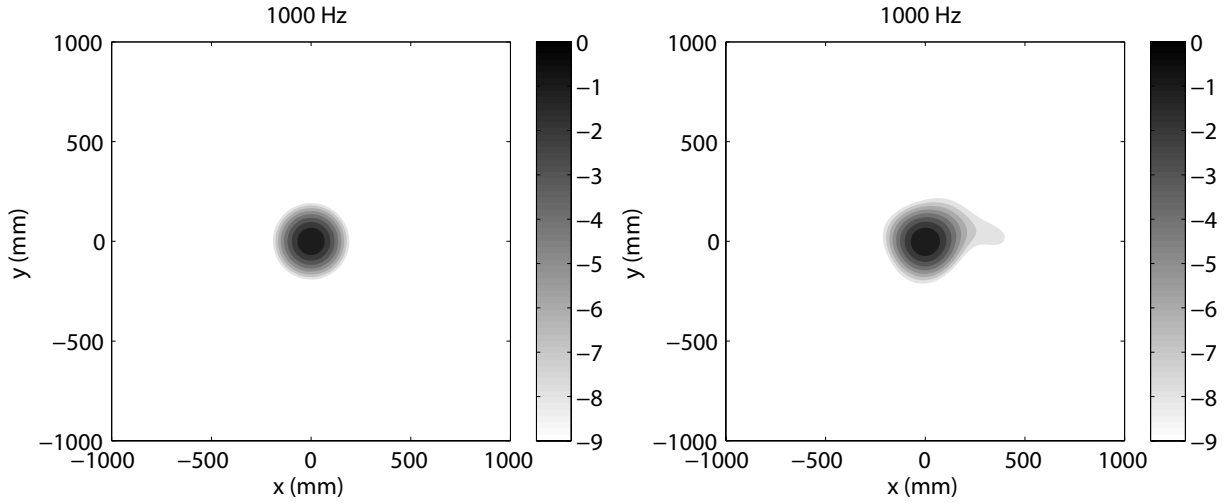

Figure D.5: Theoretical and measured LSA response for Case 16: 1 kHz monopole source along z-axis at 500 mm, 88.0 dB peak

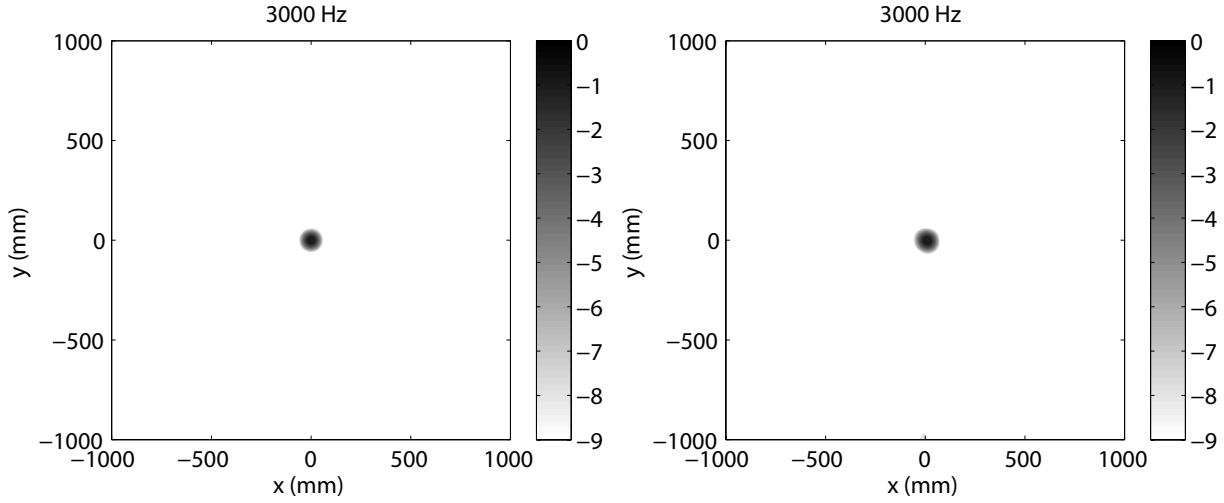

Figure D.6: Theoretical and measured LSA response for Case 17: 3 kHz monopole source along z-axis at 500 mm, 84.6 dB peak

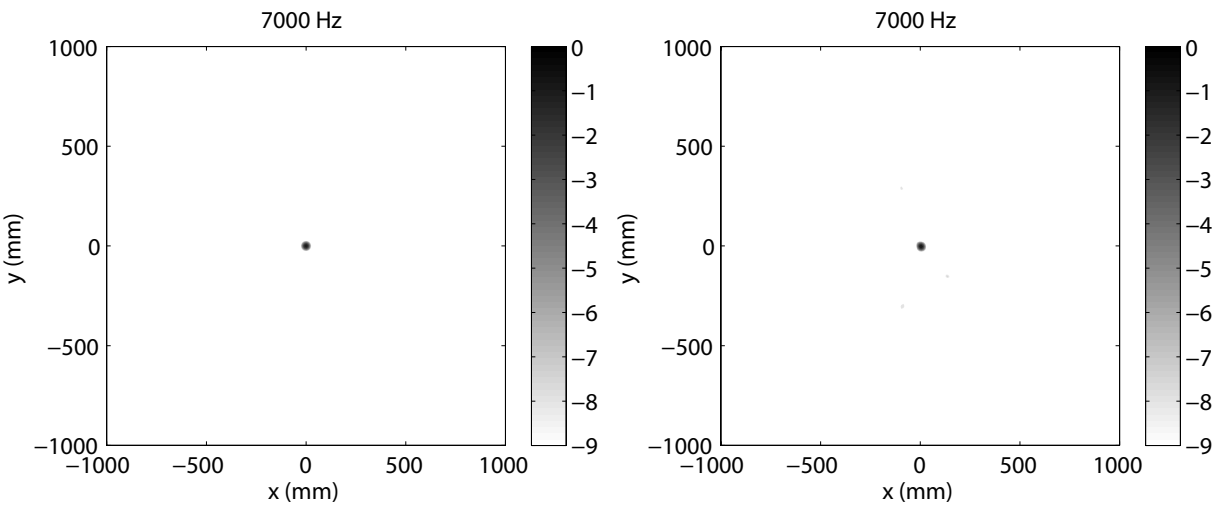

Figure D.7: Theoretical and measured LSA response for Case 19: 7 kHz monopole source along z-axis at 500 mm, 82.9 dB peak

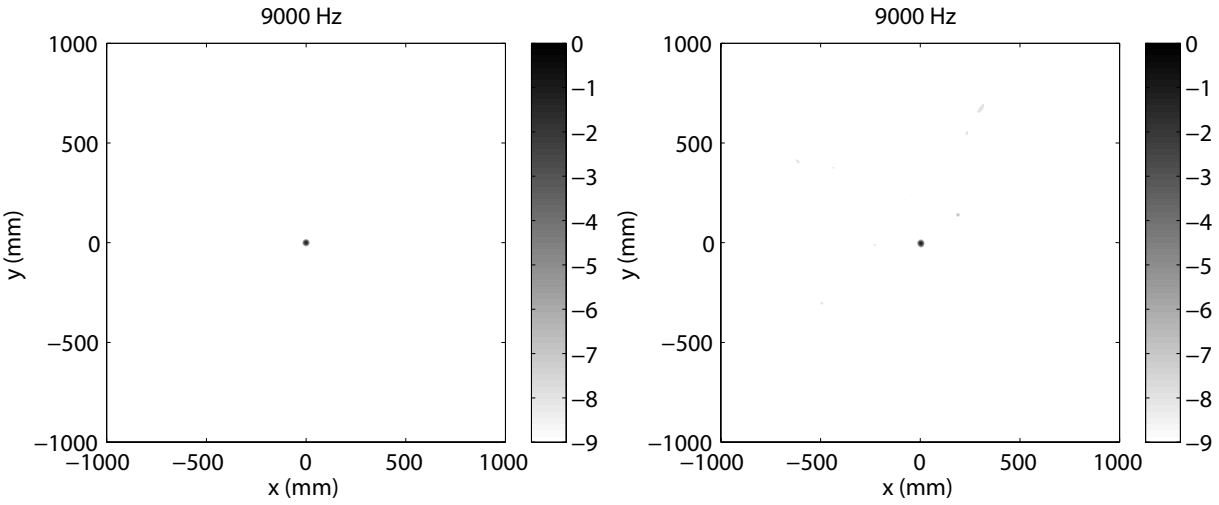

Figure D.8: Theoretical and measured LSA response for Case 20: 9 kHz monopole source along z-axis at 500 mm, 90.4 dB peak

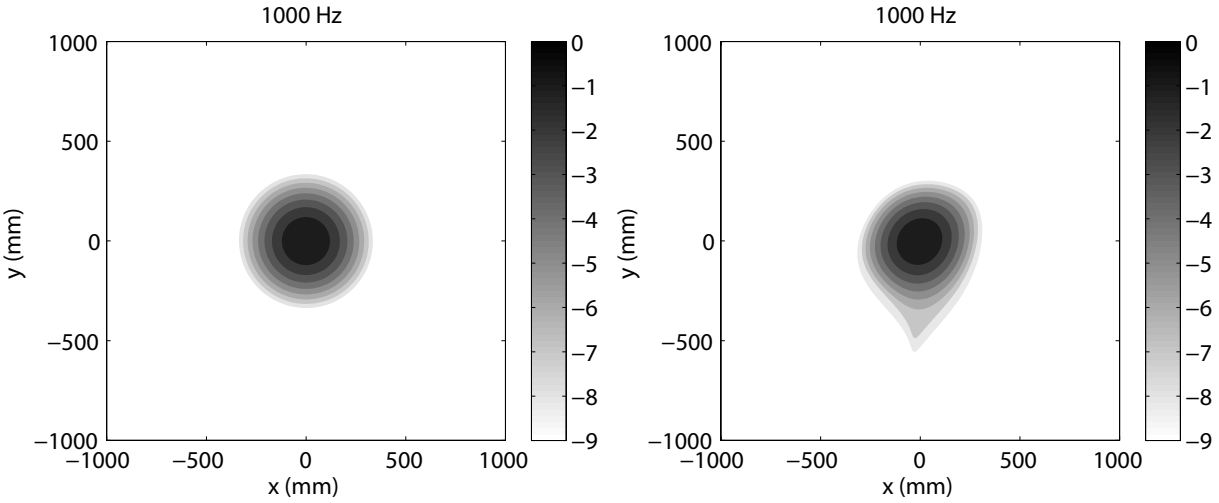

Figure D.9: Theoretical and measured LSA response for Case 21: 1 kHz monopole source along z-axis at 1000 mm, 85.1 dB peak

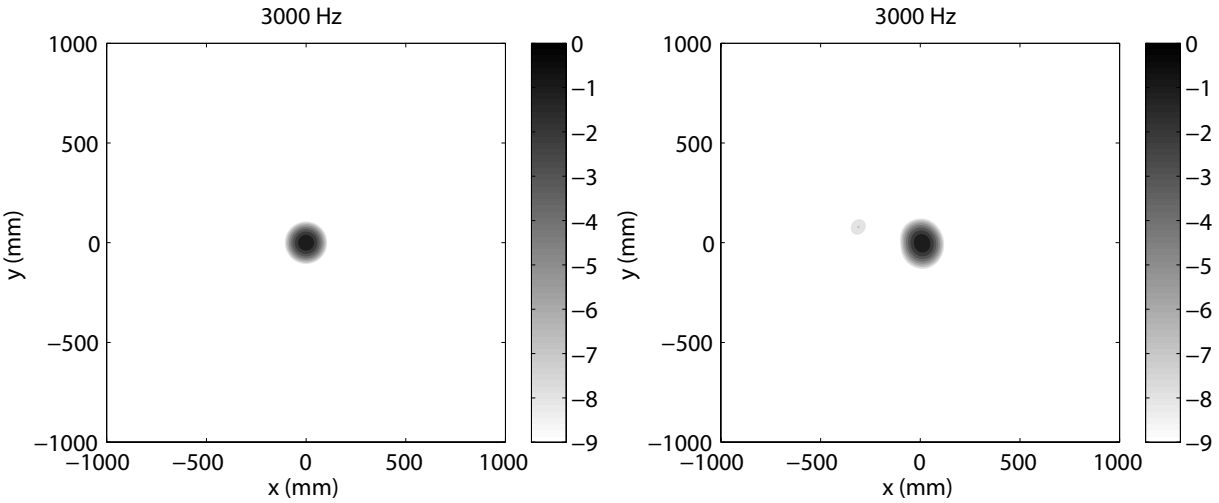

Figure D.10: Theoretical and measured LSA response for Case 22: 3 kHz monopole source along z-axis at 1000 mm, 83.8 dB peak

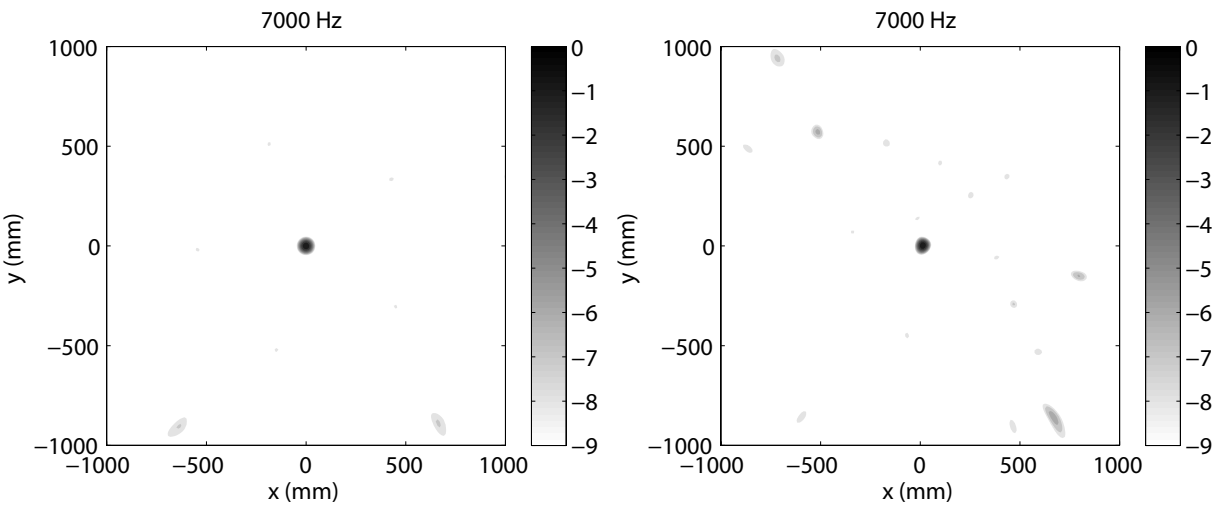

Figure D.11: Theoretical and measured LSA response for Case 24: 7 kHz monopole source along z-axis at 1000 mm, 84.8 dB peak

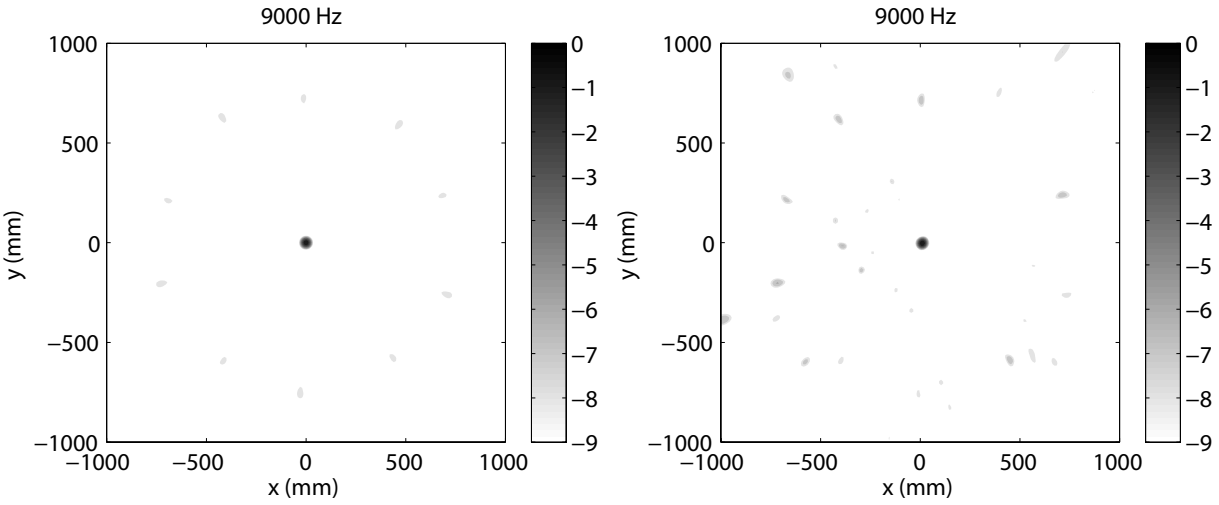

Figure D.12: Theoretical and measured LSA response for Case 25: 9 kHz monopole source along z-axis at 1000 mm, 85.5 dB peak

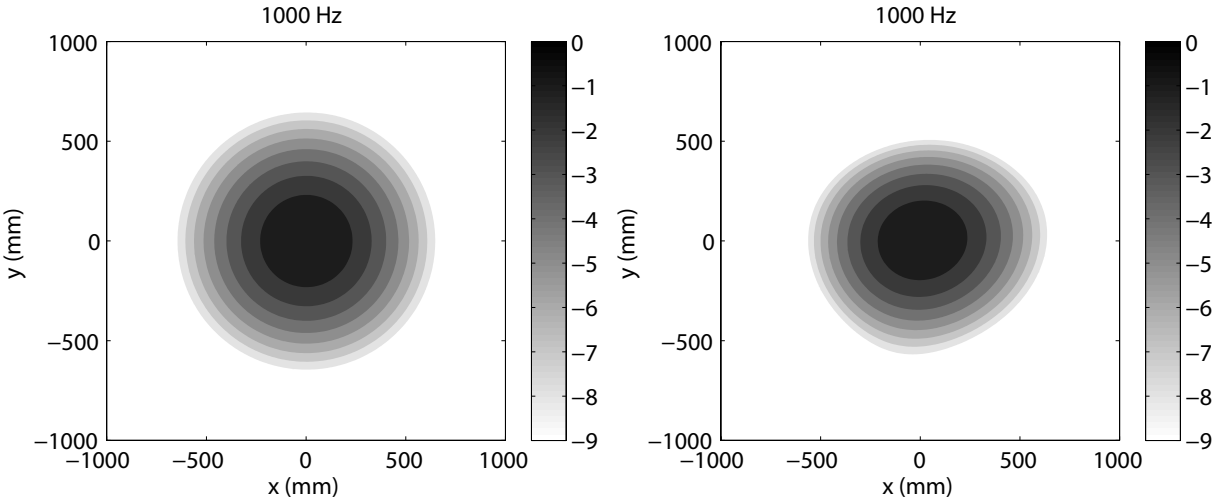

Figure D.13: Theoretical and measured LSA response for Case 26: 1 kHz monopole source along z-axis at 2000 mm, 78.5 dB peak

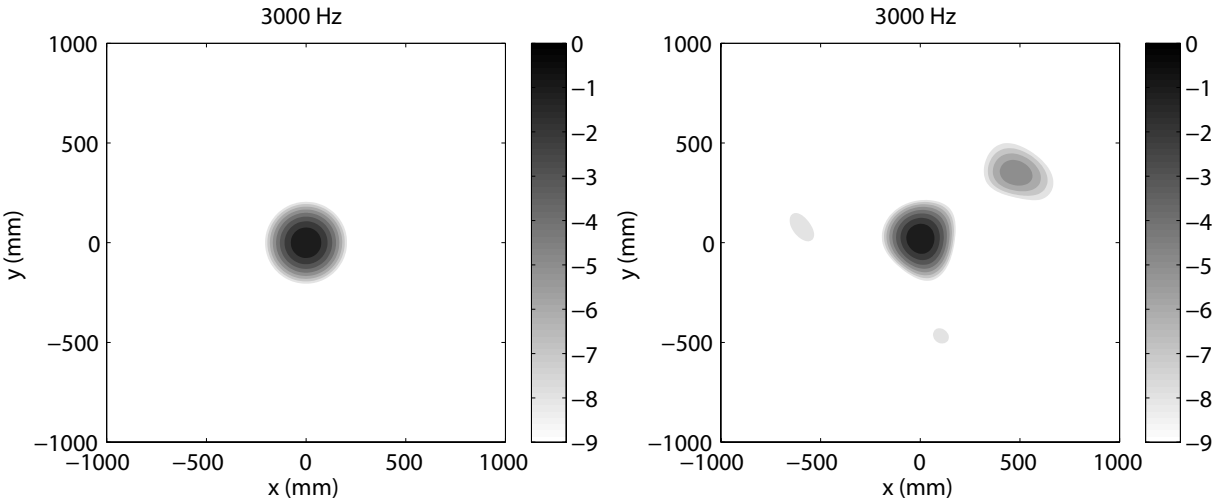

Figure D.14: Theoretical and measured LSA response for Case 27: 3 kHz monopole source along z-axis at 2000 mm, 77.0 dB peak

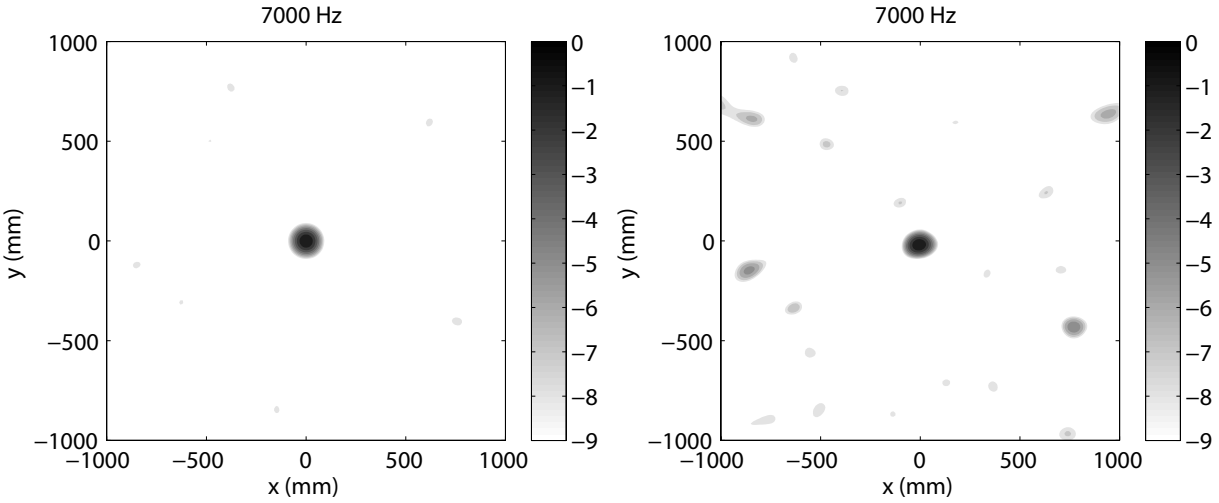

Figure D.15: Theoretical and measured LSA response for Case 29: 7 kHz monopole source along z-axis at 2000 mm, 77.5 dB peak

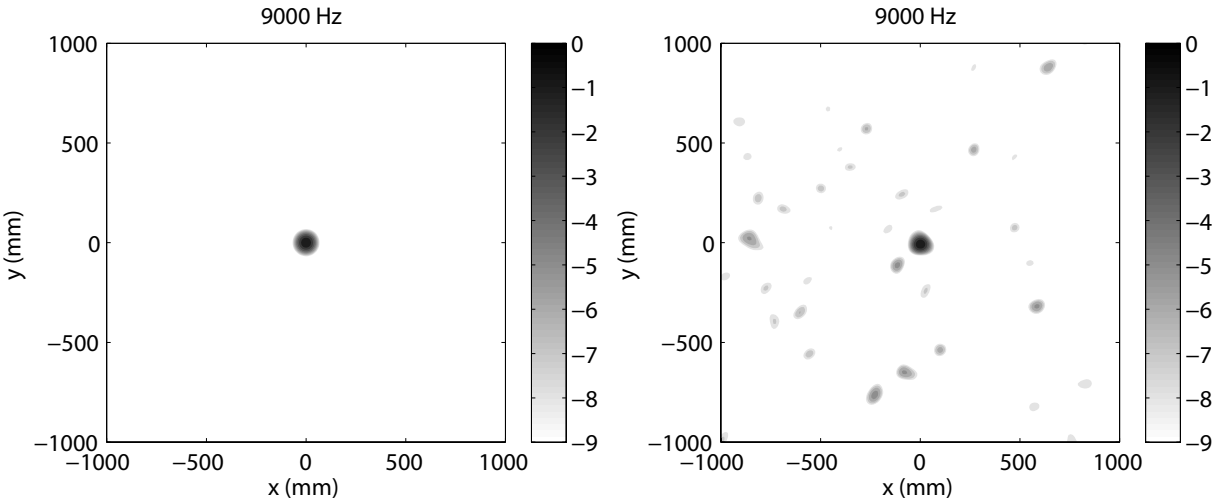

Figure D.16: Theoretical and measured LSA response for Case 30: 9 kHz monopole source along z-axis at 2000 mm, 78.0 dB peak